

# NOVEL UV METHODS FOR PATTERNING MICRO-SCALE CONDUCTIVE STRUCTURES ON INSULATING DIAMOND SURFACES

By

**Matthew Allen Clarke**

Submitted in partial completion of the requirements for the degree of

**Master of Research**

in the Faculty of Science at Macquarie University

October 2014





## Preface

I would like it known to all relevant parties that I have submitted a formal request for acknowledgement of Disruption to Studies to the Physics MRes Advisor, due to my hospitalisation from 4th to 11th of June and debilitating illness leading to my hospitalisation through the prior fortnight. After being discharged, it was another week before I returned to campus as I needed time to adjust to my new medications. As a result of my illness, I have lost nearly a month from the middle of my research project and am concerned that the completion of my project to my full capacity has suffered as a result. The relevant documentation of my illness and inability to complete my studies during the period of my illness has been supplied to the university.

Matthew Clarke

## Abstract

This thesis reports an investigation into laser direct-write manipulation of the terminating layer on diamond surfaces. A novel two-photon etching process is used to partially or completely oxidize the diamond surface to create functional surfaces with engineered regions of oxygen and hydrogen termination.

Hydrogen-terminated diamond has a sub-surface two-dimensional hole sheet, with a carrier density of  $\sim 2 \times 10^{13} \text{ cm}^{-2}$  which results in conduction when the surface is exposed to a mildly acidic water layer. This is contrasted by an oxygen-terminated surface that is highly insulating. Two-photon UV etching of oxygen-terminated regions on a hydrogen-terminated surface thus has the potential, for example, to enable a highly practical method for developing micro-scale surface electronic systems. To this end, hydrogen-terminated surfaces were prepared by exposure to a high-power hydrogen plasma source and electrically characterised after evaporation of Au contacts onto the surface. A method of producing consistent, low-resistivity, and smooth hydrogen-terminated surfaces has been developed empirically.

Conducting tracks of H-termination were electrically isolated by direct-write two-photon UV laser etching. This technique has been used to electrically isolate individual, and pairs of, Au contacts from the bulk surface whilst allowing conduction inside the region defined by the etched path. Also, partial removal of H-termination was demonstrated enabling the resistance (hole doping) on the surface to be modified in a highly controllable fashion over many orders of magnitude. This result demonstrates an important feature of the laser technique compared with traditional chemical doping techniques.

Patterning of hydrogen and oxygen terminated regions was used to structure planar field-effect transistors (FETs). Although the FETs displayed significant resistance and were sub-optimal devices nevertheless the drain-source current was influenced by the gate voltage. These results provide the basis towards a functioning p-type surface conduction diamond FET fabricated by a direct-write laser technique, and is the first demonstration of the ability to write complex patterns into the surface termination of diamond by way of pulsed UV laser techniques.

This work reveals the challenges ahead to developing practical devices, and highlights the potential for the UV laser direct-write technique for rapid-prototyping of functionalized diamond surface structures for electronics as well as other possible interesting applications including quantum devices and biosubstrates.

## Acknowledgements

In no particular order I would like to thank and acknowledge: Chris Baldwin for his instruction and assistance in the use of the laser etching system; Adam Joyce for the use of the optical profiler; the Macquarie ANFF OptoFab Node, specifically Peter Ha for running the hydrogen-plasma chamber and the field-emission SEM, as well as Alex Stokes and Ben Johnson for laser cutting the evaporation masks and the initial SEM work.

Thanks also go to my supervisors, Rich Mildren and James Downes, for always being optimistic about my progress.

Finally I would like to thank the staff at Westmead Hospital, and in particular to staff from the Medical High Dependency ward, for bringing me back to full health and able to see this project through.

## Table of Contents

Preface.....	i
Abstract .....	ii
Acknowledgements .....	iii
1 Introduction.....	1
1.1 Project Overview .....	1
1.2 Diamond Electronics.....	2
1.3 Diamond Surface Conduction Channel.....	4
1.4 Review of Diamond Surface Devices .....	7
1.5 UV Laser Etching of Diamond .....	15
1.6 Project Direction.....	19
2 Sample Processing Techniques.....	21
2.1 The UV Laser Etching System.....	21
2.2 Hydrogenation of diamond films.....	22
2.3 Au Contact Evaporation.....	25
3 Electrical Characterisation of the Diamond Surface.....	29
4 Results & Discussion .....	33
4.1 Etch Calibrations on H-terminated Diamond .....	33
4.2 Early Electrical Isolation Attempts.....	37
4.3 Partial etching and dopant modification.....	39
4.4 Isolated conducting paths .....	45
4.5 Fabricating Field-Effect Transistors .....	47
5 Conclusions.....	54
6 References .....	56
7 Appendix.....	60
7.1 Optical Interferometry.....	60
7.1.1 Phase-shifting Interferometry (PSI) .....	60
7.1.2 Vertical-scanning Interferometry (VSI).....	61
7.2 G-code scripts .....	62

## List of Figures

Figure 1-1 Surface conductance of the hydrogenated (masked) and the hydrogen-free (irradiated) part of a homoepitaxial diamond (100) layer in UHV and during exposure to air. Image credit: [27] ....	4
Figure 1-2 Schematic picture of the hydrogenated diamond surface in contact with a water layer as it forms in air. Image credit: [27] .....	5
Figure 1-3 Schematic drawing of the diamond/adsorbate heterojunction for the (a) non-equilibrated and (b) equilibrated case. Electrons from the valence-band diffuse into empty electronic states of the adsorbate layer as long as the chemical potential $\mu$ is lower than the Fermi energy $E_F$ . Image credit: [29] .....	6
Figure 1-4 Metal-Oxide-Semiconductor Field-Effect Transistor (MOSFET). Image credit: [38] .....	7
Figure 1-5 LEFT: Enhancement-type FET. RIGHT: Depletion-type FET. Each I-V curve is for a separate gate voltage. Image credit: [38] .....	8
Figure 1-6 Requirements for RF high-power devices and the capability of semiconductors to meet them. Image credit: [5] .....	9
Figure 1-7 DC output characteristics of a 50 nm gate length H-termination diamond FET. The dashed line indicates initial measurement of $I_d$ prior to application of the present gate voltage range. Image credit: [39] .....	10
Figure 1-8 SEM micrograph of circular FET structure. The bright areas are the active areas with hydrogen terminated surface. The dark areas are the insulating oxygen passivated surrounding areas. Image credit: [21] .....	10
Figure 1-9 DC characteristics of; LEFT: rectangular FET structure $L_g = 3.0 \mu\text{m}$ , $W_g = 100 \mu\text{m}$ , $L_{ds} = 12 \mu\text{m}$ . The insert shows the transconductance versus gate bias. RIGHT: circular FET structure. $L_g = 8.5 \mu\text{m}$ , $W_g = 500 \mu\text{m}$ , $L_{ds} = 50 \mu\text{m}$ . The breakdown voltage shown was destructive. Image credit: [21] .....	11
Figure 1-10 Schematic diagram of H-terminated diamond FET. Image credit: [5] .....	11
Figure 1-11 AFM image of diamond single-hole transistor. Bright and dark regions represent locally oxidized (O-terminated) and H-terminated regions, respectively. Image credit: [23] .....	12
Figure 1-12 Schematic and AFM image of; LEFT: single-hole transistor, RIGHT: a dual side-gated FET. Both structures are formed by local anodisation of the H-terminated surface by applying a positive voltage between the AFM cantilever tip and the diamond substrate. Image credit: [42] .....	13
Figure 1-13 $I_{ds} - V_{gs}$ characteristics of a diamond single-hole transistor at 77 K. $V_{ds}$ is -50 mV. Coulomb oscillation is observed with distinct peaks at 1.4 V intervals ( $\Delta V_{gs}$ ). Image credit: [23] .....	13
Figure 1-14 $I_{ds} - V_{ds}$ characteristics of a side-gated FET. (a) Measured at room temperature. (b) Measured at 4.4 K. Image credit: [42] .....	14
Figure 1-15 $I_{ds} - V_{gs}$ characteristics measured at 4.6 K. $V_{ds} = -15\text{V}$ . Image credit: [42] .....	14
Figure 1-16 Image of a single-crystal diamond surface obtained after irradiation by 100,000 pulses from a KrF excimer laser (laser fluence $10 \text{ J/cm}^2$ , intensity $109 \text{ W/cm}^2$ ). Image credit: [4] .....	15

Figure 1-17 LEFT: Dependence of the etching depth on the number of radiation pulses for different laser fluencies in the laser spot. RIGHT: Dependence of the laser nanoablation rate on the laser fluence at room temperature. Image credit: [4] .....	16
Figure 1-18 Interferometric optical profile image of the surface pit after exposure to $3.6 \times 10^{10}$ pulses of energy 10 nJ. The cross-section through the deepest point is shown to the right. Image credit: [46] .....	17
Figure 1-19 Microscope images of the diamond surface subsequent to exposure at a) 1.1, b) 0.6 times the ablation threshold. The exposure times were 0.05 s and 30 s, and the crater depths 30 $\mu\text{m}$ and 0.60 $\mu\text{m}$ respectively; the pulse rate was 7.5 kHz. In a), the beam size is indicated by the dashed circle. For b) the contrast was enhanced using differential interferometric contrast mode. Image credit: [3] .....	17
Figure 1-20 Etch rate as a function of laser fluence. The data point shown for the fluence above the ablation threshold corresponds to the average ablation rate per pulse for 60 pulses of fluence 110 $\text{J} \cdot \text{cm}^{-2}$ . Pulse rate 7.5 kHz. Image credit: [3] .....	18
Figure 1-21 Dependence of the laser nanoablation rate on the temperature of the externally heated sample for a laser fluence of 5.4 $\text{J} \cdot \text{cm}^{-2}$ . The linear fit in the Arrhenius coordinates suggests ejection of carbon atoms obeys Boltzmann statistics. Image credit: [4] .....	19
Figure 2-1 UV laser etching system and detailed schematic of objective/translation stage. ....	21
Figure 2-2 a) Ball-and-stick drawing of octane and b) H-terminated diamond lattice. Image credit: [49] .....	22
Figure 2-3 Optical interferometry (PSI) image of the surface roughness on the front face of the 0.5 mm thick single-crystal diamond after the initial hydrogen-plasma treatment. This image shows a typical surface between the Au contacts. ....	23
Figure 2-4 Optical interferometry (PSI) image of the surface roughness on the back face of the 0.5 mm thick single-crystal diamond after the second hydrogen-plasma treatment. The back face does not appear to be as rough and does not show the same distinctive pitting as the front face. ....	24
Figure 2-5 H-terminated diamond FET fabrication process. (a) Epitaxial growth of diamond and hydrogen termination of the surface. (b) Evaporation of Au and formation of MESA structures using optical lithography. (c) Device isolation using oxygen plasma. (d) E-beam lithography for T-gate and wet chemical Au etch back. (e) Self-aligned Al evaporation. (f) Gate patterning and lift-off. Image credit: [58] .....	26
Figure 2-6 LEFT: Schematic of sample mount cut by Macquarie Engineering and Technical Services. The middle groove where the mask sits is 0.8 mm deep and the inner region is cut right through. RIGHT: Schematic of nickel evaporation mask, laser-cut by Macquarie University ANFF OptoFab Node. All measurements are in mm. ....	27
Figure 2-7 Optical surface profile image of a Au contact deposited onto polycrystalline diamond. The stepped effect along the edge is likely due to movement between the diamond and mask during the Au evaporation process. The vertical scale is exaggerated for clarity. ....	27



Figure 2-8 Optical surface profile image of Au deposited onto 0.5 mm thick single-crystal diamond. The Au is approximately 260 $\mu\text{m}$ wide and 0.1 $\mu\text{m}$ thick. The vertical scale is exaggerated for clarity. ....	28
Figure 3-1 Optical micrograph of surface connection of Au-coated probes onto Au contacts deposited on a polycrystalline diamond film. Each Au contact, which appears as a black square due to the optics of the microscope, is 0.26 mm in side length. The diamond is sitting in a groove on a custom designed aluminium block, which prevents the diamond from sliding when the Au-coated tungsten probes apply pressure. The probes would remain in place and the diamond was translated beneath the probes to measure the resistance across each pair of horizontally adjacent Au contacts. ....	29
Figure 3-2 Surface resistance of a single-crystal 0.2 mm thick hydrogen-terminated diamond film plotted in a 2-dimensional contour plot. The axes in the figure refer to the pairs of Au contacts and not to coordinates on the diamond. The lower right corner of the plot contains no data points due to the Au cross-hair in that corner. Resistance is measured in $\text{k}\Omega$ , although the data is truncated at the edges due to the high resistance ( $\geq 1\text{M}\Omega$ ) between the contacts along the edge of the diamond. ....	30
Figure 3-3 Optical surface profile image of a Au contact on 0.2 mm thick single-crystal diamond which had been damaged during electrical characterisation of the surface. The Au-plated tungsten probes used for electrical measurements are capable of scratching through the Au right to the diamond surface below. ....	31
Figure 3-4 Surface resistance of the single-crystal 0.5 mm thick hydrogen-terminated diamond film after the first hydrogenation treatment plotted in a 2-dimensional contour plot. Resistance is measured in $\text{k}\Omega$ , the relative humidity was 53%. The axes in the figure refer to the pairs of Au contacts and not to coordinates on the diamond. The lower right corner of the plot contains no data points due to the Au cross-hair in that corner. ....	32
Figure 4-1 Evidence of ablation during laser focus and etch depth calibrations on 0.2 mm thick single crystal diamond at an incident power of $(320 \pm 20)$ mW. The intended etch was to be a series of vertical lines with systematic variation in the etch depth due to translation of the stage through the focal plane. The approximate position of the intended etches are marked with dotted lines. ....	34
Figure 4-2 Etch depth calibration on 0.2 mm thick single-crystal diamond at an incident power of $(125 \pm 5)$ mW. Each dip is a single pit, etched for 1 min, taken at set intervals around the focal plane in order to locate the precise focus. The deepest pit will correspond with the position of the focal plane of the objective. The maximum etch depth of 30 nm/min is a significantly faster etch rate than expected from past experience in the group with this laser system. ....	34
Figure 4-3 Clear and characteristic signs of ablation are visible around the Au contacts on the 0.2 mm thick single-crystal diamond film despite being calibrated for a 1 nm deep etch. The Au contact is just outside the field-of-view near the bottom-right corner. ....	35
Figure 4-4 Optical Interferometry (VSI) image of ablation of the 0.5 mm thick single-crystal diamond during etch-rate calibrations using the 5x objective lens and 150 mW incident power. Each oval-shaped ablation crater was formed during a stationary exposure due to the astigmatism in the beam profile. ....	36
Figure 4-5 Etch depth calibration on 0.5 mm thick single-crystal diamond at low incident power. Each significant dip is a single pit, etched for 2 mins, taken at set intervals around the focal plane in order to locate the precise focus. The deepest pit will correspond with the position of the focal plane of the	

objective. The depth of the each etched pit is difficult to determine due to the significant surface roughness of the diamond.....	37
Figure 4-6 SEM image taken at 5kV of diamond ablation induced by a misaligned laser beam scanning across a Au contact. The bright specs scattered across the surface are Au that has been knocked loose by the passing beam. ....	38
Figure 4-7 Narrow channel isolation etch schematic. The yellow areas are the Au contacts; the black line shows the etching path, and hence oxygen-termination around the contacts. The blue area indicates the conducting channel connecting the two contacts where fine control of the surface-termination is desirable. All white space plus the blue area would be hydrogen-terminated surface. The beam would approximately fill one square on the grid using the 5x objective. All measurements are in mm.....	39
Figure 4-8 SEM image taken at 400x magnification and 5kV of a potential isolation etch. A 40 mW UV beam with a waist of 25 $\mu\text{m}$ was traced between the dotted lines. A change in the contrast of the image would indicate a change in the electrical conductivity of the surface and hence a change in the surface termination, but no such change is visible. ....	41
Figure 4-9 SEM image taken at 15kV on EDX mode displaying the location of atomic C, Au and O. An etched channel around the Au should pass between the dotted lines and appear as a track of oxygen-termination but instead the entire region appears to be covered in oxygen. ....	42
Figure 4-10 Optical interferometry scan (PSI) and cross-sectional depth profile of a 0.2 mm long ‘plus sign’ etched on diamond. Total exposure time was 40 min per arm. The depth profile is taken along the red line of the crosshair; the two positions marked are shown along the line. ....	42
Figure 4-11 Resistance change between two Au contacts separated by 0.25 mm with exposure time to a 257.5 nm beam at 40 mW.....	45
Figure 4-12 An attempted etch to isolate two pairs of Au contacts from the other pair whilst maintaining conduction between each pair. Clear signs of ablation are visible under the red outline which depicts the location of the etched track. Despite the ablation, each vertical pair of Au contacts was electrically isolated from the other pair.....	46
Figure 4-13 Optical interferometry scan (PSI) of a small L-shaped etch on the back side of the 0.5 mm thick diamond. The consequence of the elliptical beam profile is evident in the asymmetrical etch depth along each arm.....	47
Figure 4-14 Optical micrograph of a practice ‘FET’ etch on glass. The locations of the drain, source and gate are marked.....	48
Figure 4-15 I-V characteristic of FET 1. Negative Gate Bias 4-48V, max $V_{ds}$ 48V. More data sets were taken which show the same trend but only three are shown here for clarity.....	49
Figure 4-16 I-V characteristic of FET 1 with reduced voltage range. If the FET is modelled with a resistor in parallel, then the linear trend past $\sim 4$ V corresponds to a resistance of $\sim 300$ G $\Omega$ . Several data sets are omitted for clarity. ....	50
Figure 4-17 I-V characteristic of FET 1 for positive gate voltages, after subtraction of the linear trend. ....	50

Figure 4-18 I-V characteristic of FET 1 for negative gate voltages, after subtraction of the linear trend. ....	51
Figure 4-19 I-V characteristic of FET 1 for all measured gate voltages, after subtraction of the linear trend. The positive and negative data sets show self-consistency in the order of the I-V curves however the positive and negative sets are not consistent with each other. ....	51
Figure 4-20 FESEM image of the FET diamond chip; FETS 1-3 clockwise from top left. Dark lines are attributed to induced oxygen-termination by pulsed UV laser etching. The slight distortion in the corners of the image are an artifact of the instrumentation. ....	52
Figure 4-21 FESEM image of the FET diamond chip; ablation craters observed on FET 2 (left) and FET 3 (right). Also (barely) visible in the contrast are the oxygen tracks defining each device. Bright streaks across the images are attributed to surface charging by the electron beam. ....	53

## List of Tables

Table 1-1 Properties of diamond relevant for semiconductor/electrical devices and comparison with silicon and gallium arsenide. ....	3
Table 2-1 Hydrogenation conditions used for the various diamond samples. The ‘plasma temperature’ refers to the temperature the top surface of the diamond was brought to by the plasma. Although the last two entries were only brought to 700°C for a moment, the total exposure time to the hydrogen-plasma was 5 minutes. ....	24
Table 2-2 Source, Drain, & Gate contact materials used for diamond electronic devices .....	25
Table 4-1 Resistance between isolated Au contacts. The offset is the distance between the centre of the beam path and the Au contacts. All resistance measurements were taken at 51% humidity. Resistance measurements in parentheses are follow-up measurements demonstrating the difficulty in repeatability. ....	39
Table 4-2 Partial etch feed-rates and resistance between neighbouring Au contacts measured using a Fluke 45 Dual Display Multimeter. Incident UV beam power: 40±5 mW. Room humidity: 50% .....	40
Table 4-3 Partial etch feed-rates and resistance between neighbouring Au contacts measured using a Keithley 617 Programmable Electrometer. Incident UV beam power: 40±5 mW. Room humidity 56-59%. Un-isolated surface resistance between adjacent contacts: 16 kΩ. Data for feed-rate of 10 mm/min was unavailable as that Au contact had been damaged and there were no other contacts available to repeat the etching as they were designated for other investigations. ....	44
Table 4-4 Resistance measurements between components in the hydrogen-surface channel field-effect transistor devices etched on diamond. Measurements are given for cases where the device is illuminated by the halogen lamp of the microscope and in the dark. Prior to etching the average resistance between adjacent contacts separated by 0.625 mm was 13 kΩ. ....	49



# 1 Introduction

## 1.1 Project Overview

Not long ago diamond was considered merely as an exotic and beautiful material, the purpose of which was decorating the necks and fingers of the affluent and the famous. Wars were fought and paid for by the wealth generated from what is essentially just a regular tetrahedral arrangement of carbon atoms, the sixth most abundant element in the universe. This exotic material is more than just a 'girl's best friend', nowadays it's found on cutting blades, in motor-oil lubricant and even finds potential applications in the quantum [1] and biological life sciences [2]. Of interest here are the properties of diamond which make it particularly interesting for semiconductor devices.

The goal of this project was to demonstrate laser patterned electronics on diamond for the first time; the following sections in this chapter are a review of the literature related to diamond electronics and laser structuring of diamond surfaces. The contrasting conductivity of the two most stable atomic surface-terminations of diamond is what makes the prospect of diamond surface electronics most intriguing. If the (conducting) hydrogen and (insulating) oxygen surface terminations can be accurately and precisely controlled, novel electronic devices may be demonstrated. It has been recently demonstrated that oxygen-terminated diamonds can be machined with micron resolution using an ultra-violet 2-photon desorption technique [3] and it is this technique that this project looked to exploit in order to fabricate micro-scale electronic devices. During this project, factors such as laser writing speed, fluence, and spot size were investigated during UV patterning. The electrical properties of the written structures were investigated with respect to variables such as the size of the structure, the level of electrical isolation required and the etching process itself. The stated goal of the project was to demonstrate the fabrication of simple micro-scale electronic devices such as resistors, capacitors, and transistors on a diamond surface with the ultimate goal of fabricating an entire circuit in the form of a ring oscillator. The outcomes of this project will be of most interest to those working in diamond surface physics and diamond opto-electronics. This chapter will first detail the nature of the diamond surface conduction channel then examine the state-of-the-art with regards to diamond surface electronics, before finally reviewing the process of laser induced desorption, which will be used for both etching diamond and the creation of oxygen-terminated surface regions.

The pulsed UV laser etching process described here shows many advantages over traditional ablation regimes. Pulsed UV laser etching has been shown to proceed at rates largely independent of the facet direction, with only a 20% difference in etch rates between (100) homoepitaxial and polycrystalline diamond [3]. The etched surface is free from graphitic structures [4] and is oxygen terminated [3]. The etched surfaces show surface roughness of the order of several nanometres in contrast to the severe dross and cleavage along the major crystal lattice planes, which is typical of the standard ablation regime [3]. Low surface roughness is crucial in many applications, including improved device performance in electronics. It is these features that make this technique of interest to this project. If oxygen-terminated regions can be quickly and accurately written on hydrogen-terminated diamond then conducting surface tracks can be defined and this presents the prospect for electrical devices to be fabricated on the surface by a direct-write laser process. Furthermore, there are likely many other applications in photonics, biophysics and biophotonics for patterned termination surfaces not considered here.

---

Although there are still unanswered questions regarding the nature of the hydrogen-termination induced surface conductivity, there is clearly potential for the realisation of a commercial diamond semiconductor device as evidenced by the myriad of devices outlined here as well as on consideration of the semiconductor figures of merit. Further, despite an incomplete understanding of the mechanism to date, UV etching may well play a part in future devices for not only fabrication of the device itself but also for writing the entire circuit on the surface of diamond.

## 1.2 Diamond Electronics

The properties of diamond that make it interesting for semiconductor devices are its wide band gap, high thermal conductivity and a high breakdown electric field [5]. Consideration of the material parameters indicate that diamond semiconductor devices are expected to provide the best performance for high power and high frequency requirements [6]. Such considerations include (but are not limited to) the Johnson figure of merit (JFOM), which defines the power-frequency product for a low-voltage transistor [7]; the Keyes figure of merit (KFOM), which describes the thermal limitation to the switching behaviour of the transistor [8]; and the Baliga figure of merit (BFOM), which defines the material parameters to minimise the conduction losses in power field-effect transistors [9]. These three figures are defined in Equation 1-1 to Equation 1-3.

$$JFOM = \frac{E_c \cdot v_s}{2\pi}$$

Equation 1-1

where  $E_c$  is the critical electric field for breakdown and  $v_s$  is the saturated drift velocity.

$$KFOM = \lambda \sqrt{\frac{c \cdot v_s}{4\pi\epsilon}}$$

Equation 1-2

where  $\lambda$  is the thermal conductivity of the semiconductor,  $\epsilon$  is the dielectric constant and  $c$  is the velocity of light.

$$BFOM = \epsilon\mu E_G^3$$

Equation 1-3

where  $\mu$  is the carrier mobility and  $E_G$  is the bandgap of the semiconductor.

On consideration of the figures of merit discussed above, diamond as a semiconductor material appears quite attractive for semiconductor electronics with, for instance, the highest Johnson figure of merit for any semiconductor [5]. The values for the properties mentioned are listed Table 1-1 along with those for Si and GaAs for comparison.

Table 1-1 Properties of diamond relevant for semiconductor/electrical devices and comparison with silicon and gallium arsenide.

Property	C	Si [10]	GaAs [11]
Band Gap ( $eV$ )	5.47 [12]	1.12	1.424
Thermal conductivity ( $W/cm.K$ )	22 [12]	1.3	0.55
Breakdown electric field ( $MV/cm$ )	10 [12]	0.3	0.4
Electron mobility ( $cm^2/V.s$ )	4500 [13]	1400	8500
Hole mobility ( $cm^2/V.s$ )	3800 [13]	450	400
Electron saturation velocity ( $cm/s$ )	$1.5 \times 10^7$ [14]	$\sim 1 \times 10^7$	$\sim 2 \times 10^7$
Hole saturation velocity ( $cm/s$ )	$1.1 \times 10^7$ [14]	$\sim 1 \times 10^7$	$\sim 1 \times 10^7$

Despite these advantages, doping remains an issue. Because of the small lattice constant of diamond, most doping elements lead to severe distortions of the unit cell and are difficult to incorporate. The only deep acceptor available for doping is boron, and this is only partially activated at room temperature [15] with an activation energy  $\Delta E_a = 0.37 eV$  [16]. This activation energy is lowered with greater levels of doping and, in fact, it becomes negligible at concentrations of the order  $10^{20} cm^{-3}$  [17] where upon it forms a miniband and enables ohmic contacts by tunnelling [16]. However for field-effect transistor (FET) devices, the sheet charge in the transistor channel needs to be limited to nanometre-thin channels which are able to be pinched-off easily by the gate prior to breakdown. This requires monolayer doping and growth control. Furthermore, n-type doping has not been shown to be effective enough to produce high electron densities [15]. The only dopant shown to reproducibly produce n-type conductivity has been phosphorus [18]. However, its use is limited due to it incorporating during growth on (111) lattice planes, making defect-free growth difficult [19]. Nitrogen is not activated at room temperature with an activation energy of  $\Delta E_a = 1.7 eV$  although it is used to obtain semi-insulating characteristics as well as being incorporated into FET structures to create Metal-Insulator-Semiconductor-like pn-junctions, where the nitrogen doped part represents a lossy gate dielectric [16].

It has been found however, that hydrogen-termination on the surface of diamond creates a sub-surface p-type doping effect [20]. Such sub-surface layers show room temperature activated hole conduction of  $\approx 10^{13} cm^{-2}$  sheet charge [21]. This channel closely follows the surface topography of the diamond and is considered a two-dimensional hole gas (2DHG) [22]. This carrier density is sufficient for room temperature FET operation. Due to surface band bending, carriers are confined to a 5 nm depth, which means that device isolation is easily achieved because the bulk diamond itself is insulating [23]. Furthermore, H-terminated surfaces can be separated by oxygen-terminated regions as such surfaces are highly insulating due to surface potential pinning [24], i.e. active and passive areas of the semiconductor device are defined by the surface termination of the diamond.

### 1.3 Diamond Surface Conduction Channel

The first reports of hydrogen-termination induced conduction came from Landstrass & Ravi (1989) where it was reported that diamond films, as grown by plasma chemical vapour deposition, show fairly low resistivity [25]. The authors found that the resistivity increased by up to six orders of magnitude upon annealing at high temperature, whereas it was again reduced with a subsequent hydrogen plasma treatment. The authors postulated that the hydrogen-termination on the surface was responsible for the passivation of deep traps in the films and that dehydrogenation resulted in the electrical activation of these traps, leading to an increase in the resistivity [25]. It was therefore assumed that hydrogen was directly responsible for the hole accumulation layer that is observed in hydrogenated diamond through the formation of unspecified defects that act as acceptors [26]. It has since been shown that although hydrogen is necessary for surface conductivity, it is not sufficient on its own.

Maier et al. (2000) measured the conductivity in air and under an ultrahigh vacuum of various H-terminated diamonds [27]. The authors reported that the conductance of homoepitaxial (100) diamond dropped five orders of magnitude when placed in an ultrahigh vacuum but returned to its previous conductance upon re-exposure to air. The authors exposed one-half of a diamond film to an electron beam, which removed the hydrogen termination, and the conductance of both halves was measured in the ultrahigh vacuum and upon re-introduction to the atmosphere. As shown in Figure 1-1 both the hydrogenated (masked) and non-hydrogenated (irradiated) sections displayed minimal conductance in ultra-high vacuum (UHV). Upon exposure to the atmosphere, however, the hydrogenated surface showed an increase in conductance of 5 orders of magnitude whereas the conductance of the non-hydrogenated surface remained constant.

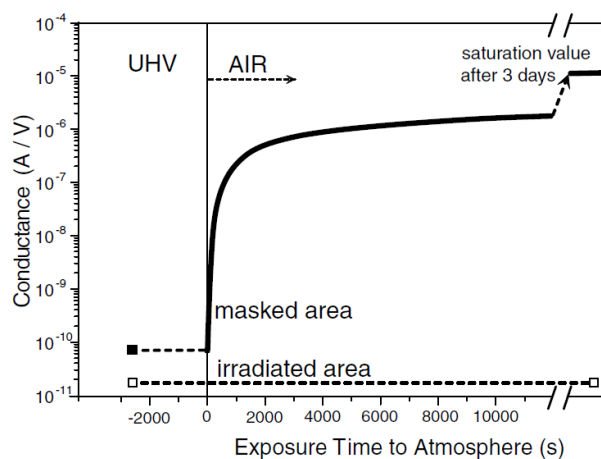
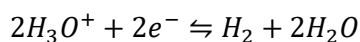


Figure 1-1 Surface conductance of the hydrogenated (masked) and the hydrogen-free (irradiated) part of a homoepitaxial diamond (100) layer in UHV and during exposure to air. Image credit: [27]

It therefore becomes clear that although hydrogen is necessary for surface conductivity, an additional component provided from the air is required. The authors proposed that a thin water layer, which would form naturally from exposure to the atmosphere, provides the electron system that acts as a surface acceptor. In the proposed model, hydrogenation raises the valance band maximum (VBM) of the diamond with respect to the vacuum level and leaves it just above the chemical potential of a mildly acidic water layer (due to dissolution of atmospheric gases, particularly  $\text{CO}_2$ ) physisorbed at the surface. Electron exchange from the diamond to the water layer is then governed by a redox reaction:





While the chemical potential of electrons in the liquid phase is less than the Fermi level, electrons will be transferred from the diamond to the water layer and push the redox reaction to the right. The holes left in the diamond form the accumulation layer, which induces surface band bending, thereby raising the chemical potential. A schematic picture of the hydrogenated surface with the adsorbate layer is shown in Figure 1-2 where we see depicted the self-ionisation of water molecules and the dissolution of carbon dioxide to form carbonic acid.

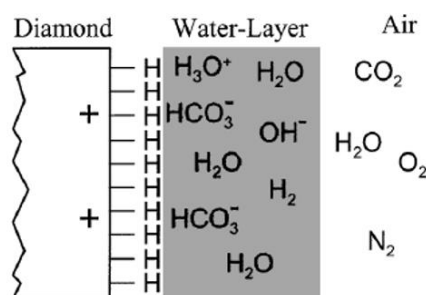


Figure 1-2 Schematic picture of the hydrogenated diamond surface in contact with a water layer as it forms in air. Image credit: [27]

This model has been supported qualitatively by Foord et al. (2002) who reported on the influence of gaseous and solution phases on surface conductivity [28]. The authors were able to measure the conductivity of the sample from inside the hydrogenation reactor where analytical grade vapours and gases could be pumped in. Dry air was admitted into the chamber with and without first exposing the diamond surface to water vapour. It was observed that exposure to dry air increased the surface conductance but only when the hydrogenated surface was exposed to both moisture and atmospheric gases do we see the highly conductive surface state, i.e. moisture or atmospheric gases alone do not produce the highly conductive surface. The authors' note that the chemisorption of the common atmospheric components on diamond is minimal and their vapour pressures are too high for significant physisorption, however physisorption of water enables the subsequent dissolution of the gases.

Further support for the "wetting layer" model is also provided by Foord et al. (2002) who report on the conductivity of hydrogenated diamond surfaces exposed to acidic and alkaline solutions. It was found that the surface conductance of the diamond films when submerged in solutions with a pH of less than 1 were comparable to those measured prior to insertion into the acidic solution. However, the conductance decreased when the diamond films were submerged in alkaline solutions (pH 13). Foord et al. also note that oxygen itself is effective at promoting surface conductivity in the "wetting layer" however nitrogen is not due to a lack of nitrogen reduction couples with sufficiently positive electrochemical potentials.

The negative electron affinity of the hydrogenated surface and associated p-type surface conductivity are two features unique to diamond among all semiconductors [29]. Several other models have been proposed to explain this phenomenon including shallow hydrogen-induced acceptors [30], and deep-level passivation by hydrogen [31] however it does appear that surface band bending due to hydrogen surface-termination where valence-band electrons transfer into an adsorbate layer (the so-called transfer doping model) is the best explanation [22], [32].

This charge transfer has also been studied using first-principles Density Functional Theory (DFT) by Petrini et al. (2007). The authors' showed that the electron transfer takes place from the diamond surface to the reducible species when oxonium ions, molecular oxygen, or ozone is present in the adsorbate layer [33]. Their modelling also show that electron transfer does not occur when only water is present in the adsorbate layer. Further, their modelling also showed that the electron transfer effect is greatly enhanced when molecular oxygen or ozone is present in the water film along with oxonium ions (i.e. hydronium ions). Furthermore, when oxygen was included with oxonium ion, the observed effect on the electron transfer became much more pronounced than predicted by the simple addition of values for individual effects. This is supported by the observation of reduced surface conductivity when the surface is exposed to deoxygenated water [28].

To improve the performance of any potential diamond surface electronic device, a greater understanding of the conduction mechanism as well as the identification of specific adsorbates is required. For instance, Kubovic et al. (2010) have shown that  $\text{NO}_2$  gas may be used to increase the surface conductivity [34] and Ley et al. (2006) have demonstrated that the chemical potential of highly fluorinated fullerenes also makes them suitable for an aqueous adsorbate layer. Further, Russell et al. (2013) has shown that coating the diamond surface in  $\text{MoO}_3$  facilitates the surface transfer doping while providing a more stable adsorbate layer as well as a substantial increase in the hole carrier concentration [35].

To summarise: In the transfer doping model, valence band electrons move into empty electronic states of an adjacent adsorbate layer. The adsorbate layer must have its lowest unoccupied electronic level below the valence-band maximum of diamond in order to act as sink for electrons [29]. Under standard atmospheric conditions, the pH value of water is about 6 due to dissolved atmospheric gases (namely  $\text{CO}_2$ ). The chemical potential  $\mu_e$  for such an aqueous wetting layer has been calculated to be  $-4.26$  eV [27]. Taking into account the negative electron affinity  $\chi$  of  $-1.3$  eV for a hydrogenated diamond surface, the pinning position of the Fermi-level  $E_F$  at the water–diamond interface would be 50 meV below the valence band maximum, which is enough to generate a hole accumulation layer at the surface of diamond [29]. This band bending is depicted in Figure 1-3.

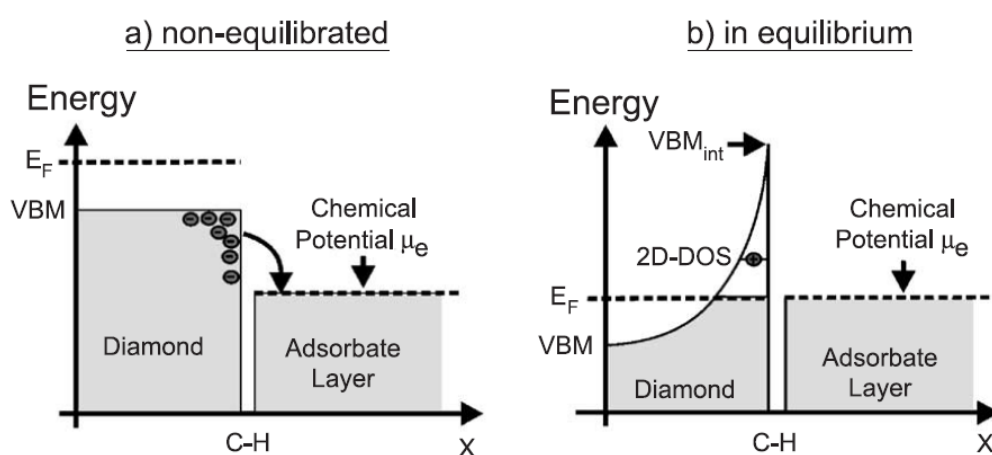


Figure 1-3 Schematic drawing of the diamond/adsorbate heterojunction for the (a) non-equilibrated and (b) equilibrated case. Electrons from the valence-band diffuse into empty electronic states of the adsorbate layer as long as the chemical potential  $\mu_e$  is lower than the Fermi energy  $E_F$ . Image credit: [29]

## 1.4 Review of Diamond Surface Devices

This section will detail the basic design and manufacture of diamond field-effect transistors to contrast and compare with the direct-write procedure attempted here. Field-effect transistors (FET) come in various forms but all perform two functions: (1) voltage-controlled switches and (2) voltage-controlled current sources. These functions form the essential building blocks of digital circuits and allow the construction of linear amplifiers respectively [36]. In one variation of the field-effect transistor, a slab of p-type semiconductor is made with two n-type regions on top called the ‘source’ and ‘drain’ with a metallic conductor deposited on top of each region as shown in Figure 1-4. The third electrode on a FET is called the ‘gate’ and may have an insulator layer between it and the semiconductor, as in Metal-Oxide-Semiconductor (MOSFET) or Metal-Insulator-Semiconductor (MISFET) devices, or the electrode may be deposited directly onto the surface of the semiconductor, as in Metal-Electrode-Semiconductor (MESFET) devices. The decision to include an insulating layer will depend on the function of the device and the size of the integrated circuit.

In the case of the MOSFET shown in Figure 1-4, if there is no charge on the gate, there will be very little current flowing from source to drain when a potential difference is applied between them as one of the p-n junctions is reverse biased. If a positive charge is placed on the gate, the few electrons that are present in the p-type material will be attracted towards the gate. The enhanced concentration of electrons between the two junctions will permit current to flow between the source and the drain. The current is very sensitive to the gate charge and potential, and the device functions as an amplifier [37] or as a switch as the gate potential may be tuned to cut-off the current or allow it to flow.

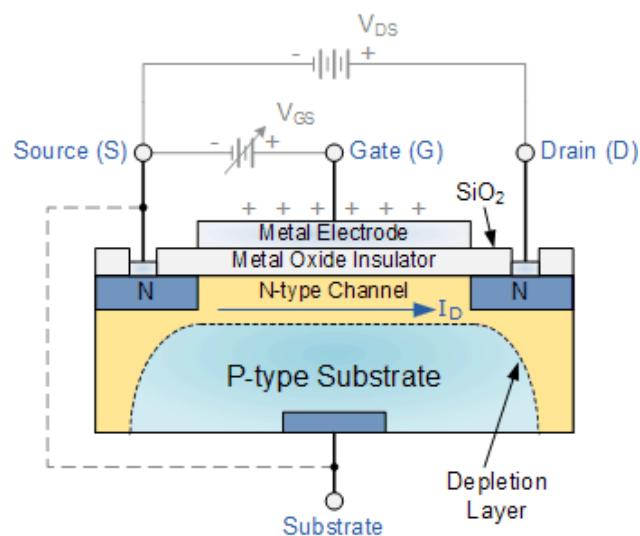


Figure 1-4 Metal-Oxide-Semiconductor Field-Effect Transistor (MOSFET). Image credit: [38]

The FET depicted in Figure 1-4 is not the only way a FET may be constructed; the p- and n-type regions in Figure 1-4 may be interchanged or a myriad of other designs may be employed depending on the design specifications required. Transistors fabricated using the pure p-type sub-surface of hydrogen-terminated diamond will be described later in this section. However the transistor may be constructed, all fall into one of two groups: (1) Depletion-Type, and (2) Enhancement-Type.

Enhancement-type transistors are the most common and they require the Gate-Source voltage to switch the device “ON” i.e. the gate potential is required for current to flow from source to drain. Conversely, a depletion-type transistor requires the gate-source voltage to stop the flow of current

from source to drain and switch the device “OFF”. All diamond transistors using the hydrogen-termination induced sub-surface channel are depletion type transistors as the conduction channel is ever present and will require a gate voltage to close it.

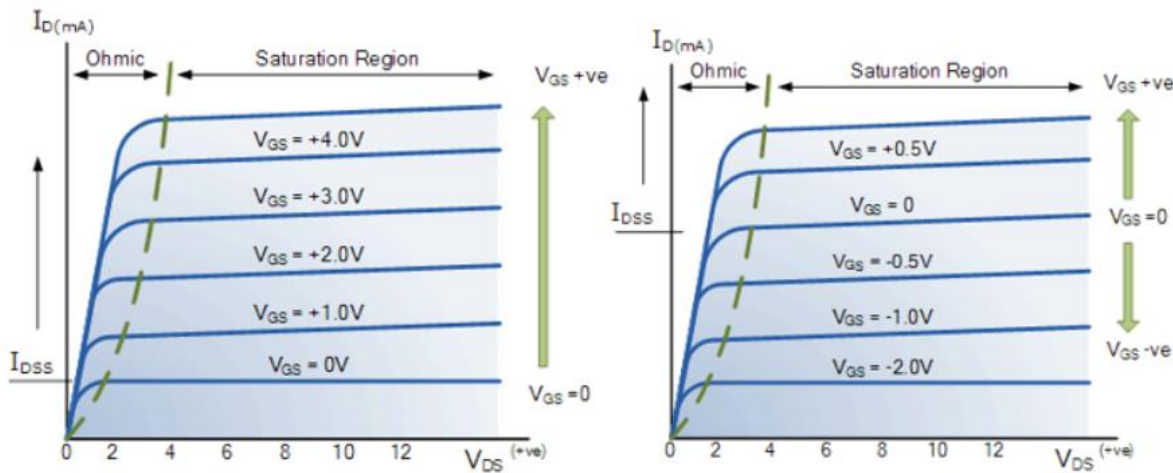


Figure 1-5 LEFT: Enhancement-type FET. RIGHT: Depletion-type FET. Each I-V curve is for a separate gate voltage. Image credit: [38]

Figure 1-5 depicts the difference between the current-voltage (I-V) characteristics of enhancement and depletion-type transistors where the majority carriers in the conduction channel are electrons, hence increasing the positive gate-voltage will attract additional negative-charge carriers into the channel and therefore increase the current. As the gate voltage influences the number of carriers in the channel, there is a separate curve shown for each gate-voltage explored. The source-drain current ( $I_{ds}$ ) is often written in terms amperes/unit length, as the current is proportional to the width of the channel. Note that for the depletion-type device in Figure 1-5, there is significant source-drain current flow when the gate-voltage ( $V_{gs}$ ) is zero. Such a device would require a negative gate-voltage in order to switch the device off.

Note the ‘saturation region’ in Figure 1-5 as the source-drain voltage ( $V_{ds}$ ) is increased, the lateral electric field in the channel is increased eventually becoming stronger than the vertical electric field due to the gate voltage. Under these conditions the gate field is unable to keep the charge carriers in the channel as they are swept out by the source-drain field. At this stage, the drain current is controlled by the gate voltage which influences how many carriers are in the depletion region and the transistor acts as a voltage-controlled current source [36].

Depending on the device and its intended use, there will be different output power and operational frequency requirements, which will dictate the material requirements of the device. This is illustrated in Figure 1-6, which shows the power and frequency requirements for various wireless communication devices and the semiconductors that can or are expected to fill those requirements.

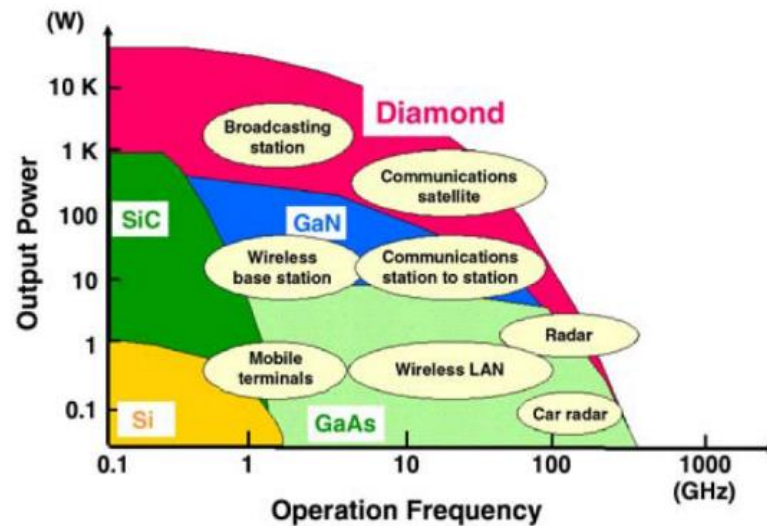


Figure 1-6 Requirements for RF high-power devices and the capability of semiconductors to meet them. Image credit: [5]

As illustrated in Figure 1-6: broadcasting stations, communications satellites, and radars require output powers and frequencies that are unattainable with conventional semiconductor devices. These devices still rely on vacuum tubes, and it is expected that diamond transistors will replace them in the future provided they can be fabricated to operate in this regime [5]. Several groups have reported on early devices operating in this regime such as Russell et al. (2012) who reported on the RF performance of 50 nm gate length H-terminated homoepitaxial diamond FETs with an extrinsic cut-off frequency of 53 GHz [39]. The authors' further report a calculated intrinsic cut-off frequency of 90 GHz, highlighting the need for engineering controls to minimise resistance and maximise operational frequency. Other H-terminated diamond FETs have achieved cut-off frequencies of 45 GHz for 100 nm and 150 nm gate lengths [40].

A number of approaches have been made towards realising a diamond-based transistor. Russell et al. (2012) began with a clean CVD diamond film and hydrogen-termination of the surface was achieved in a high-power hydrogen plasma for 30 min at 580 °C [39]. Contacts to the diamond surface were formed by depositing an 80 nm thick Au metal layer to form the ohmic contacts and to protect the diamond surface during the device processing. Each subsequent stage was patterned using PMMA resist and an electron-beam lithography device. The device was electrically isolated by exposing the diamond surface to oxygen plasma after the removal of the Au layer by a  $KI/I_2$  wet etch. The gate lines were written by electron-beam lithography and wet etched to form the ohmic contacts. A 25 nm Al/25 nm Au gate metal was then deposited through the same mask directly onto the exposed diamond. The DC characteristics for this device are shown in Figure 1-7. An initial DC measurement with zero gate bias was reported with a maximum drain current of 225 mA/mm at  $-10\text{ V } V_{ds}$ . Interestingly it was also reported that subsequent measurement with a gate bias applied between  $-2\text{ V}$  and  $+4\text{ V}$  demonstrated good transistor action but led to a shift in the drain current to a reduced value of 170 mA/mm (see Figure 1-7), however the DC characteristics of the device then remained stable during repeat measurements. The authors do not discuss a possible mechanism for this surprising behaviour but presumably it would be due to trapped charge at the gate interface prior to first operation. This behaviour is similar to that observed in FET structures fabricated during this project.

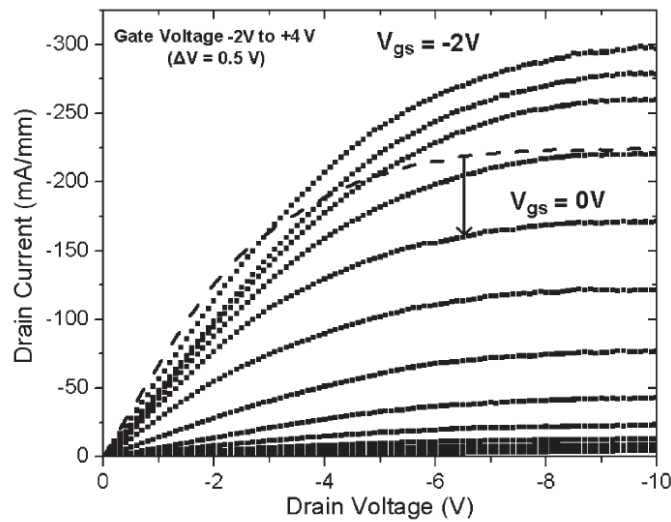


Figure 1-7 DC output characteristics of a 50 nm gate length H-termination diamond FET. The dashed line indicates initial measurement of  $I_d$  prior to application of the present gate voltage range. Image credit: [39]

Gluche et al. (1997) has reported on two device geometries: a planar circular device structure with a gate length of 8.5  $\mu\text{m}$  and 500  $\mu\text{m}$  effective gate width (see Figure 1-8) and a single gate rectangular device with a gate length of 3.0  $\mu\text{m}$  and a 100  $\mu\text{m}$  gate width [21].

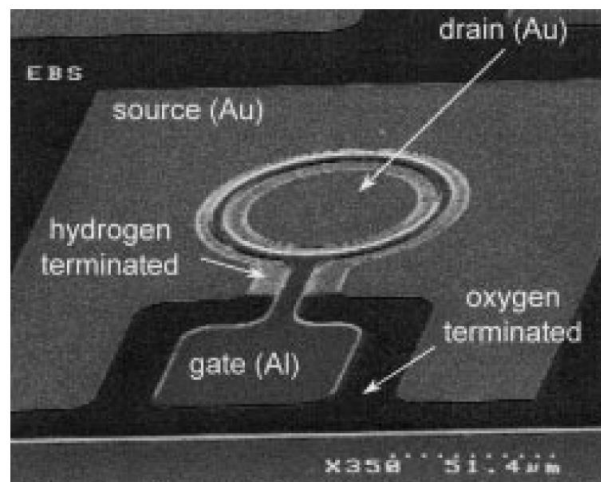


Figure 1-8 SEM micrograph of circular FET structure. The bright areas are the active areas with hydrogen terminated surface. The dark areas are the insulating oxygen passivated surrounding areas. Image credit: [21]

Both devices were fabricated from 100 nm thick CVD grown homoepitaxial films. The growth conditions resulted in a hydrogen-terminated type 1b single-crystal diamond. The authors chose Au for the source and drain contacts as it has a high electronegativity and thus a small electronegativity difference to diamond; Al was chosen for the gate contact as it has a small electronegativity. The contacts were fabricated using evaporation and patterning by wet chemical etch back and substitution of the surface hydrogen was achieved by oxygen plasma treatment. The DC characteristics of both devices are shown in Figure 1-9. A similar method was used [5] by Kasu et al. (2007) to fabricate the



contacts as well as being of similar geometry to the single gate structure and is illustrated schematically in Figure 1-10.

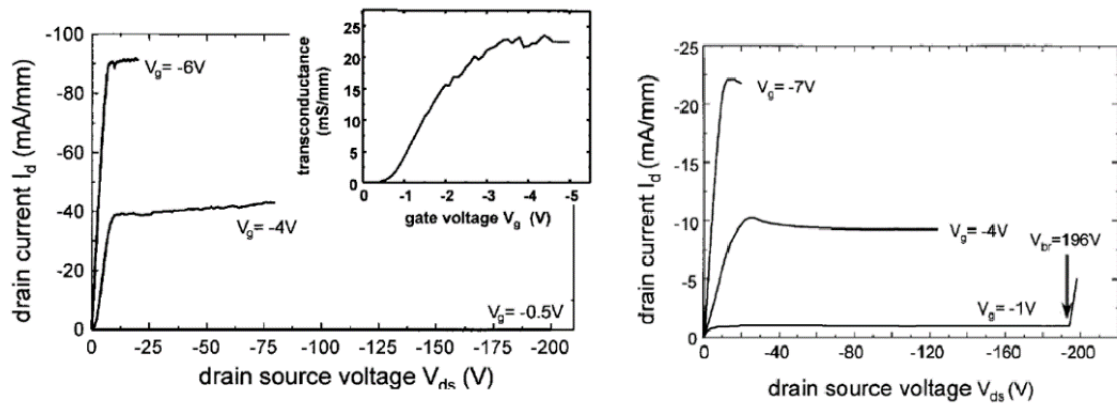


Figure 1-9 DC characteristics of; LEFT: rectangular FET structure  $L_g = 3.0 \mu\text{m}$ ,  $W_g = 100 \mu\text{m}$ ,  $L_{ds} = 12 \mu\text{m}$ . The insert shows the transconductance versus gate bias. RIGHT: circular FET structure.  $L_g = 8.5 \mu\text{m}$ ,  $W_g = 500 \mu\text{m}$ ,  $L_{ds} = 50 \mu\text{m}$ . The breakdown voltage shown was destructive. Image credit: [21]

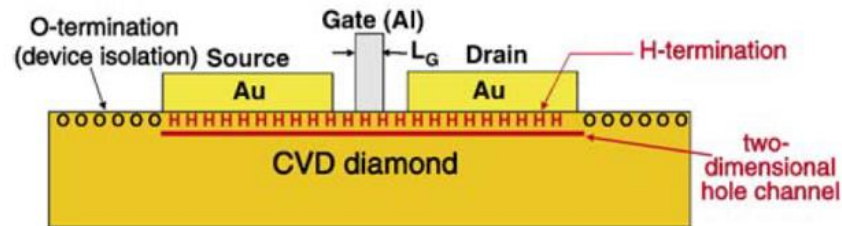


Figure 1-10 Schematic diagram of H-terminated diamond FET. Image credit: [5]

Similar structures to those discussed above have also been fabricated on polycrystalline diamond films. Calvani et al. (2009) reported on butterfly-shaped FET structures that had been fabricated on polycrystalline films grown by microwave plasma CVD [41]. Again, Au is used for the source and drain contacts and Al for the gate contact. The device was isolated by Reactive Ion Etching (RIE) in oxygen and argon plasma. Calvani et al. (2009) reported on metal-semiconductor field effect transistors (MESFETs) with a grain size in the range  $100\text{--}200 \mu\text{m}$  and found the DC behaviour on the MESFETs largely unaffected by the grain size. The RF performance on the other hand showed significant improvement on the larger grain size diamond and the authors noted the importance of device structures with channel lengths smaller or equal to the average grain size.

Calvani et al. (2009) also reported that devices realized on high quality diamond sample showed a maximum drain current of  $120 \text{ mA/mm}$  in DC and pulsed current regimes as well as a maximum transconductance of  $50 \text{ mS/mm}$  [41]. Likewise Ueda et al. (2006) also reported on FET devices with a similar structure to Figure 1-10 on polycrystalline diamond with an average grain size of approximately  $100 \mu\text{m}$  which is comparable to the size of the transistor itself [40]. The authors report a drain current approximately 50% higher than their previous values for single-crystal CVD diamond FETs, which they attribute to a decrease in the source-gate gap. Further, they report that the drain leakage, which is

often observed in FETs using single-crystal CVD diamond, was not observed in the polycrystalline FETs [40].

Ueda et al. (2006) cite as a reason for using polycrystalline diamond, which is also discussed elsewhere (see for example [5] & [15]), that the size of homoepitaxial diamond is limited to that of the High-Pressure High-Temperature (HPHT) substrate, 4 mm x 4 mm, and its size cannot meet the requirement of the wafer size, which is at least 4 inches. High quality polycrystalline diamond can however meet that requirement. Furthermore Kasu et al. (2007) report that the maximum drain current is 1.5 times higher than that of a conventional homoepitaxial diamond FET which indicates that 1) the crystal quality of the polycrystalline diamond is better than that of the homoepitaxial diamond and 2) that its grain boundaries have little influence on the FET performance [5].

Single electron FETs on p-type diamond are also an active area of fundamental research. Two separate device geometries will be discussed here although both are structured by the same process: a direct-write oxidation of the diamond surface using an atomic force microscope (AFM). Figure 1-11 shows an AFM image of a single-hole transistor on p-type diamond fabricated by nanoscale oxidation using the conductive probe of an AFM as reported by Tachiki et al. (2002). From an H-terminated surface, the regions of p-type conduction can be electrically isolated very precisely by selectively oxidising the surface to create O-terminated insulating regions through the application of a positive voltage between the conductive probe and the surface [23]. This ability to write complex patterns into the surface termination, albeit using laser techniques as opposed to a scanning probe, is also the fundamental research angle of the work undertaken during this project.

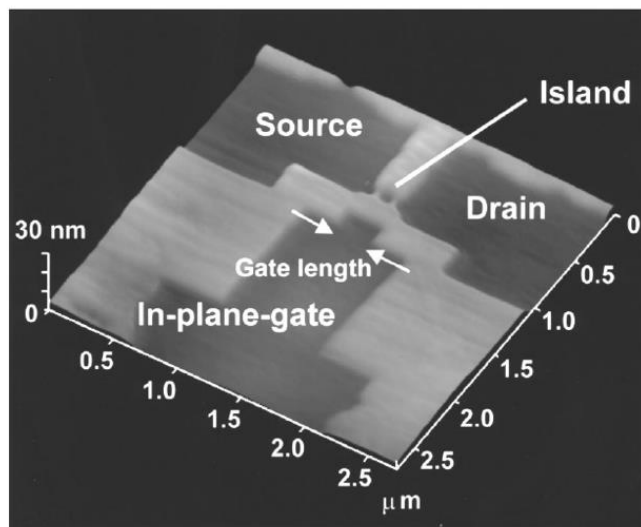


Figure 1-11 AFM image of diamond single-hole transistor. Bright and dark regions represent locally oxidized (O-terminated) and H-terminated regions, respectively. Image credit:[23]

Further in [42], Banno et al. (2002) also used local anodisation using an AFM to form a narrow oxide line along the path of the scanning tip.



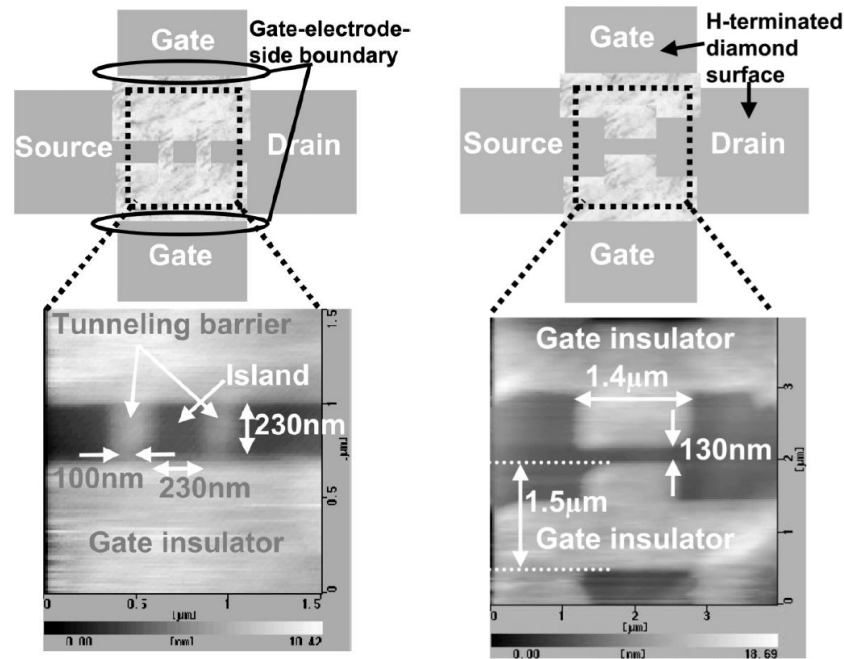


Figure 1-12 Schematic and AFM image of; LEFT: single-hole transistor, RIGHT: a dual side-gated FET. Both structures are formed by local anodisation of the H-terminated surface by applying a positive voltage between the AFM cantilever tip and the diamond substrate. Image credit: [42]

These techniques (local oxidation using an AFM) were originally developed for more traditional semiconductor materials however unlike other materials, the oxidation of diamond is controlled to a single atomic layer which results in much greater resolution [23]. The  $I_{ds} - V_{gs}$  characteristics for the in-plane-gate transistor [23] are shown in Figure 1-13. Oscillation peaks with intervals of 1.4 V are clearly seen at an operational temperature of 77 K however the noise level is reported to become high at room temperature. Assuming each oscillation corresponds to the movement of a single electron, the self-capacitance of the island was estimated to be  $\sim 10^{-18} F$  [23].

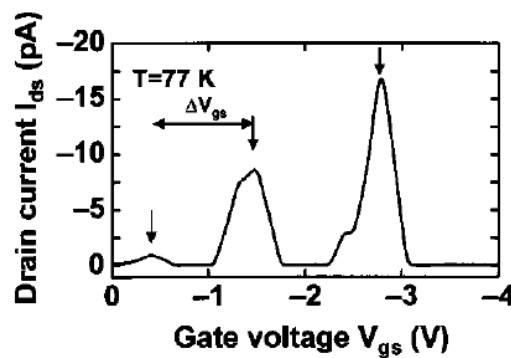


Figure 1-13  $I_{ds} - V_{gs}$  characteristics of a diamond single-hole transistor at 77 K.  $V_{ds}$  is -50 mV. Coulomb oscillation is observed with distinct peaks at 1.4 V intervals ( $\Delta V_{gs}$ ). Image credit: [23]

The electrical characteristics of the two devices presented in [42] (depicted in Figure 1-12) are presented below in Figure 1-14 and Figure 1-15. Operating at room temperature, the threshold voltage of the dual side-gated FET was noted to be approximately +2V and in the linear operation region the sheet resistance was calculated to be 35 kΩ/square. The gate leakage is 32 nA at  $V_{gs} =$

$-20\text{ V}$ . The  $I_{ds}$  is suppressed to less than  $10\text{ nA}$  in the lower negative drain voltage range when operated at  $4.4\text{ K}$ . This is due to the non-negligible barrier height of the Au contacts to the H-terminated surface at such low temperatures.

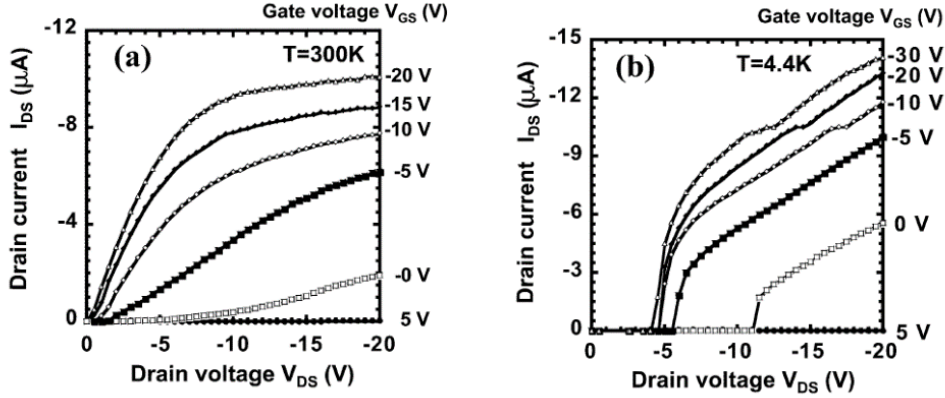


Figure 1-14  $I_{ds} - V_{ds}$  characteristics of a side-gated FET. (a) Measured at room temperature. (b) Measured at  $4.4\text{ K}$ . Image credit: [42]

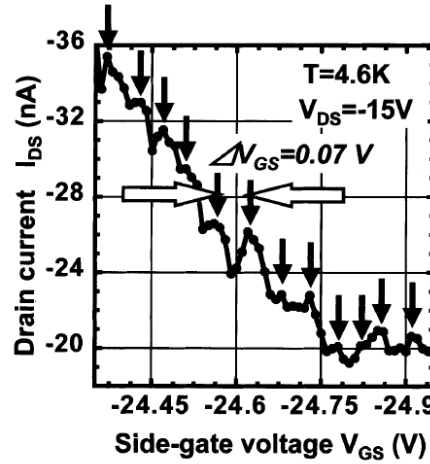


Figure 1-15  $I_{ds} - V_{gs}$  characteristics measured at  $4.6\text{ K}$ .  $V_{ds} = -15\text{ V}$ . Image credit: [42]

The single-hole transistor in Figure 1-12 was fabricated by combining the dual side-gated FET with the AFM anodised lines as tunnelling barriers to control the island potential [42]. Figure 1-15 shows several equally spaced current peaks separated by  $0.07\text{ V}$  and these current oscillations are interpreted as a Coulomb blockade effect. The heights of the peaks tend to be irregular in the Coulomb oscillations of a semiconductor quantum dot when there is no magnetic field [43].

In closing, a number of device geometries and fabrication methods found in the literature have been summarised and explored. In contrast to the devices discussed above, the FET devices investigated during this project were fabricated using a direct-write pulsed UV laser process, which will be detailed, in the following section.

## 1.5 UV Laser Etching of Diamond

It is well established that diamond is transformed into graphite at elevated temperatures (dependent on ambient pressures). With sufficient energy the  $sp^3$  (tetrahedral) bonded carbon atom in the diamond lattice can undergo a structural rearrangement and move into the  $sp^2$  (hexagonal) state which has a smaller binding energy [44]. It is this feature of diamond that allows it to be laser-processed via a mechanism unique to diamond; graphitic transformation of diamond is induced by the leading part of a laser pulse, allowing the remainder of the energy to be absorbed more efficiently and heating the surface to the temperature of sublimation. An ablation of graphitic material will take place such that a crater is formed in the irradiation zone [44]. However, pulsed ultra-violet laser regimes have been identified where very low rates of etching occur in the absence of graphitisation. Kononenko et al. (2003) found that under low irradiance conditions, laser etching of ion-implanted diamond was taking place at a rate of  $10^{-3}$  to  $10^{-4}$  nm/pulse, with a dependence on the implantation dose [45]. They also found that an even lower rate of etching was occurring ( $\sim 10^{-5}$  nm/pulse) during KrF laser irradiation of a natural single crystal diamond. It was supposed at this time that the graphitisation of a few surface monolayers occurred at relatively low irradiance via non-thermal interactions and that the removal of carbon atoms from the surface would take place via chemical reactions with oxygen in the air or direct photon-induced sublimation [45].

The same research group followed up by irradiating a diamond surface with an KrF excimer laser, operating at 248 nm with 15 ns, 400 mJ pulses and a repetition rate of up to 100 Hz [4]. A short-focus lens was used to bring an image of the uniformly illuminated square mask onto the surface with an area of 50-100  $\mu\text{m}$  on the side and the laser fluence at the sample surface was kept constant within the radiation spot. The extremely low etching rates, to the order of less than 1 nm/1000 pulses, have inspired the term *nanoablation* for this process, however this term will be avoided in favour of *UV etching* as this process will be shown to be very different from ablation and in-fact more akin to photon-induced desorption. Figure 1-16 shows the image of the 70-nm deep crater formed at the surface of a single crystal diamond after irradiation by 100,000 laser pulses through the mask in the absence of any visible surface graphitisation [4].

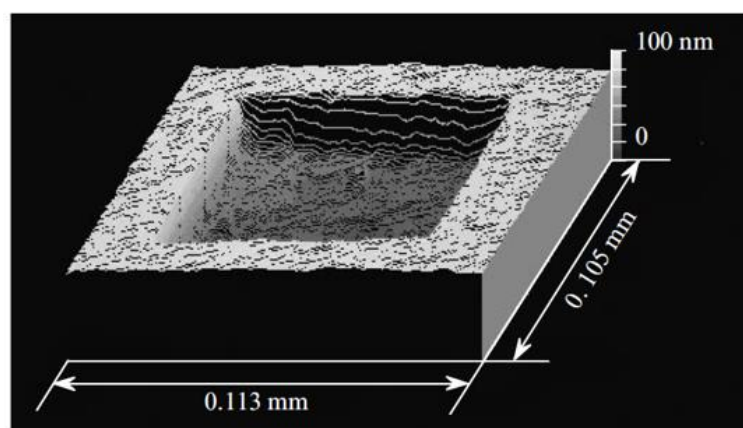


Figure 1-16 Image of a single-crystal diamond surface obtained after irradiation by 100,000 pulses from a KrF excimer laser (laser fluence  $10 \text{ J}/\text{cm}^2$ , intensity  $10^9 \text{ W}/\text{cm}^2$ ). Image credit: [4]

The authors investigated the dependence of the etch rate on the fluence and their results are shown in Figure 1-17. The removal rate of material was determined from the slope of the corresponding

straight line corresponding to each laser fluence and the dependence of the UV etching rate on the laser fluence was obtained. A maximum UV etching rate at room temperature was then extrapolated to be approximately 0.7 nm/1000 pulses, limited by the development of traditional ablation at a laser fluence of approximately  $14 \text{ J} \cdot \text{cm}^{-2}$  for the sample used.

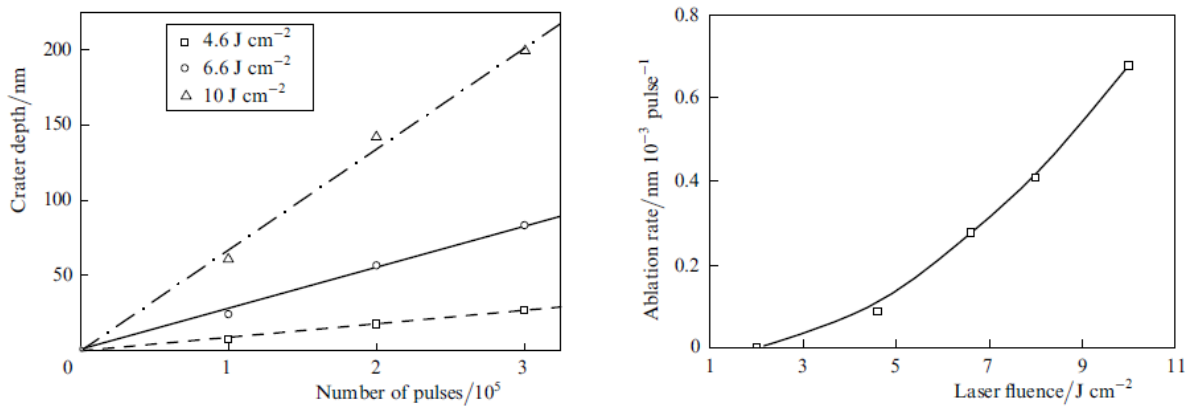


Figure 1-17 LEFT: Dependence of the etching depth on the number of radiation pulses for different laser fluencies in the laser spot. RIGHT: Dependence of the laser nanoablation rate on the laser fluence at room temperature. Image credit: [4]

This effect has since been observed using other UV lasers; during operation of a deep ultraviolet diamond Raman laser, Granados et al. (2011) observed the output power of the diamond Raman laser to decrease by a factor of 2 over a 10 minute period [46]. Throughout the decrease in laser performance a flaring of the pump beam profile was observed upon exiting the diamond, indicating a significant refraction by the diamond. Surface profiling by optical interferometry showed very shallow pits on both entrance and exit facets as shown in Figure 1-18. The authors report that after 10 minutes of operation the typical pit depth was approximately 50 nm and, through measurements at one minute intervals, established that the rate of removal was roughly constant with exposure duration. The average removal rate per pulse was reported to be  $1.4 \times 10^{-8}$  nm or 395 carbon atoms i.e. many orders of magnitude fewer than the number of surface atoms exposed to the pump beam. Further, they report that by reducing the pump intensity by a factor of 10, the ablation rate correspondingly reduced by a factor of 30, indicating a multi-photon process. Multi-pulse effects were presumed to be negligible due to the relaxation times of free carriers and surface temperature gradients being shorter than the interpulse period [46].

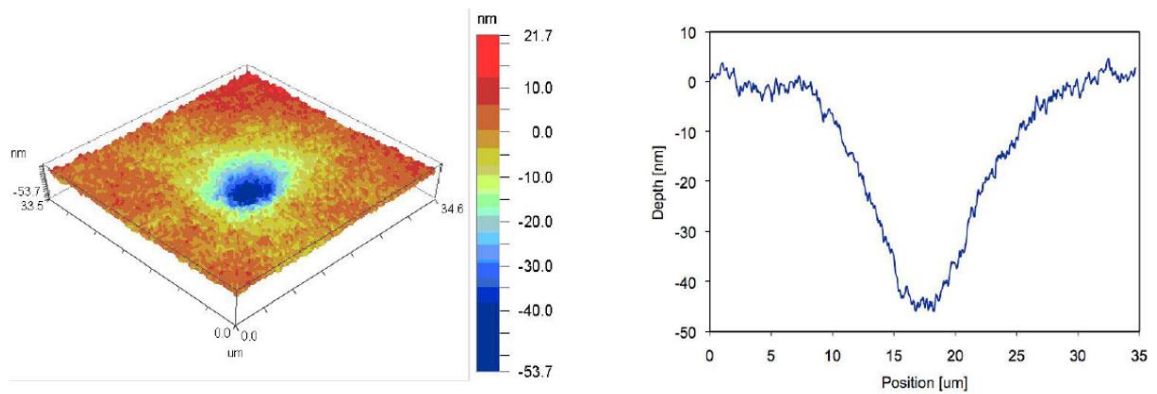


Figure 1-18 Interferometric optical profile image of the surface pit after exposure to  $3.6 \times 10^{10}$  pulses of energy 10 nJ. The cross-section through the deepest point is shown to the right. Image credit: [46]

The same research group followed up by investigating how irradiance influences the rate of etching as well as investigating the properties of the etched surface [3]. A clean type IIa single crystal diamond was etched with a 266 nm wavelength beam at 300 mW and a spot size of approximately 5  $\mu\text{m}$ . The fluence/exposure time was then altered and the resulting surface characterised with optical surface interferometry for surface roughness and etch depth; near edge x-ray absorption fine structure (NEXAFS) was used to characterise the surface chemistry [3]. Figure 1-19 shows a pair of microscopy images of the surface after being exposed to irradiances 1.1 and 0.6 times the threshold for laser ablation. These images really illustrate the difference between laser ablation and UV etching.

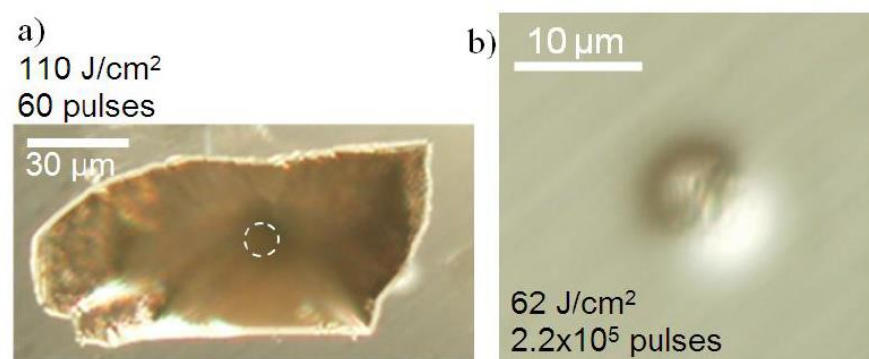


Figure 1-19 Microscope images of the diamond surface subsequent to exposure at a) 1.1, b) 0.6 times the ablation threshold. The exposure times were 0.05 s and 30 s, and the crater depths 30  $\mu\text{m}$  and 0.60  $\mu\text{m}$  respectively; the pulse rate was 7.5 kHz. In a), the beam size is indicated by the dashed circle. For b) the contrast was enhanced using differential interferometric contrast mode. Image credit: [3]

Above the ablation threshold, pits 10 times the beam width were reported which exhibited cleavage along the major crystal planes and dross typical of explosive ejections, very much in line with what would be expected from traditional ablation. In contrast, below the ablation threshold, the rate at which material is removed is orders of magnitude slower, with etched pits of depth less than 1  $\mu\text{m}$  and of similar diameter to the incident beam. Furthermore these etched pits appear on the front and back of the sample, where the beam focus interacted with each surface. The authors investigated the pit depth as a function of the exposure time and found a linear trend, implying that the etch depth is proportional to the number of cumulative pulses. The pits are reported to be approximately Gaussian

shaped through vertical scanning interferometric measurements. The pit width was reported to be narrower than the beam width and more closely following the square of the beam profile.

The etch rate as a function of pulse fluence was investigated by the authors and is shown in Figure 1-20. This was done by varying the time period for etching and using the results obtained for the etch depth as a function of exposure time. A least squares regression showed an  $(I_p)^x$  dependence where  $x = 1.88 \pm 0.16$  where the uncertainty is taken to be twice the variance. This is consistent with a two-photon process underpinning the desorption rate and also consistent with the relationship found between the beam and pit profiles [3]. Note also in Figure 1-20 that the etch rate can be many orders of magnitude lower for UV etching than for laser ablation, allowing for much greater depth precision.

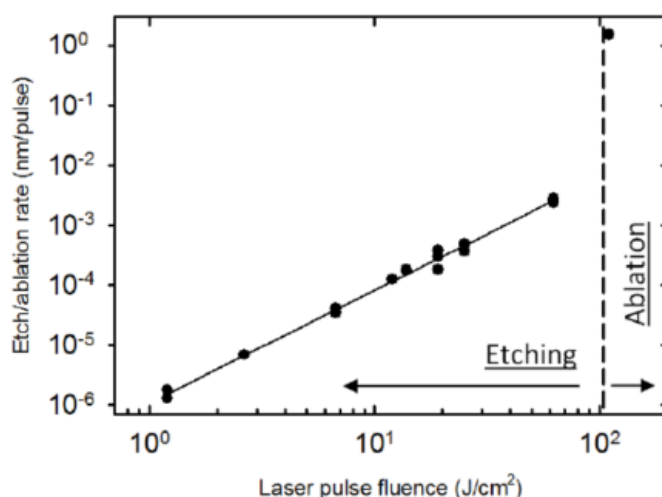


Figure 1-20 Etch rate as a function of laser fluence. The data point shown for the fluence above the ablation threshold corresponds to the average ablation rate per pulse for 60 pulses of fluence  $110 \text{ J} \cdot \text{cm}^{-2}$ . Pulse rate 7.5 kHz. Image credit: [3]

The authors report that the surface roughness increases from 1 nm to 3 nm upon etching to a depth of 300 nm as measured by the optical interferometric surface profiling. Finally the surface is shown to be oxygen-terminated and free from graphite through NEXAFS measurements [3].

This technique demonstrates the ability to create shallow high-resolution structuring and writing on oxygen-terminated surfaces however the exact process by which this takes place is not well understood as was whether this process would proceed in the same manner on hydrogen-terminated diamond. The phenomenon of UV etching of diamond is not well understood with respect to many aspects including the absorption mechanism, bond breakage and carbon atom ejection although work which has been done to understand this process will be discussed below.

Experiments on laser irradiation of diamond single-crystals in the absence of oxygen were decisive for clarifying one aspect of the UV etching mechanism. Experiments performed in vacuum and in helium atmospheres were carried out with the laser fluence at the spot up to only 15-20% below the traditional ablation threshold [4]. In both cases, no laser-induced etching occurred. The authors proposed that atmospheric oxygen plays a key role in the ejection of carbon from the surface of the diamond target and that given oxidation is the main reaction oxygen is involved in, that it is oxidation that is occurring on the surface of the diamond during this process.

The effect of the sample temperature on the UV etching rate was reported on by Kononenko et al. (2007). A diamond heating system was devised which consisted of a ceramic heater, an autotransformer as a voltage source, a thermocouple and a micro-voltmeter for measuring the sample temperature. This system was able to maintain the diamond from room temperature to 700 °C with an error of up to 10 °C without reacting chemically with the diamond even at the highest temperatures. The dependency of the ablation rate on the temperature is shown in Figure 1-21, where a clear trend is seen in the Arrhenius coordinates. This implies that the probability of detachment of a carbon atom from the surface obeys Boltzmann statistics and has a strong dependence on the temperature. The deviation between the temperature dependency and the Arrhenius fit observed at low temperatures was attributed to a fixed laser-induced heating of the sample [4].

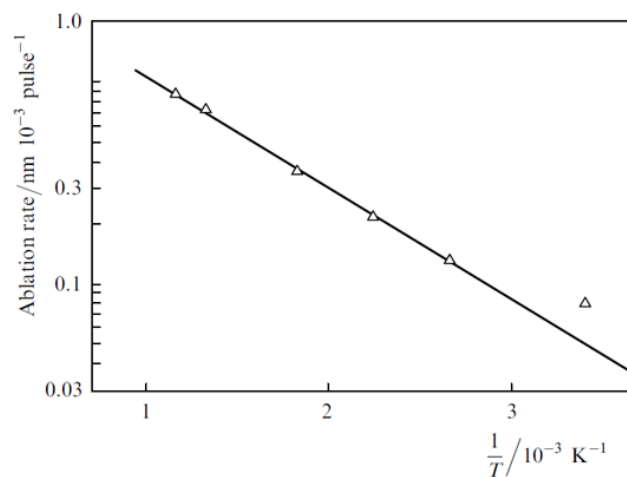


Figure 1-21 Dependence of the laser nanoablation rate on the temperature of the externally heated sample for a laser fluence of  $5.4 \text{ J cm}^{-2}$ . The linear fit in the Arrhenius coordinates suggests ejection of carbon atoms obeys Boltzmann statistics. Image credit: [4]

The activation energy for removal of surface carbon was calculated from Figure 1-21 and found to be 25 times lower than that of thermal oxidation [4]. Thus UV radiation appears to significantly lower the energy barrier of the oxidation reaction which is then proceeded by the removal of the formed oxide from the surface. It has been proposed that this oxidation mechanism is based on a photo-excitation of diamond which results in the appearance of free charge carriers in the conduction band upon absorption of photons [44]. This photo-excitation process will lead to the “suppression of atomic bonds in parts of the lattice” and due to the high efficiency of this process, it could be assumed that the number of “supressed bonds” is large enough to considerably increase the surface oxidation rate, thus providing the observed etching of the diamond surface in the absence of a graphitisation stage as in traditional laser ablation of diamond [4].

## 1.6 Project Direction

This project intended to develop techniques for rapid prototyping of functional micro-structures on diamond surfaces by using the UV laser etching technique to direct-write patterns with alternating H- and O-terminations. The investigations aimed to understand the parameters needed to create insulating and conducting tracks, develop techniques to interface and characterize the created structures, and ultimately design and characterize an example device – a surface FET.

At the outset of the project, this was to be the first systematic investigation on UV etching of hydrogen-terminated surfaces and it was unknown whether the surface-termination would influence the rate or probability of etching. Furthermore, it was not entirely clear how to form an ohmic contact to a sub-surface two-dimensional hole gas nor was it clear how to efficiently hydrogen-terminate the surface of a diamond film in the diamond CVD reactor that was available for the project. The later questions were the first to be answered and will be discussed in the following two chapters. The etching of hydrogen-terminated diamond will be discussed in Chapter 4.

---



## 2 Sample Processing Techniques

### 2.1 The UV Laser Etching System

The UV laser etching system is custom-built around a pulsed IR (1030 nm) pump beam which is frequency doubled twice, resulting in a pulsed UV beam at 257.5 nm wavelength. The pump beam is first frequency doubled by a temperature-tuned lithium triborate (LBO) crystal, then again using an angle-tuned beta-barium borate (BBO) crystal. The UV laser etching system is depicted in Figure 2-1. The IR pump beam is first rotated 90 degrees from horizontal to vertical by a half-wave plate. This serves three purposes: 1) the BBO can now be conveniently tuned by rotation in the horizontal plane, 2) the Pellin-Broca prism can rotate and separate the beams safely in the horizontal plane as opposed to the vertical, and 3) the incident power can be conveniently controlled by rotation of the wave plate. By controlling the pulse energy with the half-wave plate, we can control the etch rate and reduce the likelihood of ablation by reducing the energy per pulse without reducing the pulse repetition rate. The ability to conveniently tune the laser power was especially useful given the low ablation threshold of the diamond films available during this project.

The IR beam is then focused at normal incidence into the LBO crystal, which is maintained at 150°C by a temperature-controlled mount to achieve the optimal phase matching condition. The diverging beam of green (515 nm) laser light produced by the LBO is collimated and focused by a cylindrical anti-green reflection coated lens into the BBO crystal. The BBO must be angle tuned to achieve the correct phase matching conditions. The beam is then collimated again by a fused silica cylindrical lens and a Pellin-Broca prism is placed in the beam path to separate the various harmonics and direct the beam to the translation stage. A shutter is positioned between fused silica lens and the Pellin-Broca prism to stop the beam reaching the translation stage when necessary.

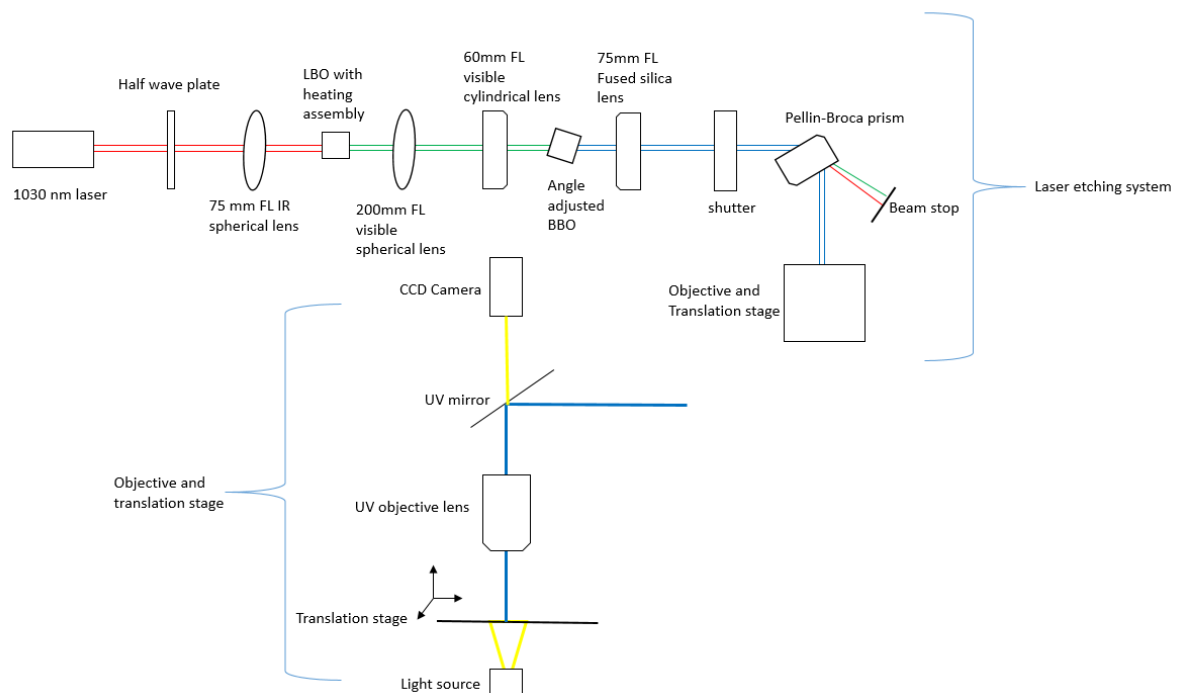


Figure 2-1 UV laser etching system and detailed schematic of objective/translation stage.

It should be noted that the focal length of the collimating and focusing lenses currently in use are not identical which results in an elliptical beam. This is due to a limited availability of lenses, as a fused

silica lens is required to focus the UV output, but no fused silica cylindrical lenses were available with focal length matching the lens required for optimised second-harmonic generation in the BBO. The unfortunate and currently unavoidable consequence of the elliptical beam is that any diamond etches performed by this system will be asymmetrical.

A UV mirror is used to direct the beam downward to a UV objective lens, which focuses the beam on the translation stage. The objective lens can be easily interchanged between a 5x and a 20x objective depending on the requirements for a particular etch. To view the sample on the translation stage, a bare CCD is placed above the objective. Light redirected from the sample in the focal plane of the objective is approximately collimated as it passes through the lens. The CCD is positioned so that the focal plane of the camera is the same as that of the UV beam, therefore bringing the sample into the cameras focus with the translation stage brings the sample into the beams focus. Fine adjustments to the focus are achieved by moving the translation stage through the focal-plane at set intervals by a simple programming script and observing when the beam is capable of cutting a glass slide on the translation stage. Further fine adjustments can then be made in the same manner by etching shallow pits into a diamond surface and observing the depth of the etched pits using optical interferometry (see Appendix 7.1 for details of optical interferometry). The deepest pit will indicate the position of the focal plane and will also determine the etch rate for a given pulse repetition rate, pulse energy and diamond sample.

Typical etch rates within the group for this laser system would be in the 10's of nm per minute depending on the pulse rate and energy. For the purposes of this work however, mono-layer deep etches would suffice to switch the surface termination from hydrogen to oxygen in order to define conductive structures in the surface termination.

## 2.2 Hydrogenation of diamond films

Diamond films grown by hydrogen-plasma assisted chemical-vapour deposition processes will have their surfaces terminated in hydrogen [47]. Unlike graphite, the diamond surface has to be truncated by hydrogen to maintain the  $sp^3$  bond integrity and in fact it is the hydrogen termination of the surface which facilitates the preferential deposition of diamond over graphite during growth [48]. As an interesting aside: the surface of hydrogenated diamond roughly resembles a continuous  $sp^3$ -bonded alkane molecule as depicted in Figure 2-2.

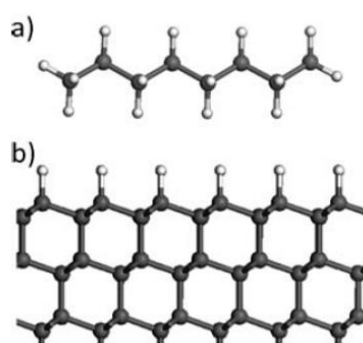


Figure 2-2 a) Ball-and-stick drawing of octane and b) H-terminated diamond lattice. Image credit: [49]

Such diamonds will display p-type surface conduction as discussed in Chapter 1.3. It is possible however, to hydrogenate (or re-hydrogenate) the diamond surface post-growth, by exposure to

hydrogen plasma. Several samples were hydrogenated in a microwave-excited plasma under various conditions. A survey of the literature, particularly in regards to diamond electronics, reveals sample temperatures while exposed to the plasma in the range of 500 to 800 °C, pressures between 10 and 50 Torr for between 10 and 30 minutes (see for example [26], [50], [51], [52]). Despite all the information found on various hydrogenation conditions, very little information was located on the 'optimal' conditions or why specific conditions were chosen by various authors. Determining a suitable hydrogenation procedure was therefore very much a trial-and-error process; the varied parameters explored are summarised in Table 2-1 at the end of this section. The first sample to be hydrogen treated under microwave plasma was a 4x4x0.2 mm<sup>3</sup> polycrystalline diamond. The base of the diamond was held at 500 °C while the top surface of the sample, as measured by a two-wavelength pyrometer, was heated to 600 °C by the plasma. The plasma was run at 600 W for 30 minutes at a pressure of 20 Torr. This was followed by a 4x4x0.2 mm<sup>3</sup> single-crystal diamond treated under the same conditions except that the diamond was hydrogenated on both sides by turning the diamond over and running the plasma over the other side after the treating the first side. Both sides were hydrogenated as a precaution in case any confusion were to arise as to which side had been hydrogenated. Next a 4x4x0.5 mm<sup>3</sup> single crystal was hydrogenated at 700 °C and 1 kW with specific attention paid to running the hydrogen gas through the vacuum chamber until the diamond had cooled substantially as thermal desorption of chemisorbed hydrogen will commence at 700 °C [27]. These conditions yielded a surface with low resistance, although the surface of this diamond was very rough post-hydrogenation with seemingly random pits dotted around the surface. This was attributed to hydrogen-plasma etching of the diamond surface [53]. A surface region typical of the roughness and pitting observed is shown in Figure 2-3 where the root-mean-squared (RMS) roughness is 6.04 nm. The consequences of this hydrogen-plasma induced surface roughness will be discussed further in Chapter 4.

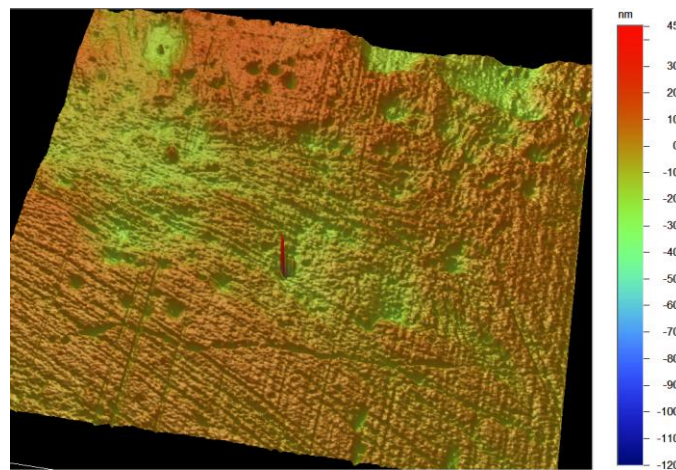


Figure 2-3 Optical interferometry (PSI) image of the surface roughness on the front face of the 0.5 mm thick single-crystal diamond after the initial hydrogen-plasma treatment. This image shows a typical surface between the Au contacts.

For the final set of experiments the 4x4x0.5 mm<sup>3</sup> single-crystal was washed in Aqua regia to remove the Au deposited onto the surface, as discussed in the next section, and the previous hydrogenation conditions were replicated for the back-side of the diamond, except that the sample in the plasma was brought to 700 °C and then reduced almost immediately in order to minimise the potential hydrogen-plasma induced etching observed on the front-side of this sample. This procedure was also applied to a 'new' 0.2 mm thick single-crystal diamond at the same time. This diamond had previously been used

for ablation threshold tests however the back side of this film would still be suitable for the needs of this project.

The back surface of the 0.5 mm thick sample did not appear to be pitted post-plasma exposure but did appear to have an RMS roughness of 4.81 nm as can be seen in Figure 2-4. However it is unknown if this surface roughness was present pre-plasma exposure as the surface profiling was inconclusive due to difficulties with the instrumentation.

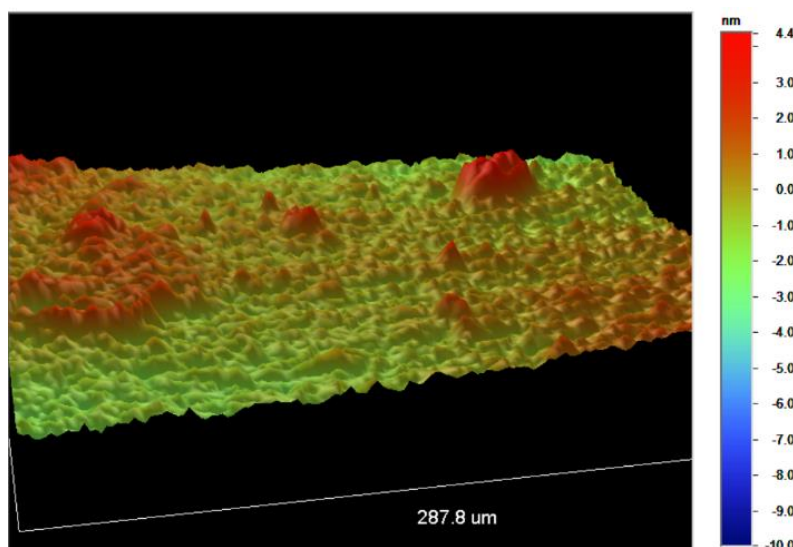


Figure 2-4 Optical interferometry (PSI) image of the surface roughness on the back face of the 0.5 mm thick single-crystal diamond after the second hydrogen-plasma treatment. The back face does not appear to be as rough and does not show the same distinctive pitting as the front face.

However the ‘new’ 0.2 mm deep diamond film was successfully imaged before and after hydrogenation and no statistically significant variation in the surface roughness was observed with an RMS roughness of 0.71 nm. Furthermore the surface displayed low resistance, as will be discussed in the next chapter. Therefore this final hydrogenation procedure appears to be the most successful, producing a low resistance surface with minimal alteration to the surface roughness or random etching.

Table 2-1 Hydrogenation conditions used for the various diamond samples. The ‘plasma temperature’ refers to the temperature the top surface of the diamond was brought to by the plasma. Although the last two entries were only brought to 700 °C for a moment, the total exposure time to the hydrogen-plasma was 5 minutes.

Diamond	Power (W)	‘Plasma Temperature’ (°C)	Time (mins)
0.2 mm polycrystalline	600	600	30
0.2 mm single-crystal	600	600	30
0.5 mm single-crystal	1000	700	30
0.5 mm single-crystal (back)	1000	700	5
‘new’ 0.2 mm single-crystal	1000	700	5

### 2.3 Au Contact Evaporation

As discussed in Chapter 1, the hydrogen-terminated surface and adsorbate transfer-doping-layer creates a two-dimensional hole gas below the diamond surface which may be 5 nm deep. It is therefore not entirely clear how to form an ohmic contact to the sub-surface conducting layer and in fact this is a common engineering problem in the semiconductor industry. However, an examination of the literature of diamond semiconductor devices reveals that Au will form an ohmic contact and is the most common choice for drain, source and gate contacts in diamond surface devices, although Al is often also used as the gate contact. A selection of devices from the literature are listed in Table 2-2 with information on the contact material and specifics of the fabricated device.

Table 2-2 Source, Drain, & Gate contact materials used for diamond electronic devices

Reference	Drain/Source	Gate	Device Type
[39]	Au	Au (50nm)	53 GHz extrinsic, 90 GHz intrinsic, 50 nm gate length
[21]	Au	Al	Circular planar, gate length 8.5 $\mu\text{m}$ and 500 $\mu\text{m}$ effective gate width
[21]	Au	Al	Rectangular planar, gate length of 3.0 $\mu\text{m}$ and 100 $\mu\text{m}$ gate width.
[54]	Au	CaF <sub>2</sub> /Cu/Au	Surface-channel-MISFET
[15]	Au	Au (0.2 $\mu\text{m}$ )	Surface-channel-MESFET, self-aligned gate technology
[5]	Au	Al	0.1 $\mu\text{m}$ gate, 45GHz, homoepitaxial & polycrystalline
[41]	Au	Al	Polycrystalline, average grain size of 200 $\mu\text{m}^2$ , $L_g=0.3 \mu\text{m}$ and $W_g=25 \mu\text{m}$
[55]	Au	Al	Polycrystalline, optically activated gate $L_g = 1 \text{ mm}$ , $W_g = 0.5 \text{ mm}$
[56]	Au	CaF <sub>2</sub> /Al	Surface-channel-MISFET
[56]	Au	Cu	Device dimensions: $D_{sg} = 0.2\mu\text{m}$ , $D_{gd} = 0.2\mu\text{m}$ , $D_g = 26\mu\text{m}$
[42]	Au	Au	Single electron, AFM oxidised
[57]	Ti/Al/Ti/Au	AlN/Ni/Au	SiO <sub>2</sub> , Al <sub>2</sub> O <sub>3</sub> , and AlN have mainly been used as the insulators for the surface channel FETs.
[54]	Au	CaF <sub>2</sub> /Cu/Au	$f_{cutoff} = 11 \text{ GHz}$

To fabricate the devices in Table 2-2, standard lithography and etch-back/lift-off techniques are used. These devices, as well as those described in Chapter 1.4, are all planar devices and are fabricated by depositing the ohmic contacts directly onto the hydrogen-terminated surface. The general procedure is depicted in Figure 2-5 and involves several photo-resist depositions as well as oxygen-plasma and wet chemical etching to define the electrode structure.

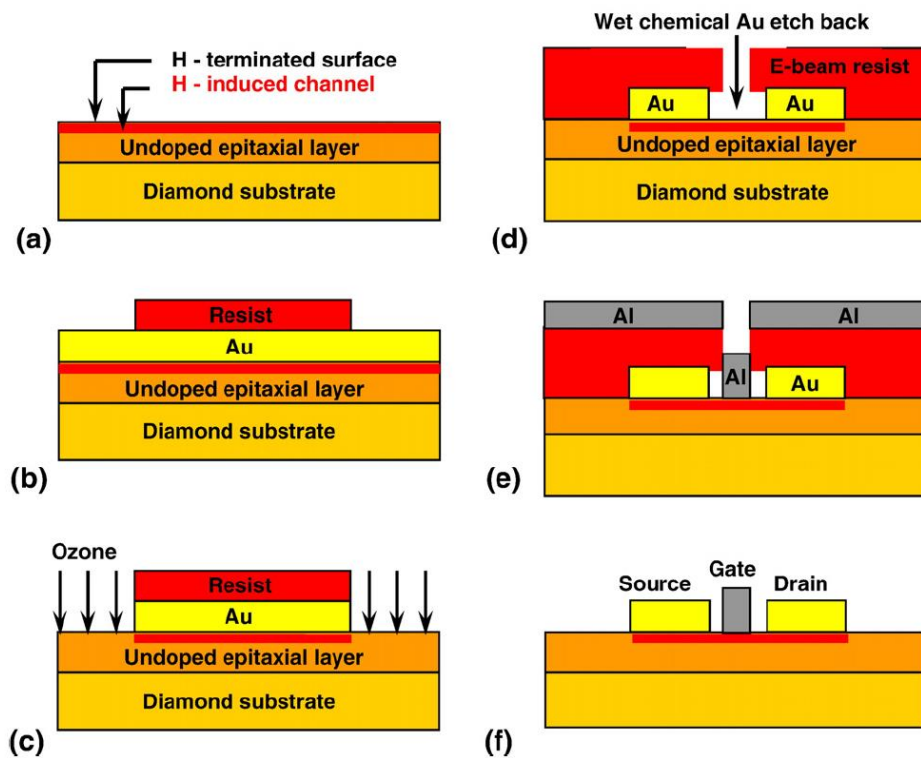


Figure 2-5 H-terminated diamond FET fabrication process. (a) Epitaxial growth of diamond and hydrogen termination of the surface. (b) Evaporation of Au and formation of MESA structures using optical lithography. (c) Device isolation using oxygen plasma. (d) E-beam lithography for T-gate and wet chemical Au etch back. (e) Self-aligned Al evaporation. (f) Gate patterning and lift-off. Image credit: [58]

This procedure for depositing ohmic contacts onto the hydrogenated surface is less useful for the aims of this project where the structure of the FET, i.e. the conducting surface, is to be defined using the UV etching process. To this end, Au was evaporated under vacuum onto the hydrogenated surface through a Ni mask with the intent to define the conduction path of the devices around the Au deposits. The masks were laser cut by the Macquarie University ANFF OptoFab Node with 0.250 mm square holes and the diamond sample was held behind the mask in an Al-block custom built by Macquarie Engineering and Technical Services. A 0.250 mm square was chosen for the Au contacts as it allowed for a 'high density' of Au contacts to be deposited whilst making them large enough to be easily accessible for electrical measurements on the probe station, which is detailed in Chapter 3. A pair of 10  $\mu\text{m}$  wide slits was cut in one corner of the mask to provide a region of the diamond for calibration etches to be performed as well as providing a reference point. The designs for the sample mount and mask are shown in Figure 2-6. The mask would sit in a shallow groove in the Al block while the diamond would sit on the mask inside a hole cut through the block. A magnet on the back of the Al block would hold the nickel mask in place while the entire mount was suspended upside down in a vacuum chamber. Au was evaporated from a thermal source 30 cm below the sample, passing through the contact mask to deposit on the sample surface. The background pressure during deposition was  $2 \times 10^{-6}$  Torr. A quartz crystal thickness monitor was used to estimate the thickness of the Au layer as it was being deposited, however more accurate measurements were taken afterwards using an optical interferometer.

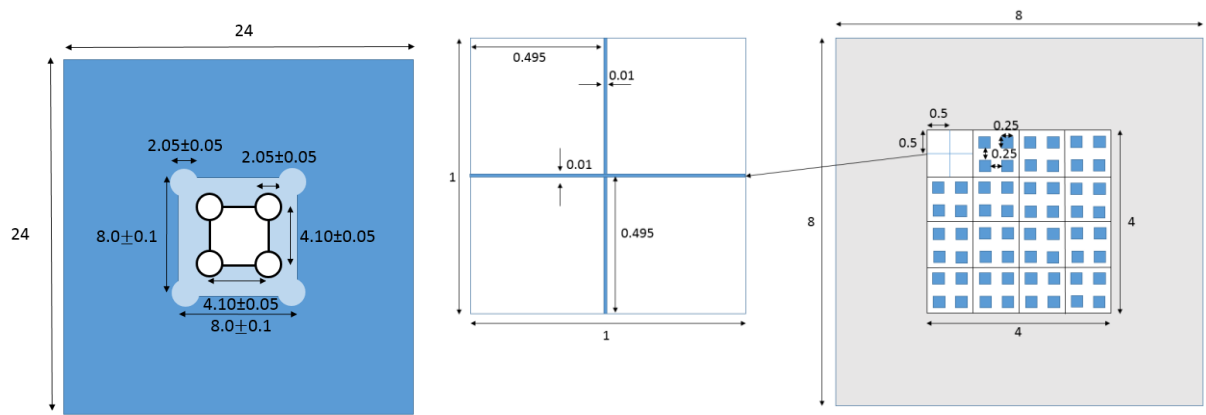


Figure 2-6 LEFT: Schematic of sample mount cut by Macquarie Engineering and Technical Services. The middle groove where the mask sits is 0.8 mm deep and the inner region is cut right through. RIGHT: Schematic of nickel evaporation mask, laser-cut by Macquarie University ANFF OptoFab Node. All measurements are in mm.

This process resulted in reasonably well resolved square plates of Au on the surface of the diamond. The first attempt with a 0.2 mm thick polycrystalline film resulted in Au deposits with a typical height of 60 nm and a width of 0.26 mm. The width of the deposited Au was close to that specified for the mask, however the thickness of the Au was a fraction of the estimate given by the quartz crystal thickness monitor (~100 nm). Measurements of later depositions on single-crystal diamond were more consistent and although this was the only polycrystalline diamond examined this is not taken as an explanation for the inconsistency here. It is clear that either the diamond was not sitting flat against the mask or that one or both the mask and diamond moved during the deposition process. This is evident from Figure 2-7 where two steps are clearly visible along one edge of the Au contact and another is present along the opposite edge. This step-like feature may account for the discrepancy between the thickness estimate from the quartz crystal monitor and the optical interferometry measurement. Further evidence of relative motion between the mask and diamond can be seen later in Figure 3-1 where it is clear that the pattern of Au contacts has been shifted towards one edge of the diamond relative to where they should have been deposited.

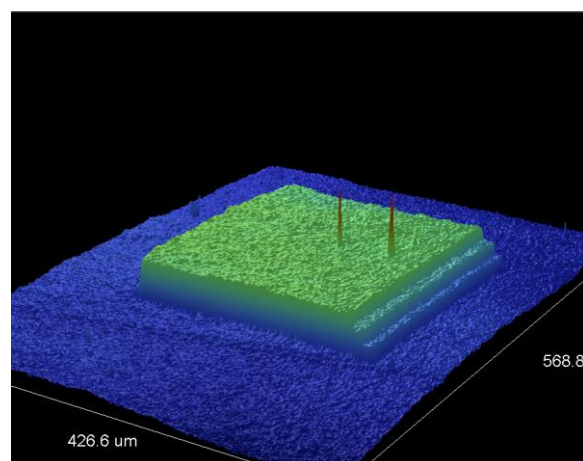


Figure 2-7 Optical surface profile image of a Au contact deposited onto polycrystalline diamond. The stepped effect along the edge is likely due to movement between the diamond and mask during the Au evaporation process. The vertical scale is exaggerated for clarity.



This step-like feature was not observed in subsequent depositions onto new samples and is most likely attributed to greater care in positioning the diamond into the sample mount. Note the well-defined edges of the Au deposited onto the 0.5mm thick single-crystal diamond in Figure 2-8. Also interesting to note is that the surface roughness of the diamond is translated onto the surface of the deposited Au.

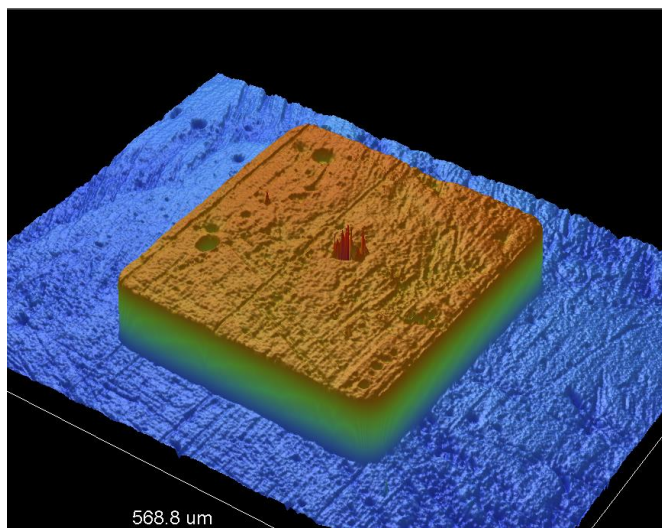


Figure 2-8 Optical surface profile image of Au deposited onto 0.5 mm thick single-crystal diamond. The Au is approximately 260  $\mu\text{m}$  wide and 0.1  $\mu\text{m}$  thick. The vertical scale is exaggerated for clarity.

The Au plates, however, are quite soft and prone to damage. Measurements of the surface resistance were performed using a pair of Au-plated tungsten needles, which frequently scratched the surface of the Au-plates, and were more than capable of completely removing Au from the diamond surface. Furthermore, exposure to the UV laser spot in the etching system was also able to remove Au from the surface under modest power conditions and furthermore was capable of inducing ablation of the diamond surface below despite the beam parameters being otherwise below the threshold for diamond ablation. Due to the ease with which the Au contacts were removed, they would eventually need to be etched off the surface with acid and re-deposited.

A second mask was also cut by ANFF OptoFab to allow for the deposition of a lower density of Au contacts. This mask would be used to form the contacts for a field-effect transistor with the lower density of Au contacts providing increased room for larger and more complicated etched structures.



### 3 Electrical Characterisation of the Diamond Surface

Characterisation of the surface electronics was carried out on a translation stage under an optical microscope. Metallic needles (probes) connected to a programmable electrometer (Keithley 617 or Fluke 45) are positioned above the translation stage and lowered onto the surface of the diamond. The first attempt to measure the surface resistance of a hydrogenated diamond using tungsten probes was unsuccessful; the resistance between the tungsten probes and the hydrogenated surface exceeded the standard range ( $>200\text{ G}\Omega$ ) of any accessible measurement device. To remedy this problem, the tungsten probes were electro-chemically etched to clean and sharpen them, and coated in Au using an evaporative technique similar to that described in Chapter 2.3. This allowed for better electrical contact with the surface and resistance measurements in range 10-100's  $\text{G}\Omega$ . This, however, is still far too high for fabrication of semiconductor devices, and this provided the rationale for depositing the Au contacts onto the diamond surface as described in Chapter 2.3. With the Au contacts deposited on the surface of the diamond, the resistance between each contact was easily measurable using the Au-coated tungsten probe tips as shown below in Figure 3-1. The presence of the Au contacts makes measuring the resistivity problematic, however, as the spacing between contacts is consistent, measuring the resistance between adjacent contacts allows a useful comparison between devices/samples.

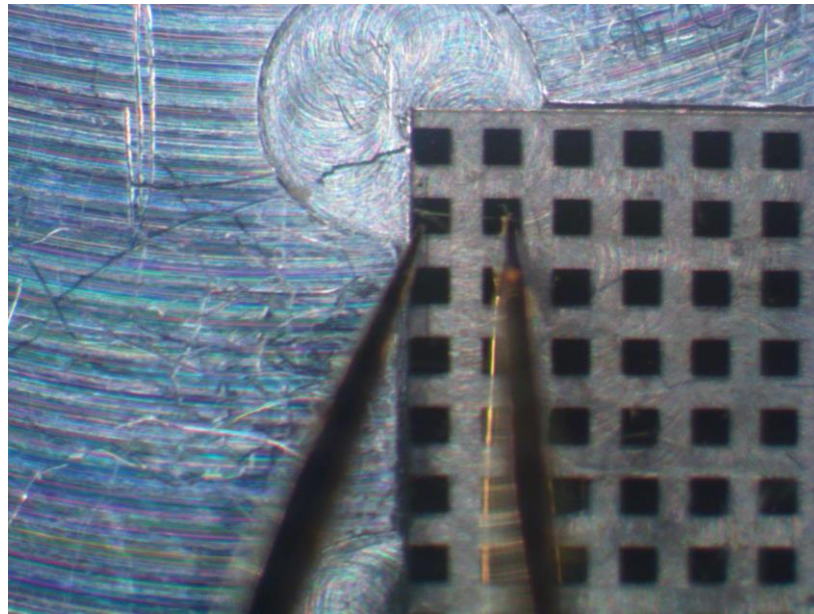


Figure 3-1 Optical micrograph of surface connection of Au-coated probes onto Au contacts deposited on a polycrystalline diamond film. Each Au contact, which appears as a black square due to the optics of the microscope, is 0.26 mm in side length. The diamond is sitting in a groove on a custom designed aluminium block, which prevents the diamond from sliding when the Au-coated tungsten probes apply pressure. The probes would remain in place and the diamond was translated beneath the probes to measure the resistance across each pair of horizontally adjacent Au contacts.

The consistency of the hydrogenated surface was checked by mapping the surface resistance via translation of the stage under the probes and recording the resistance between each horizontal pair of adjacent Au contacts. The measurements were performed this way to avoid any additional issues with plotting discrete data points as a continuous surface. The surface resistance of the 0.2 mm hydrogenated single-crystal diamond is plotted in Figure 3-2; note that the axes in the figure below

refer to the pairs of Au contacts and not to coordinates on the diamond i.e. point (1,1) is the first pair of horizontal contacts in the first row etc.

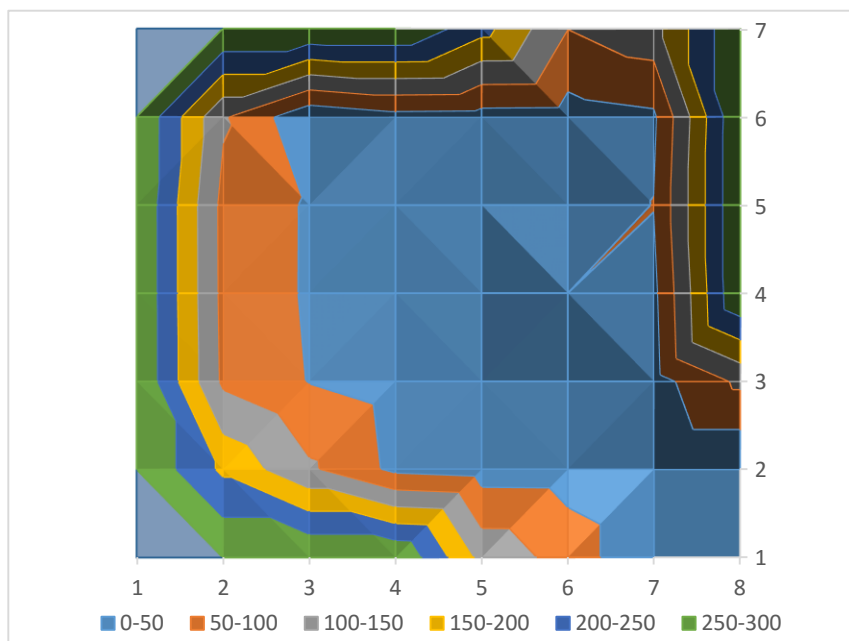


Figure 3-2 Surface resistance of a single-crystal 0.2 mm thick hydrogen-terminated diamond film plotted in a 2-dimensional contour plot. The axes in the figure refer to the pairs of Au contacts and not to coordinates on the diamond. The lower right corner of the plot contains no data points due to the Au cross-hair in that corner. Resistance is measured in k $\Omega$ , although the data is truncated at the edges due to the high resistance ( $\geq 1\text{M}\Omega$ ) between the contacts along the edge of the diamond.

In the case of the 0.2 mm single-crystal diamond, we find that the surface resistance between adjacent Au contacts, separated by 0.24 mm, is less than 50 k $\Omega$  across the middle of the diamond film. The resistance rises quickly towards the edges of the diamond to the 10's-100's of M $\Omega$  and higher. The reasons for this are not entirely clear but may be due to insufficient hydrogen-termination towards the edges due to the hydrogenation conditions employed (see Table 2-1) or imperfections in the crystal. Furthermore, subsequent measurements yielded consistently higher readings for the resistance between the Au contacts. It was postulated that this was due to an uncharacteristically low humidity in the lab, and from this point onwards the humidity of the lab was noted during any electrical characterisation of the samples.

Due to the softness of Au, the contacts were very malleable and susceptible to scratches during electrical measurements with the Au-plated probes. This made taking resistance measurements challenging, particularly as high contact resistance between the probe and Au surface meant having to 'jiggle' the probe back-and-forth on the Au surface before adequate contact was made. With practice, the damage done to the Au contacts could be minimised but not eliminated entirely. A new pair of Au-coated tungsten tips were prepared which were very heavily coated and appeared to cause less damage to the Au contacts compared to the previous tips, although if lowered far enough would easily push the Au right off the surface. Given the Au is essentially sitting on a hydrocarbon surface an apt comparison could be made between the diamond surface and baking paper; the deposited Au will slide off the diamond surface given minimal force.

An example of the damage done to one of the Au contacts is shown in Figure 3-3. This image, produced by optical interferometry, shows that the probe tip has gouged a channel right through the Au contact to the diamond surface below. Eventually, with all the Au contacts damaged it was no longer possible to determine the resistance of the 0.2 mm single-crystal diamond and the diamond would need to be re-hydrogenated with new Au contacts deposited before any future investigation of this sample.

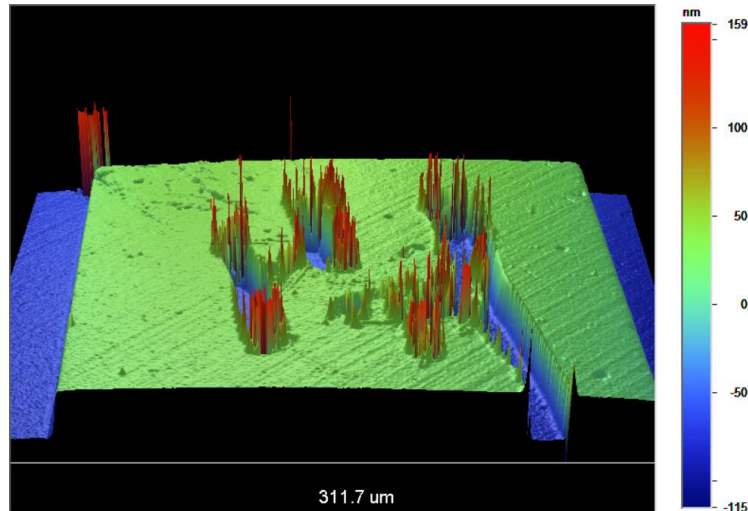


Figure 3-3 Optical surface profile image of a Au contact on 0.2 mm thick single-crystal diamond which had been damaged during electrical characterisation of the surface. The Au-plated tungsten probes used for electrical measurements are capable of scratching through the Au right to the diamond surface below.

The revised hydrogenation conditions used for the 0.5 mm single-crystal diamond showed much greater promise for the fabrication of diamond semiconductor devices. Significantly lower resistance was noted on this sample, as well as being more consistent across the surface. Figure 3-4 plots the surface resistance and shows the surface has a resistance of 10 k $\Omega$  or less at a humidity of 53%. This figure increased as the humidity decreased; resistance measurements in the 10's and 100's of k $\Omega$  were noted at relative humidity of 40% and 30% respectively. This sample was subsequently stored under a bell jar next to beaker of water i.e. in a virtually 100% humidity environment. After three days in this environment the resistance between a random pair of Au contacts decreased from an initial measurement of 26 k $\Omega$  to 10.5 k $\Omega$  over the course of 2 hours. This measurement was performed under a relative humidity in the laboratory of 50% and after two hours, the surface resistance between random pairs of Au contacts was consistent with previous measurements.

Proposed explanations for the increased resistance at higher relative humidity include: the p-type diamond surface requiring an optimal surface "wetness" or operational humidity, or the wetting layer needs to be continually exposed to atmospheric carbon dioxide to reduce the pH of the wetting layer and improve conduction. At this stage, both hypotheses are ad hoc conjectures. Photo-induced conduction due to the halogen-lamp of the microscope was quickly ruled out as a possible mechanism as it does not explain the increased resistance and the consistent decline in resistance from 26 k $\Omega$  to 10 k $\Omega$  was observed with and without the halogen-lamp on. For the measurements shown in Figure 3-4, under stable humidity conditions, the photo-induced conduction was seen to only contribute a reduction in resistance of several k $\Omega$ . This effect was largely ignored and measurements were taken without turning off the halogen-lamp until significant modification of the conduction channel was achieved through UV etching and resistances in the G $\Omega$  range were measured, at which point the lamp was switched off during measurements as the change in conduction had a much more pronounced

effect. As an interesting aside: by shining hand-held laser pointers at the surface it was found that the photo-conduction appeared much more pronounced for green light than for red. While this effect was not investigated any further during this project, optically activated diamond-based field-effect transistors have been reported in the literature [55]. This phenomenon remains an active area of research [59] and has been shown to be exploitable to create deep UV photo-detectors [60] however investigation of this mechanism lay beyond the scope of this project.

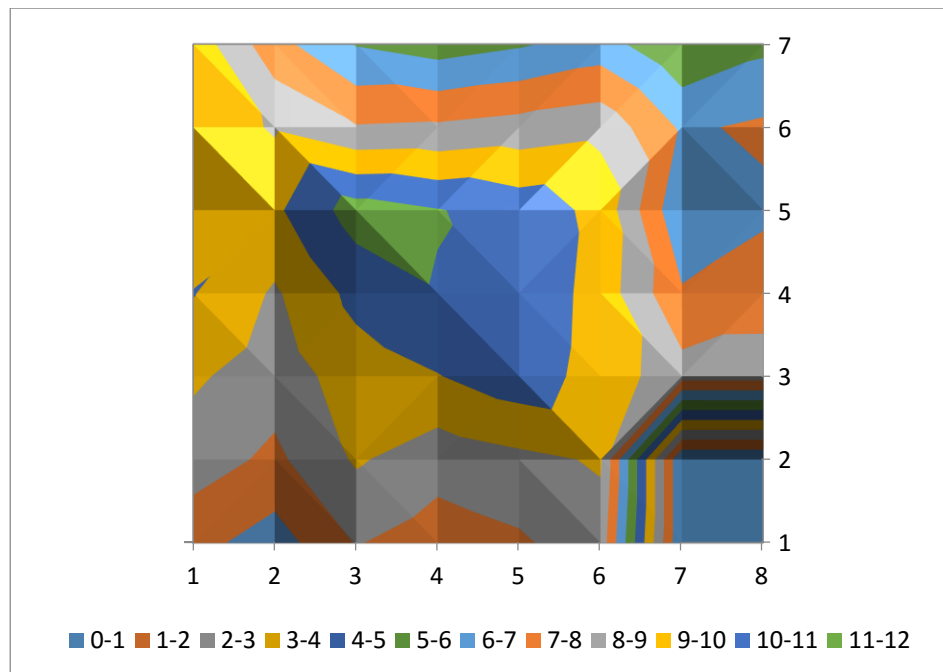


Figure 3-4 Surface resistance of the single-crystal 0.5 mm thick hydrogen-terminated diamond film after the first hydrogenation treatment plotted in a 2-dimensional contour plot. Resistance is measured in  $k\Omega$ , the relative humidity was 53%. The axes in the figure refer to the pairs of Au contacts and not to coordinates on the diamond. The lower right corner of the plot contains no data points due to the Au cross-hair in that corner.

Extensive data-logging of the 0.5 mm single-crystal diamond was planned to monitor the resistance over time as the surface wetness came into equilibrium with the ambient humidity after being stored in the 'wet' environment, however the Au contacts were rendered inaccessible over the course of other investigations before the data logging could be carried out. Therefore this investigation was carried out on a new 0.2 mm thick diamond film H-terminated under the final hydrogenation protocol discussed earlier and Au plated using the 'high-density' mask. Unfortunately this behaviour was not able to be replicated on the freshly hydrogenated sample. Immediately after deposition of the Au contacts the resistance between adjacent contacts on the new diamond film was 10  $k\Omega$ , however the resistance immediately after removal from the 'wet' environment was unchanged. In fact the resistance increased over 30 seconds to 25  $k\Omega$  although this may be related to the low humidity in the lab at that time (30% relative humidity). It may be possible that this effect is due to degradation of the surface-termination due to exposure to the atmosphere, of which the 0.5 mm diamond film certainly had more exposure too. It has been reported by Geisler & Hugel (2010) that aging of the surface-termination by physisorption of atmospheric adsorbates and conversion of surface chemical groups affects the wettability, morphology and electrical properties of the terminated surface [61]. The authors report that these two effects may take place on the time scale of days and months respectively.

## 4 Results & Discussion

This section will largely discuss the outcome of the etching experiments. These experiments follow a clear path of progression from verification of etching through to etching of field-effect transistor structures with each new stage contingent on the previous. As discussed previously, all systematic investigations of 2-photon UV etching had, to date, been performed on O-terminated diamond and had been observed to leave the etched surface O-terminated. It was not what effect a hydrogen-terminated surface would have on the etch rate or ablation threshold. Once the UV etch rate of H-terminated diamond could be established, the next step was to etch a path around a single Au contact, replacing the H-termination with O-termination, and electrically isolate that contact from the surrounding surface. If this was demonstrated, the next step in the progression would be to attempt to partially remove the H-termination and thus demonstrate novel control over the surface doping. In parallel to the last point, a demonstration of adjacent and isolated conducting paths would be attempted. Lastly, building on each previous stage, a simple FET structure would be etched. The following sections will address each of these stages in turn.

Several diamond samples were prepared and analysed over the course of this project including a 0.2 mm thick polycrystalline film, a 0.2 mm thick single-crystal film, a 0.5 mm thick single-crystal film and a 0.2 mm thick single-crystal sample that had been used previously for ablation tests. Initial work on the polycrystalline film was useful for understanding and refining the hydrogenation, Au contact evaporation, DC measurement and etching techniques. However this sample was ultimately set aside due to significantly higher surface resistance and, in particular, a lower ablation threshold which made etching structures extremely difficult.

### 4.1 Etch Calibrations on H-terminated Diamond

Etching of oxygen-terminated diamond had been carried out by others within the research group previously using the laser system described in Chapter 2.1 where incident powers of up to 300 mW had been used to achieve etch rates around 30 nm/min for a stationary exposure. Initial attempts at etching hydrogen-terminated single-crystal diamond during this project were hampered by an apparently low ablation threshold. Evidence of ablation was apparent during focus calibrations where a series of lines were etched to determine the etch rate and the position of the focal plane (the deepest etch would occur when the surface is in the focal plane of the objective lens). The irregular lines visible in Figure 4-1 are attributed to ablation of the diamond surface. The script controlling the translation stage called for evenly spaced straight lines of equal length, and it is unclear why the calibration etch appears as it does. What is clear however, is a maximum etch depth of several micrometres was achieved in one minute. This is far deeper than any previous UV etch achieved on this system and is more akin to ablation. UV etching of hydrogen-terminated diamond had not been systematically investigated previously; it is unknown if the surface-termination plays a role in the ablation threshold of diamond and it was not methodically investigated here, beyond finding the parameters for UV etching without ablation, due to the time constraints imposed.

---

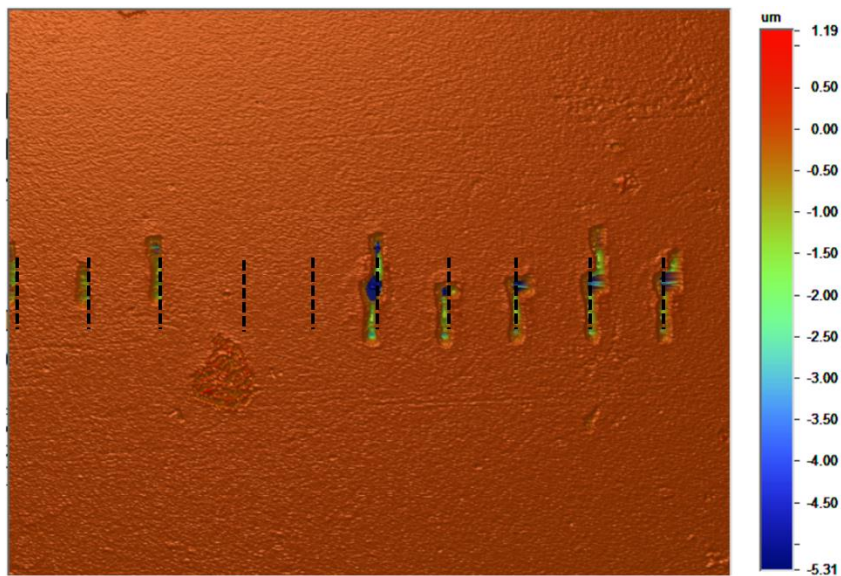


Figure 4-1 Evidence of ablation during laser focus and etch depth calibrations on 0.2 mm thick single crystal diamond at an incident power of  $320 \pm 20$  mW. The intended etch was to be a series of vertical lines with systematic variation in the etch depth due to translation of the stage through the focal plane. The approximate position of the intended etches are marked with dotted lines.

To reduce the likelihood of ablation occurring, the incident laser power was reduced to  $(125 \pm 5)$  mW by reducing the electrical current to the laser from 5000 mA to 3000 mA. As the pulse rate and applied current are linked in pulsed-laser operation, this had the additional effect of reducing the pulse repetition rate from 25 kHz to 11 kHz. In later etches, the incident power was tuned using the IR half-wave plate as described in Chapter 2.1 so that the pulse rate would remain consistent whilst still allowing for control over the incident power and thus etch rate. The result was a maximum etch rate of 30 nm/min at the position of the objective focal plane, illustrated in Figure 4-2, which was higher than expected for this laser system, given the incident laser power, but did not show obvious signs of ablation.

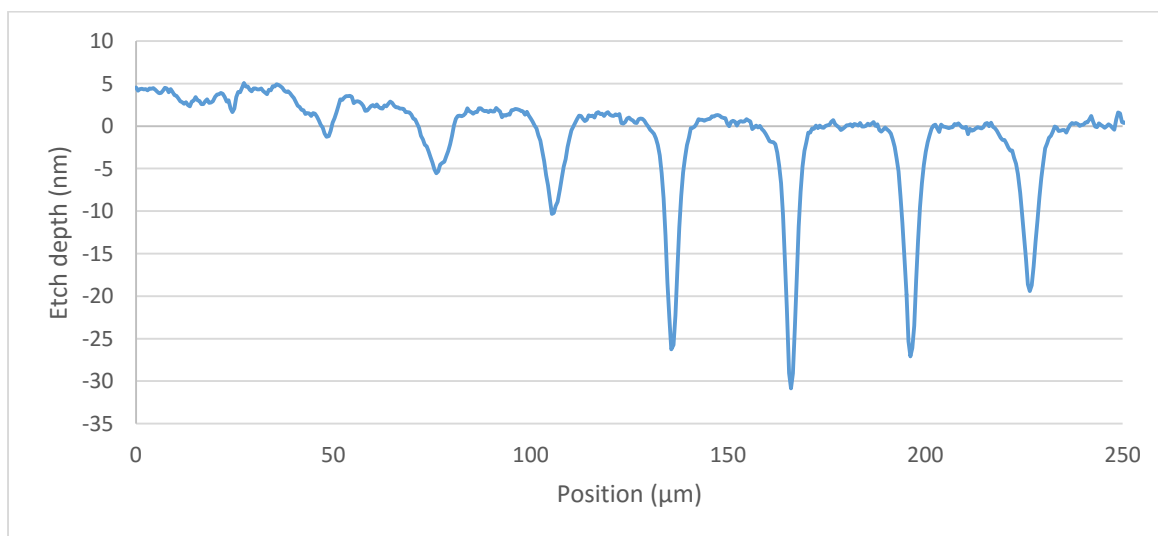


Figure 4-2 Etch depth calibration on 0.2 mm thick single-crystal diamond at an incident power of  $(125 \pm 5)$  mW. Each dip is a single pit, etched for 1 min, taken at set intervals around the focal plane in order to locate the precise focus. The deepest pit will correspond with the position of the focal plane



of the objective. The maximum etch depth of 30 nm/min is a significantly faster etch rate than expected from past experience in the group with this laser system.

Using the observed etch rate of 30 nm/min, the feed-rate (movement speed) of the translation stage was configured for an exposure time which would yield an etch depth of 1 nm. This etch depth would be more than sufficient to etch the surface layer of carbon atoms and switch the surface-termination from hydrogen to oxygen. Three etches were attempted, each tracing a square around a separate Au contact. In each case a distinct line of ablation was noted around each Au contact. The ablation lines were clearly visible under an optical microscope, as well as on the CCD camera of the laser etching system, and were also observed with a back-scattered scanning-electron microscope (SEM) as seen in Figure 4-3. At this stage, due to the apparently low ablation threshold and the excessive damage done to the Au contacts during electrical characterisation, which made any further measurements of electrical resistance impossible, this sample was abandoned in favour of a 0.5 mm thick single-crystal diamond.

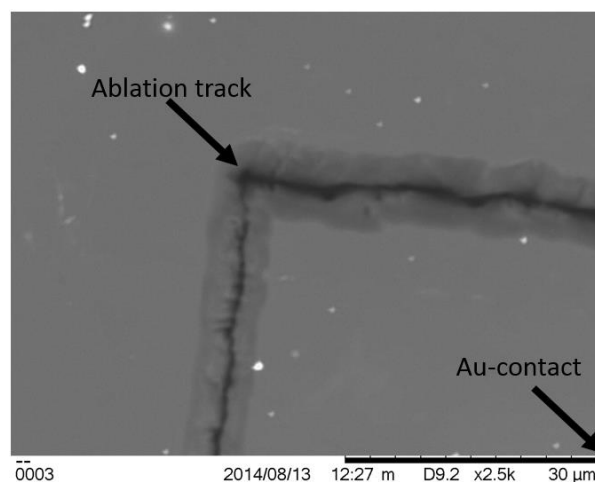


Figure 4-3 Clear and characteristic signs of ablation are visible around the Au contacts on the 0.2 mm thick single-crystal diamond film despite being calibrated for a 1 nm deep etch. The Au contact is just outside the field-of-view near the bottom-right corner.

The 0.5 mm thick single-crystal diamond sample was the most promising due to its low surface resistance however issues arising due to a low ablation threshold were still present. Measurements were also made difficult due to significant surface roughness and seemingly random pits across the surface as mentioned previously in Chapter 2.2. Together these issues made accurately determining the etch rate difficult as too much power would ablate the diamond and too little made identifying etched pits troublesome, as will be discussed shortly.

To reduce the likelihood of ablation, the UV objective lens was switched from a 20x objective to a 5x objective. This would result in a much larger beam spot on the sample, and therefore place greater limits on the minimum possible device size, but would also reduce the risk of ablation as the beam power would be less concentrated. Furthermore, it was assumed at this stage that the beam would need to be raster scanned to etch a sufficiently wide region around the Au contacts to achieve electrical isolation. Hence a wider beam spot would mean fewer scans and therefore shorter etch times, although it would later be discovered that raster scanning the beam to achieve wider etch lines was unnecessary. However, it was quickly noted that the 5x objective lens appeared to have a much greater throughput than the 20x objective and ablation of the diamond surface was still an issue. Optical

interferometry confirmed what was visible to the unaided-eye; an etch rate calibration at 150 mW using the 5x objective was ablating the 0.5 mm thick single-crystal diamond to a depth of around 10  $\mu\text{m}$  as shown in Figure 4-4.

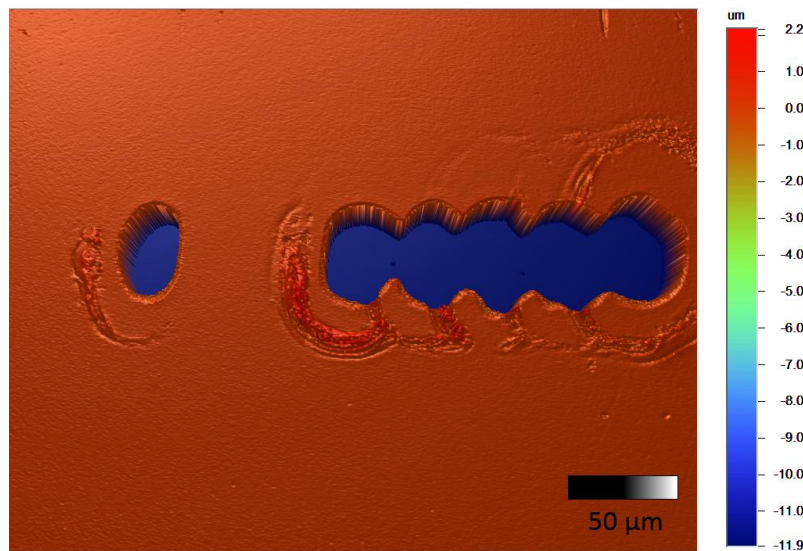


Figure 4-4 Optical Interferometry (VSI) image of ablation of the 0.5 mm thick single-crystal diamond during etch-rate calibrations using the 5x objective lens and 150 mW incident power. Each oval-shaped ablation crater was formed during a stationary exposure due to the astigmatism in the beam profile.

Regardless of the higher throughput of the 5x objective, and the still present potential for ablation, experimentation continued with the new objective as it provided a wider field-of-view on the CCD camera due to the objective both focussing the beam on the sample and passing the reflected light to the camera. This made locating etch locations more convenient than the 20x objective where a single Au contact would take up the entire field-of-view. A follow up etch rate calibration was undertaken at reduced power, however distinguishing the etched pits from the surface roughness proved difficult. The etched pits, as seen in Figure 4-5, are much less well defined than on previous samples (c.f. Figure 4-2) and the uneven surface introduces significant uncertainty to the etch depth measurement. Due to the difficulty in identifying and measuring the depth of the etched lines, the incident power was tuned to  $(40 \pm 5)$  mW using the IR half-wave plate and an arbitrary feed-rate of 1.5 mm/min was chosen for subsequent etches. These conditions were chosen as a convenience as it meant a single Au contact would be isolated in one minute in the absence of ablation; due to the limited resources available, a new diamond sample with low surface roughness could not be immediately sourced and these arbitrary conditions would allow progress to continue despite the unknown etch rate.



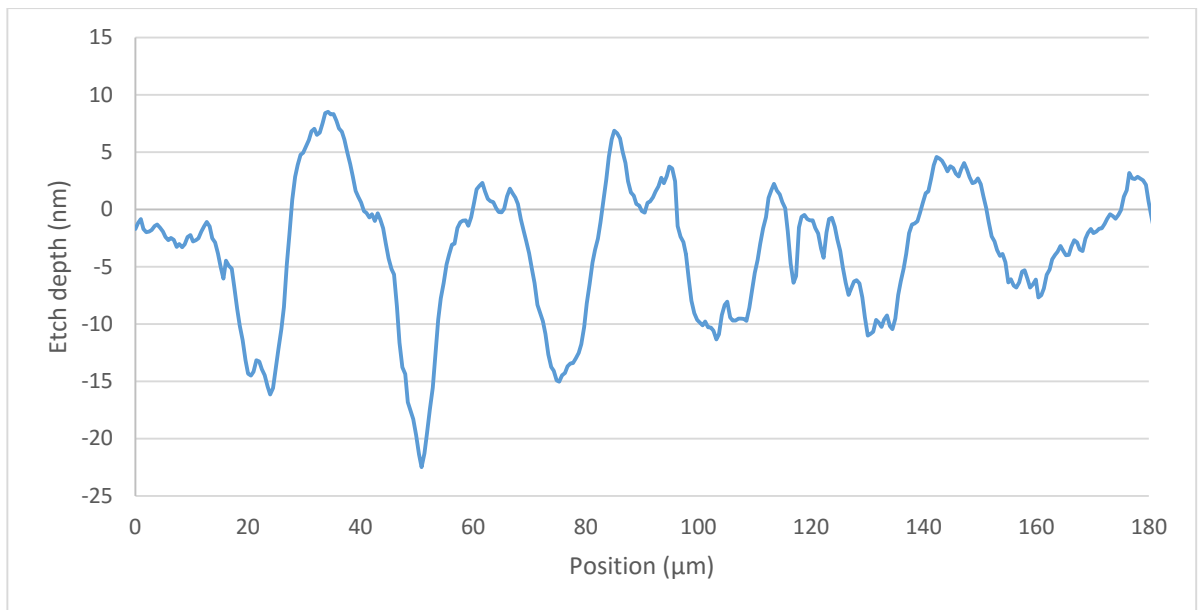


Figure 4-5 Etch depth calibration on 0.5 mm thick single-crystal diamond at low incident power. Each significant dip is a single pit, etched for 2 mins, taken at set intervals around the focal plane in order to locate the precise focus. The deepest pit will correspond with the position of the focal plane of the objective. The depth of the each etched pit is difficult to determine due to the significant surface roughness of the diamond.

## 4.2 Early Electrical Isolation Attempts

Early attempts to electrically isolate a Au contact from the surrounding diamond surface were partially successful. Due to saturation of the pixels on the CCD it is difficult to determine the precise location of the focused UV beam on the diamond surface. Imprecision in the positioning of the beam results in the Au contacts being ablated and scattered across the surface as seen in Figure 4-6. This is possible even at very modest incident power and will induce ablation of the diamond when it otherwise would not. The approximate position of the focused beam may be estimated by careful observation of the CCD output and noting the position on the monitor screen where a glass microscope slide appears to be damaged by the incident beam. The stage is then re-positioned so the diamond is aligned relative to the marked position on the monitor screen.

Due to the difficulty of calibrating the etch rate as a result of the rough diamond surface, the laser focus was largely adjusted by eye as well as on glass slides as detailed in Chapter 2.1. The procedure established for finding the focus was not as precise as the etch depth calibrations discussed above and likely resulted in a slightly de-focussed beam spot however, given the limited resources available, it was the best option at the time to see forward progress. Using the arbitrary feed-rate of 1.5 mm/min, an incident power of 40 mW and an estimated beam width of 25  $\mu\text{m}$ , the UV beam was scanned around several Au contacts in a rectangular path. The beam was offset from the edge of the Au contacts by a minimum of 50  $\mu\text{m}$ , or twice the estimated beam width, and up to 125  $\mu\text{m}$  or half the distance from one Au contact to an adjacent contact. The resistance between the Au contacts, which had been etched around, and the adjacent contacts was measured. Prior to etching the resistance between adjacent Au contacts was less than 10 k $\Omega$ , recall Figure 3-4; post-etching the resistance between adjacent Au contacts was beyond the range of the electrometer, suggesting that the etched contact had been electrically isolated from its neighbours. The electrometer, a Fluke 45 Dual Display Multimeter, has a rated resistance range of 0-100 M $\Omega$  [62] although readings of up to 300 M $\Omega$  may be

obtained by increasing the measurement rate and consequently decreasing the measurement precision. Etching a rectangle around a pair of Au contacts under the same conditions likewise appeared to isolate that pair from their neighbours whilst allowing conduction between the two contacts inside the isolation track.

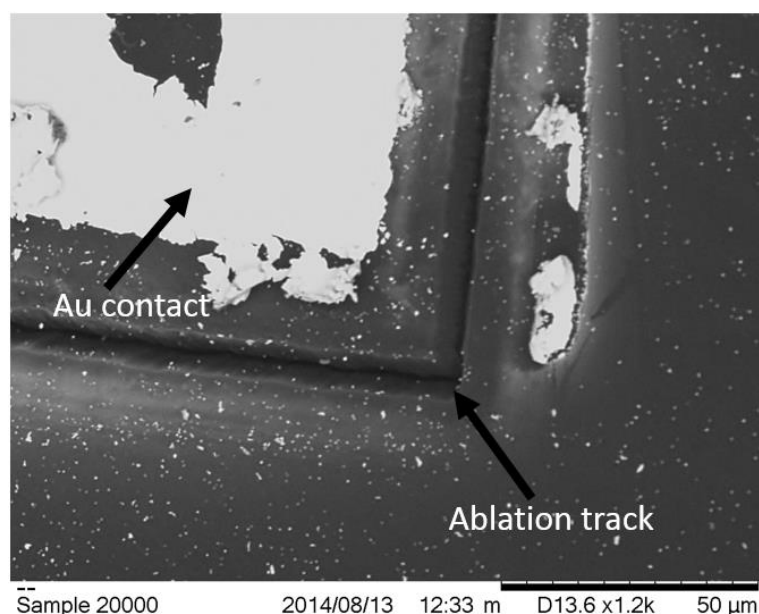


Figure 4-6 SEM image taken at 5kV of diamond ablation induced by a misaligned laser beam scanning across a Au contact. The bright specs scattered across the surface are Au that has been knocked loose by the passing beam.

Two pairs of Au contacts were isolated with a simple rectangle. For the first pair the beam was offset from the Au contacts by 50  $\mu\text{m}$  and for the second the Au contacts were given a wide berth of 125  $\mu\text{m}$ . Following these etches, the beam offset was kept at 50  $\mu\text{m}$  as this was deemed a satisfactory distance from the Au to avoid ablating either Au or diamond. The resistance measured between each pair of Au contacts is recorded in Table 4-1. For a functioning semiconductor device, a more appropriate isolation etch would be akin to the schematic in Figure 4-7, with a narrow channel connecting the two Au contacts with space either side of the channel for the gate electrodes. Several such structures were etched, again with the details listed in Table 4-1. Immediately after etching the rectangular channels the resistance between the two Au contacts was measured using the Fluke 45 electrometer. The narrow rectangular etch displayed a resistance of 350 k $\Omega$  whilst the wider rectangular etch displayed a lower resistance of 120 k $\Omega$ . However, prior to the resistance measurement, the diamond had moved from an enclosed environment at a relative humidity of 100%, moved outside between buildings from the semiconductor lab to the laser lab and back (relative humidity 69% outside at that time according to the Australian Bureau of Meteorology) before being examined electrically in the semiconductor lab at a relative humidity of 50%. Seemingly as a result of the frequently changing humidity, the measured resistance was continually dropping due to the phenomenon observed earlier in Chapter 3. The diamond was then left overnight, giving the surface wetting-layer a chance to come into equilibrium with the air-conditioned lab in which the resistance measurement would take place. Surprisingly, when the resistance measurement stabilised, the narrow rectangular etch showed a lower resistance than the wider etch. The reason for this reversal in the relative resistance between the two etches is unknown.

Table 4-1 Resistance between isolated Au contacts. The offset is the distance between the centre of the beam path and the Au contacts. All resistance measurements were taken at 51% humidity. Resistance measurements in parentheses are follow-up measurements demonstrating the difficulty in repeatability. As such the reproducibility of the measurement is a far greater source of longer-term uncertainty in the measurements than the measurement uncertainty.

Design	Offset ( $\mu\text{m}$ )	Channel width ( $\mu\text{m}$ )	Resistance ( $\text{k}\Omega$ )
Rectangular	50	335	44 $\pm$ 1 (350)
Rectangular	125	495	90 $\pm$ 1 (120)
Narrow Channel	50	25	110 000 (280 000)
Narrow Channel	50	50	763 $\pm$ 1

The narrow channel etches were more consistent with expectations in regards to their relative resistance but just as difficult to repeatably measure as the rectangular etches. An initial measurement of the 25  $\mu\text{m}$  narrow channel resistance put it at 110 M $\Omega$  however later measurements of 280 M $\Omega$  were taken days later at the same room humidity. This measurement was near the maximum range of the Fluke 45 multimeter, which had difficulty maintaining this reading and would later provide motivation towards switching to a programmable electrometer (Keithley 617) capable of measurements in the 100's of giga-ohm range. These measurements make clear the difficulty in obtaining precise and repeatable measurements of the surface resistance either due to the inconsistency of the wetting-layer or due to difficulties using the Au-plated electrode needles.

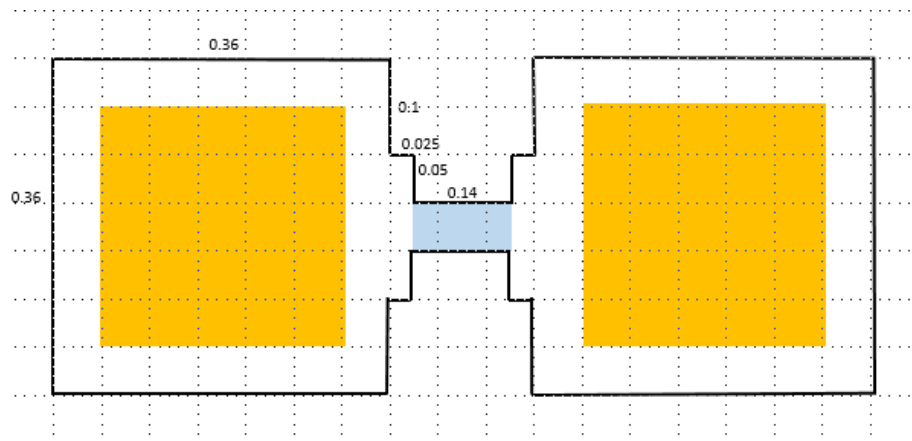


Figure 4-7 Narrow channel isolation etch schematic. The yellow areas are the Au contacts; the black line shows the etching path, and hence oxygen-termination around the contacts. The blue area indicates the conducting channel connecting the two contacts where fine control of the surface-termination is desirable. All white space plus the blue area would be hydrogen-terminated surface. The beam would approximately fill one square on the grid using the 5x objective. All measurements are in mm.

#### 4.3 Partial etching and dopant modification

Partial isolation etches were also attempted. In order to fabricate a working transistor, the number of charge carriers in the channel between the Au contacts i.e. source and drain, needs to be controllable. In the case of the diamond p-type surface channel, the number of carriers is determined by the surface-

termination. Therefore modification of the surface termination along the channel between the contacts is required. This is achieved by light etching the channel and thereby partially substituting the hydrogen-terminated surface with an oxygen-terminated surface.

To create an insulating surface on hydrogen-terminated diamond only a mono-layer of carbon atoms need be etched, with the layer below becoming oxygen-terminated. Therefore if the conditions for removing a mono-layer could be identified, the requirements for a partial surface-termination modification would be quantifiable and performed by scaling the power conditions and/or the etch exposure time. Due to the difficulty in determining the etch rate as a result of the surface roughness of the available diamond sample, an attempt to empirically determine the partial etch conditions was made by varying the feed-rate and etching a square around a single Au contact. The resistance between the partially isolated contact and an adjacent contact was measured using the Fluke 45 multimeter and the results are recorded in Table 4-2.

Table 4-2 Partial etch feed-rates and resistance between neighbouring Au contacts measured using a Fluke 45 Dual Display Multimeter. Incident UV beam power:  $40 \pm 5$  mW. Room humidity: 50%

Feed-rate (mm/min)	Resistance (k $\Omega$ )
1.5	> 300 000
5	> 300 000
15	27 000
30	146
50	39

Given an average ‘un-etched’ resistance between the Au contacts of 10 k $\Omega$ , this result demonstrates the viability of modifying the surface termination, and hence conduction, using the direct-write laser process. This ability to modify the surface resistance from k $\Omega$  to M $\Omega$  is promising for the construction of field-effect transistors where the control of the dopant level in the source-drain channel is required.

Subsequent to the apparently successful isolation etches, an attempt to visualise the etched surface was undertaken using optical interferometry and back-scattered scanning electron microscopy (SEM). However, neither technique was able to resolve the surface modifications created by the UV etching process. Figure 4-8 is an SEM image of a pair of Au contacts that had been apparently electrically isolated from one another by an etched channel around the Au contact on the left. The lack of any visible channel in either this image or in the optical profiler suggests that there has been very little etching of the diamond surface. This is not unexpected as electrical isolation of the contacts would not require a deep etch, merely that the surface termination be switched from hydrogen to oxygen by the etching of a mono-layer of carbon atoms. Initial SEM work was done at the Macquarie University ANFF OptoFab Node using a bench-top SEM operating at a minimum of 5 kV with an EDX<sup>1</sup> mode at 15 kV.

---

<sup>1</sup> EDX, or Energy Dispersive X-ray spectroscopy, uses a semiconductor detector to classify the x-ray emissions from the sample, which are emitted under electron bombardment in the electron microscope. The spectrum of this radiation can be used for elemental identification [63].

Due to the differing negative electron affinities (NEA) between the H- and O-terminated surfaces, there should be a substantial difference between the secondary electron yields from these regions which would appear as a change in contrast in the image, however at this kinetic energy range, the SEM was unable to resolve the contrast between the H- and O-terminated surfaces. This is likely due to the increased sampling depth of the high-energy electron beam of this instrument. Furthermore operating the SEM under EDX mode failed to see the oxygen-terminated channel created by the etching process and instead simply saw oxygen over the entire region scanned, likely due to water on the surface, as seen in Figure 4-9.

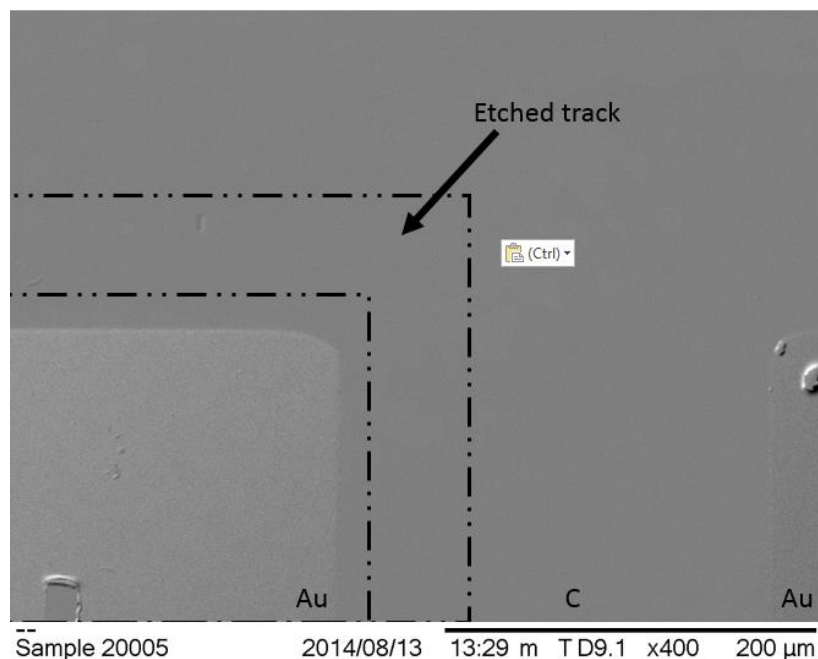


Figure 4-8 SEM image taken at 400x magnification and 5kV of a potential isolation etch. A 40 mW UV beam with a waist of 25  $\mu\text{m}$  was traced between the dotted lines. A change in the contrast of the image would indicate a change in the electrical conductivity of the surface and hence a change in the surface termination, but no such change is visible.

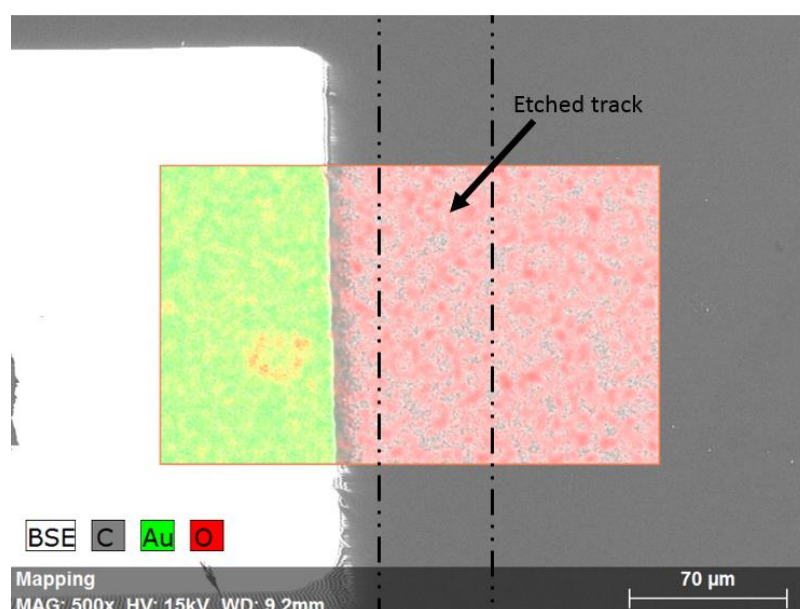


Figure 4-9 SEM image taken at 15kV on EDX mode displaying the location of atomic C, Au and O. An etched channel around the Au should pass between the dotted lines and appear as a track of oxygen-termination but instead the entire region appears to be covered in oxygen.

With a lack of evidence of the surface-termination change in the SEM image, two avenues of progress were explored: a further attempt to quantify the etch rate was made, and the Fluke 45 multimeter was replaced with a Keithley 617 programmable electrometer capable of measuring resistance up to 200 GΩ [64].

Determining the etch rate on the 0.5 mm thick single-crystal sample was complicated by the surface roughness and random pits on the surface due to the extended time spent in the hydrogen-plasma. Under low power conditions the uneven surface made distinguishing the pits and determining their depth difficult whilst increasing the power led to ablation. Therefore a low power and slow moving etch was undertaken to draw a 'plus sign' in one corner of the diamond. The slow feed-rate would ensure a more significant etch depth and the shape would make the etched region distinguishable from the surface roughness. Figure 4-10 shows the etched region and the depth profile as measured by the interferometric profiler. The etched 'plus sign' is visible in the high contrast image and is determined to be approximately 10 μm deep by averaging across the surface beside the etched region.

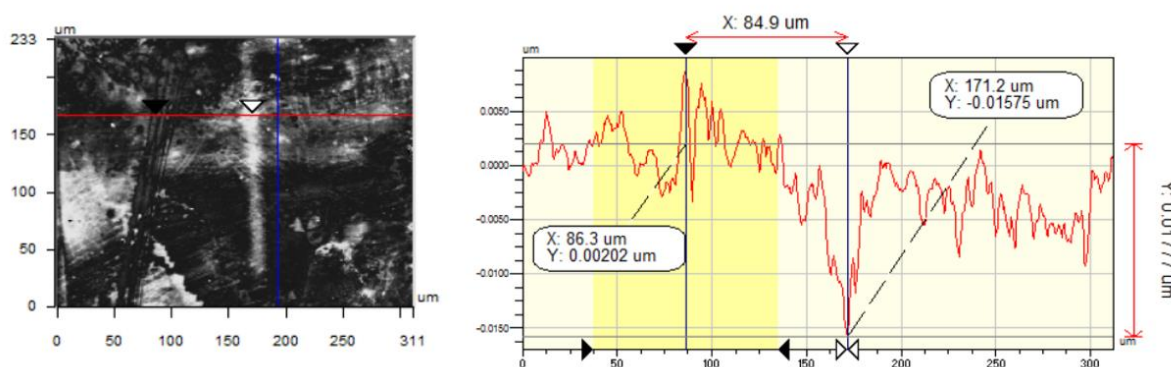


Figure 4-10 Optical interferometry scan (PSI) and cross-sectional depth profile of a 0.2 mm long 'plus sign' etched on diamond. Total exposure time was 40 min per arm. The depth profile is taken along the red line of the crosshair; the two positions marked are shown along the line.

Given the known feed-rate of the translation stage of 0.005 mm/min and an approximate etch depth of 10 nm, we can estimate the etch depth at the same power for any other feed-rate as the etch depth is proportional to the number of cumulative pulses and hence exposure time [3]. In particular, the arbitrarily chosen feed-rate of 1.5 mm/min is 300 times faster than 0.005 mm/min, hence a 300 times shorter exposure time for a given spot, therefore the etch depth should be 300 times less or 0.033 nm. The bond length of carbon atoms in diamond is 0.154 nm [12]. This line of reasoning suggests that the Au contacts etched with a feed-rate of 1.5 mm/min are not completely isolated and may in fact have giga-ohm resistance as this etch depth is not sufficient to fully replace the hydrogen-termination with an oxygen-termination. Further, with a giga-ohm resistance between adjacent contacts, the contrast in the SEM images above, due to the difference in conductivity, would almost certainly not be visible. Continuing this line of reasoning, to remove a mono-layer of carbon atoms and achieve a complete isolation, a feed-rate of 0.325 mm/min would be necessary with a slower rate obviously etching deeper and ensuring isolation.

Before any further etches were undertaken, the previous 'isolation' etches performed at a feed-rate of 1.5 mm/min were re-examined using an electrometer with a giga-ohm resistance range and were found to be conducting with a resistance of 30 G $\Omega$  between the 'isolated' contact and the nearest adjacent 'un-etched' contact. This result explains the lack of contrast in the SEM images between conducting and non-conducting surfaces. There is a great deal of uncertainty in this figure however, due to the difficulty in measuring resistance in the giga-ohm range, the photo-induced conduction brought about by the halogen-lamp of the optical microscope on the probe station and the variable humidity in the semiconductor lab. Building on the previous partial isolation attempts, several new partial and full isolation etches were undertaken and the resistance measurements are documented in Table 4-3.

Table 4-3 Partial etch feed-rates and resistance between neighbouring Au contacts measured using a Keithley 617 Programmable Electrometer. Incident UV beam power:  $40 \pm 5$  mW. Room humidity 56-59%. Un-isolated surface resistance between adjacent contacts: 16 k $\Omega$ . Data for feed-rate of 10 mm/min was unavailable as that Au contact had been damaged and there were no other contacts available to repeat the etching as they were designated for other investigations. Estimated fraction of a mono-layer removed was calculated through the reasoning described above for the feed-rate required to remove a complete mono-layer.

Feed-rate (mm/min)	Resistance (k $\Omega$ )	Estimated fraction of a mono-layer removed
<b>0.1</b>	> 200 000 000	3.25
<b>0.325</b>	> 200 000 000	1.00
<b>1.5</b>	45 000 000	0.217
<b>5</b>	2 600 000	0.0163
<b>15</b>	140 000	0.0217
<b>20</b>	6 600	0.0163
<b>30</b>	310	0.0108
<b>40</b>	840	0.008125
<b>50</b>	565	0.00650
<b>100</b>	27	0.00325

Whilst the effects of photo-induced conduction due to the bright halogen-lamp were largely ignored when measuring k $\Omega$  resistances, the effects were much more pronounced when measuring G $\Omega$  and high M $\Omega$  resistances. A standard procedure was initiated for the measurements in Table 4-3 due to the factors mentioned above; once contact was made between the probes and Au contacts, the halogen-lamp of the microscope was switched off and the resistance recorded after one minute. This procedure gave the electrometer time to stabilise towards the true resistance without the humidity in the room changing over the course of the measurement. Over the series of measurements however, the humidity in the room varied by up three percentage points. Two points are immediately obvious from the data in Table 4-3: 1) the measurements vary from the original data in Table 4-2, and 2) when comparing the feed-rates between 30 and 50 mm/min (in particular), it is clear that the uncertainty inherent in these sorts of measurements is significant. Over repeated measurements, the Au contacts became increasingly damaged, making reliable and repeatable measurements difficult. Completely removing the Au contacts was a frequent occurrence, however the mere softness of the Au contacts meant they were constantly being deformed and the contact surface (and resistance) was changing with every measurement. Furthermore, often the resistance would slowly increase (or decrease, if the halogen-lamp was on) over time. To determine whether this was a measurement problem or a real effect, the current-voltage (I-V) characteristic was to be measured over time. Unfortunately this phenomenon was not able to be investigated as misadventure would eventually damage the remaining



Au contacts before this measurement could take place and this phenomenon was not observed on subsequent samples.

The resistance vs. feed-rate (i.e. exposure time) data from Table 4-3 is plotted on a log-log plot in Figure 4-11. The best fit to the data shows a power relationship with an index of -3.53. The significance of this relationship is not fully understood but would likely be related to the reduction in conductivity by partial removal of hydrogen-termination in a two-dimensional area and the measurement of a linear resistance across that area.

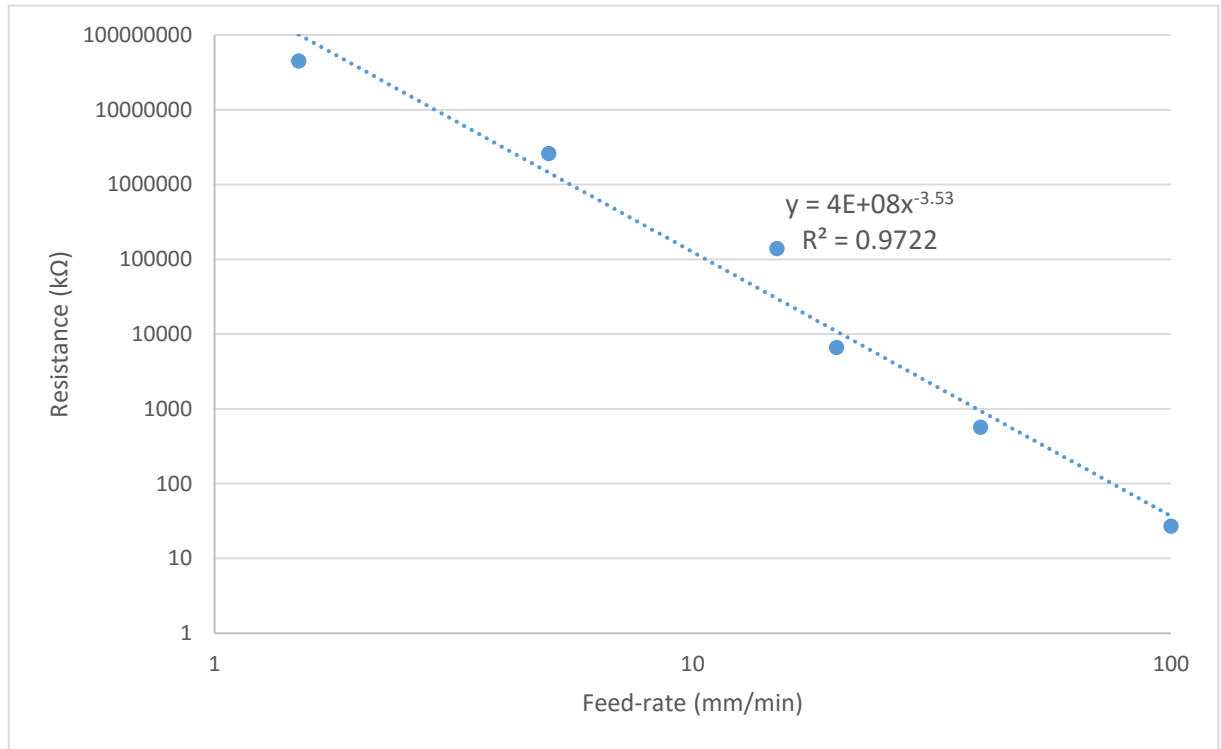


Figure 4-11 Resistance change between two Au contacts separated by 0.25 mm with exposure time to a 257.5 nm beam at 40 mW.

#### 4.4 Isolated conducting paths

The next step towards demonstrating the viability of fabricating semiconductor devices using the direct-write UV etching process was to determine whether two conducting tracks could be written side-by-side and insulated from each other. The minimum distance two tracks may be separated is determined by the beam width of the laser, which in this case is 25  $\mu\text{m}$  with the 5x objective lens. A 40 mW beam was traced around four Au contacts at a feed-rate of 0.325 mm/min to ensure electrical isolation to at least 200 G $\Omega$  between the contacts inside the etched region to the neighbouring contacts outside, as determined from the results in Table 4-3. The outline of the intended etch is drawn in red over an optical image of the diamond surface in Figure 4-12. Note the obvious signs of ablation around the etch path. At this stage of the project, ablation was again becoming an issue as previously 'safe' powers and feed-rates were causing sporadic ablation of the diamond surface. To determine the cause of this ablation, the incident power was re-checked after the ablation seen in Figure 4-12 occurred and was found to be varying over short timescales by as much as 25%, which had not been seen previously. However when ablation was also noted on repeat attempts of this etch, the power was checked immediately and found to be a stable 40 mW. It was also suspected that a stray green beam was directed at the sample although that would require that the beam be reflected out of the Pellin-Broca

prism to the fused silica cylindrical lens then back to the prism at the precise angle to then coincide with the UV output. This would vastly reduce the power of the green beam which was in fact found to be only several mW by placing a green reflecting mirror in the beam path before the stage and directing the beam to a power detector. Regardless, this green beam was reflected away from the sample but did not prevent the ablation from occurring. The slower feed-rate of the translation stage was also ruled out as a possibility as ablation was noted in real-time as the stage was controlled manually at vastly higher speeds. The next hypothesis put forward to explain the appearance of ablation was that the diamond had become dirtied by UV absorbing contaminants. The sample was subsequently washed in ethanol to remove any water soluble contaminants followed by acetone to remove any hydrocarbon contaminants. After each wash the sample was dried by passing dry nitrogen gas across the surface. Despite washing the sample, further ablation occurred when attempting this etch on a fresh region of diamond in a similar fashion to that seen in Figure 4-12.

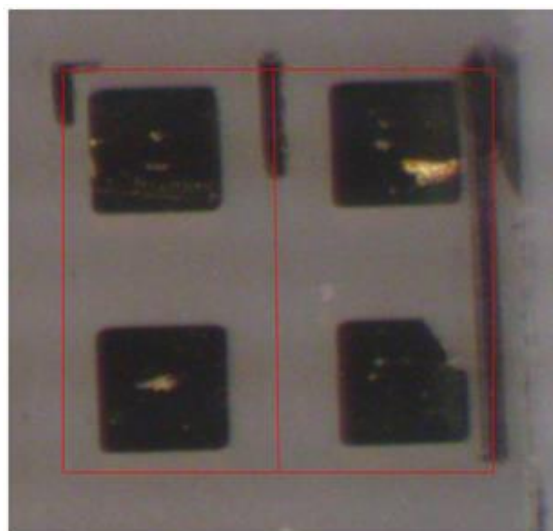


Figure 4-12 An attempted etch to isolate two pairs of Au contacts from the other pair whilst maintaining conduction between each pair. Clear signs of ablation are visible under the red outline which depicts the location of the etched track. Despite the ablation, each vertical pair of Au contacts was electrically isolated from the other pair.

To reduce the risk of ablation, the feed-rate of the translation stage was increased by a factor of four to 1.3 mm/min and the etch path was looped four times so that the total exposure time remained constant with the previous etch attempts. This attempt was successful in isolating each pair of Au contacts from the other pair (to  $>200\text{ G}\Omega$ ) without ablating the diamond, while the resistance between each of the pairs of Au contacts was still measured as  $8\text{ M}\Omega$  at a relative humidity of 60%, i.e. the pairs were isolated from each other but still connected within each pair. This figure is rather high given measurements of tens to hundreds of kilo-ohms were measured previously for similar etches (c.f. Table 4-1), still it demonstrates the ability to write adjacent and isolated conducting regions in the surface-termination.

At this point of the project, the front face of the 0.5 mm thick single-crystal diamond was no longer usable as all 60 of the Au contacts had either been electrically isolated by etching or had been removed by ablation, the Au-coated probe tips or by misadventure. In order to continue, the diamond sample was washed in Aqua Regia<sup>2</sup> and the back side was hydrogenated as mentioned in Chapter 2.2. A new

---

<sup>2</sup> 1:3 concentrated nitric and hydrochloric acids

mask was employed to deposit a smaller number of Au contacts with greater spacing between them, which would allow additional room for more complicated etched structures. The re-hydrogenated diamond would provide four regions for field-effect transistor devices to be fabricated. The scripting code for the final etching experiment was tested on glass before attempting on diamond; the scripting code for the FET is found in Appendix 7.2 and an example of the structure etched on glass is shown in Figure 4-14 . Before the FET design could be etched onto the back face of the 0.5 mm single-crystal diamond, the etch rate needed to be determined as it was unknown if the etch rate on the back face would be identical to the front face. To test this, a small L-shape was etched in one corner of the diamond film with the same power as the previous ‘plus’-shaped etch which was used to determine the etch rate on the front face. The etched region is shown in Figure 4-13 and shows two interesting observations: 1) the etch rate is similar to that previously measured for the front face, and 2) the etch depth is asymmetric in the x-y plane. The later was also seen in Figure 4-10 and is the result of the highly elliptical beam produced by the laser etching system. At this stage in the project the resources were not available to correct this issue and would require a custom engineered silica lens to correct.

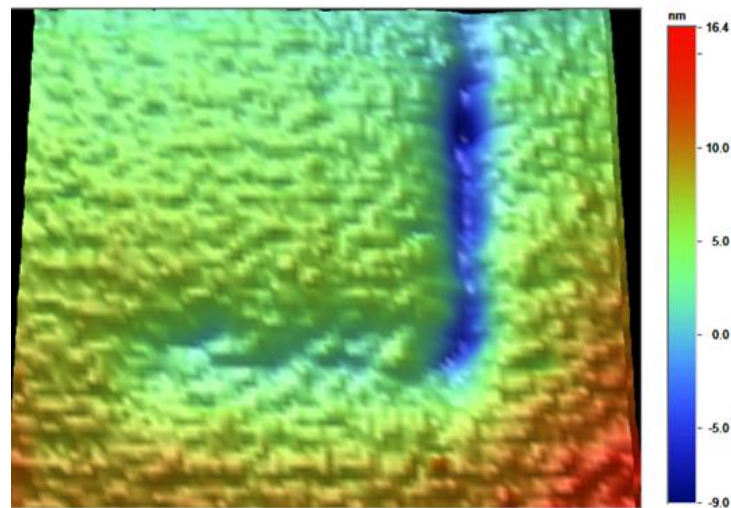


Figure 4-13 Optical interferometry scan (PSI) of a small L-shaped etch on the back side of the 0.5 mm thick diamond. The consequence of the elliptical beam profile is evident in the asymmetrical etch depth along each arm.

#### 4.5 Fabricating Field-Effect Transistors

The first attempt at defining a FET structure on diamond (referred here-after as FET 1) was achieved by etching the diamond surface around the Au contacts to define a channel between the source and drain. Then the drain and gate were isolated from the bulk surface by etching a path around them (a second etch around the drain was also performed to further isolate the drain from the gate and minimise leakage current). Lastly the source-drain channel was quickly raster-scanned perpendicular to the channel length to reduce the hydrogen-termination and control the number of charge carriers in the channel. The structure of this etch is shown in Figure 4-14. The resistance measurements between the key components of the device, and subsequent devices, are listed in Table 4-4. As noted earlier, the difficulty with the reproducibility of the measurements introduces a far greater uncertainty in the values quoted in Table 4-4 than any instrument error. As such the values quoted in Table 4-4 should not be taken as read. As seen in the table below, photo-induced conduction significantly

influences the behaviour of the device. In the dark the device is isolated from the surrounding surface (resistance  $>200\text{ G}\Omega$ ). Likewise the gate and drain are isolated in the dark. However under the bright light of the halogen-lamp on the probe station, which is necessary to visualise the sample and make electrical contact, photo-induced carriers are mobile enough to achieve conduction under the oxygen-terminated (insulated) surface between the gate and drain.

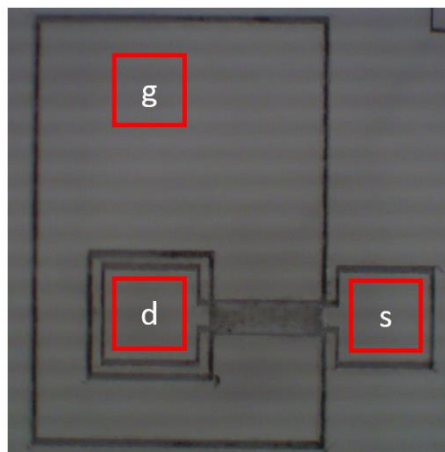


Figure 4-14 Optical micrograph of a practice 'FET' etch on glass. The locations of the drain, source and gate are marked.

Due to the high resistance ( $100\text{ G}\Omega$ ) of the source-drain channel in the first FET, a second attempt (FET 2) was made which would forego the raster-scanning across the channel. Despite the channel remaining un-etched, the source and drain were isolated from one another to greater than  $200\text{ G}\Omega$  with the light off. Furthermore, higher resistances were measured between the components during photo-conduction induced by the lamp. It was proposed that possible scattering of UV light was modifying the hydrogen-terminated surface outside of the intended beam path. This hypothesis was supported by the observation that surface resistance of  $10\text{-}100\text{ M}\Omega$  was present on the open surface near where the etches had been performed, whilst resistance of  $10\text{-}100\text{ k}\Omega$  was present on the opposite side of the diamond film to where the surface had been exposed to the beam. A third and final FET (FET 3) was etched with a much wider channel. The wider channel was etched in an attempt to minimise the influence of the scattered UV light over the width of the channel. However this device too failed to conduct between the source and drain and was further marred by quite significant ablation.

Table 4-4 Resistance measurements between components in the hydrogen-surface channel field-effect transistor devices etched on diamond. Measurements are given for cases where the device is illuminated by the halogen lamp of the microscope and in the dark. Prior to etching the average resistance between adjacent contacts separated by 0.625 mm was 13 k $\Omega$ . The variability between repeat measurements far outweighs any instrument error in the uncertainty of these measurements.

FET	Drain-Source Resistance (G $\Omega$ )		Gate-Drain Resistance (G $\Omega$ )		Inside Device to Outside Device	
	Light ON	Light OFF	Light ON	Light OFF	Light ON	Light OFF
FET 1	13	100	8	>200	1	>200
FET 2	30	>200	20	>200	17	>200
FET 3	35	>200	22	>200		

Nevertheless, the I-V characteristics of FET 1 were measured; both the halogen-lamp and the room lights were turned off to minimise the photo-induced conduction during FET measurements. It was speculated that high voltages would be required to meaningfully effect the channel due to both its high resistance and its great width, therefore a large negative gate bias voltage range (4-48 V) was applied and the drain-source voltage was likewise varied over a large range (0-48 V). As seen in Figure 4-15 there is significant noise in the data (hence the chart is displayed as a three-point moving average), due to measurement of sub pico-amp currents, but the gate voltage does appear to be influencing the channel. Note that due to holes forming the majority carriers through the channel, the drain-source current  $I_{ds}$  is increased with increasingly negative gate-voltage as electrons will be pushed away from the channel and additional holes attracted in.

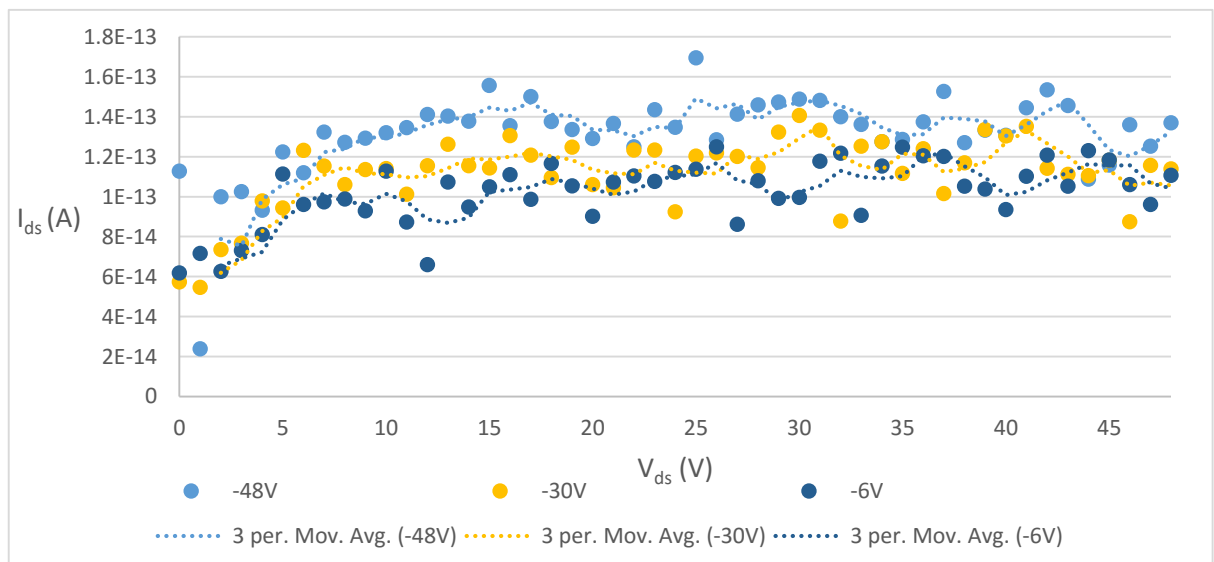


Figure 4-15 I-V characteristic of FET 1. Negative Gate Bias 4-48V, max  $V_{ds}$  48V. More data sets were taken which show the same trend but only three are shown here for clarity.

The large voltage range used appears to be sufficient to drive the device to saturation; follow-up measurements used lower voltages to investigate the ohmic region of the device. When gate voltages

between -4 V and +4 V were employed with drain-source voltage  $V_{ds}$  from 0-10 V, we see a non-linear response below 3 V  $V_{ds}$  followed by a linear trend as seen in Figure 4-16. If the device is modelled as a FET with a parallel resistor, then the FET characteristics will be extracted by removing the linear (ohmic) resistive component.

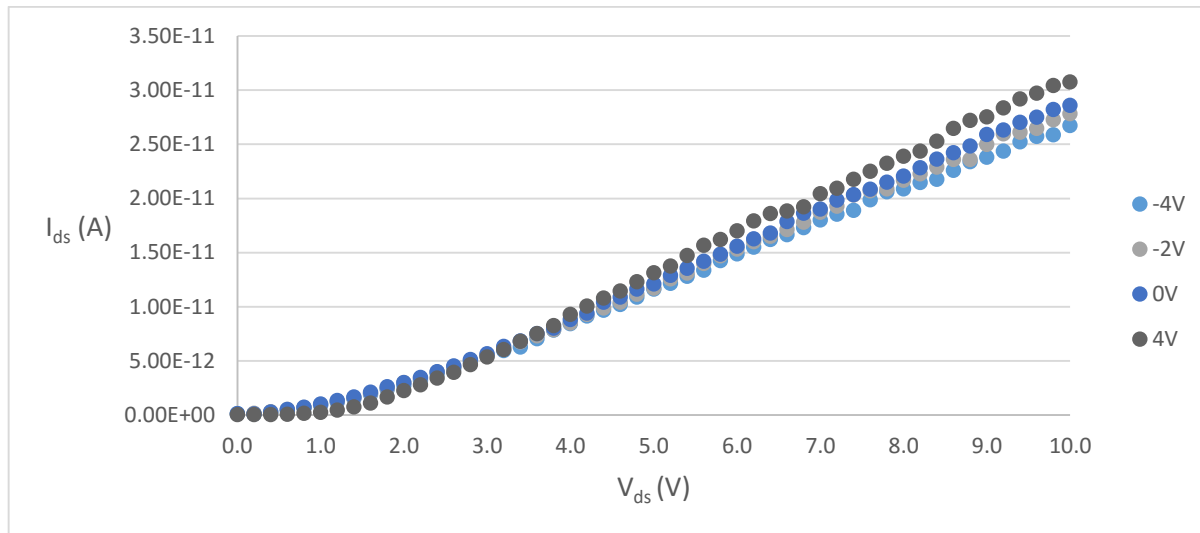


Figure 4-16 I-V characteristic of FET 1 with reduced voltage range. If the FET is modelled with a resistor in parallel, then the linear trend past ~4 V corresponds to a resistance of ~300 G $\Omega$ . Several data sets are omitted for clarity.

An average data set was calculated and the slope of the linear component determined, which corresponded to a resistance of 309 G $\Omega$ . The linear component was then subtracted from each data set and plotted in Figure 4-17 and Figure 4-18 for positive and negative gate voltages respectively. With the linear component subtracted, the characteristic curves resemble those of FET behaviour, however the curves for positive and negative gate voltages are not consistent with one another. This is seen clearly in Figure 4-19, which plots all data sets together.

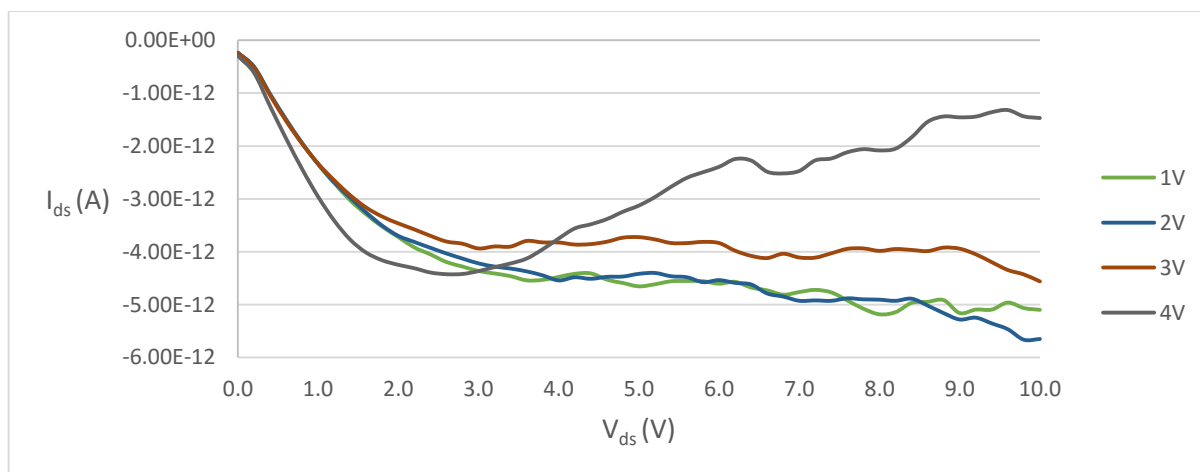


Figure 4-17 I-V characteristic of FET 1 for positive gate voltages, after subtraction of the linear trend.

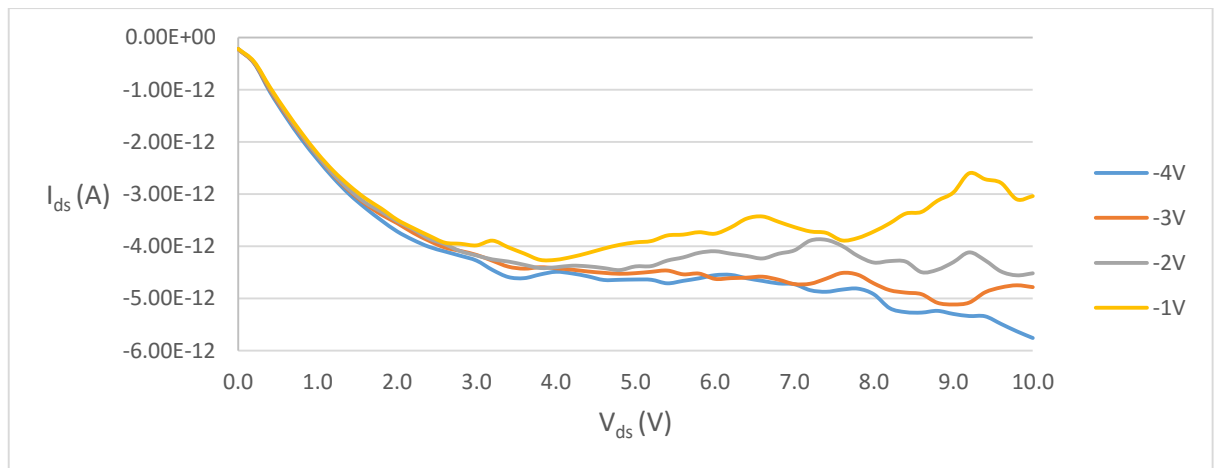


Figure 4-18 I-V characteristic of FET 1 for negative gate voltages, after subtraction of the linear trend.

Measurement of the FET curves was intrinsically difficult beyond the very low currents; significant light levels still present with the room lights off due to other devices operating in the lab, stray electric fields, and vibrations due to other operating equipment all appeared to influence the measurements. Changes in the relative humidity of the lab also cause uncontrollable variation, and this variation may account for the inconsistencies between the positive and negative gate voltage curves in Figure 4-19. Due to the design of the FET characterisation setup and software package, the positive and negative gate-bias measurements must be taken separately. Therefore if the humidity changed appreciably between collections of the two data sets then, although they may be internally consistent, they may not be directly comparable. This is seen in the data sets above; the curves for the positive gate voltages show systematic variation, likewise for the negative data sets, of decreasing (negative) drain-source current with increasingly positive gate voltage. A rapid change in the room humidity is a distinct possibility as the air-conditioning unit in the lab regularly flushes water through a grate-covered gutter in the floor. Unfortunately the humidity was not monitored between data sets, and the measurement was not able to be repeated due to time constraints. The odd shape of the +4 V curve should also be noted; the +4 V curve was the first measurement in this series and it was often noted that the first curve in a series displayed odd behaviour. It was postulated that this behaviour may be due to trapped charges in the channel prior to first operation after being stored for a period of time.

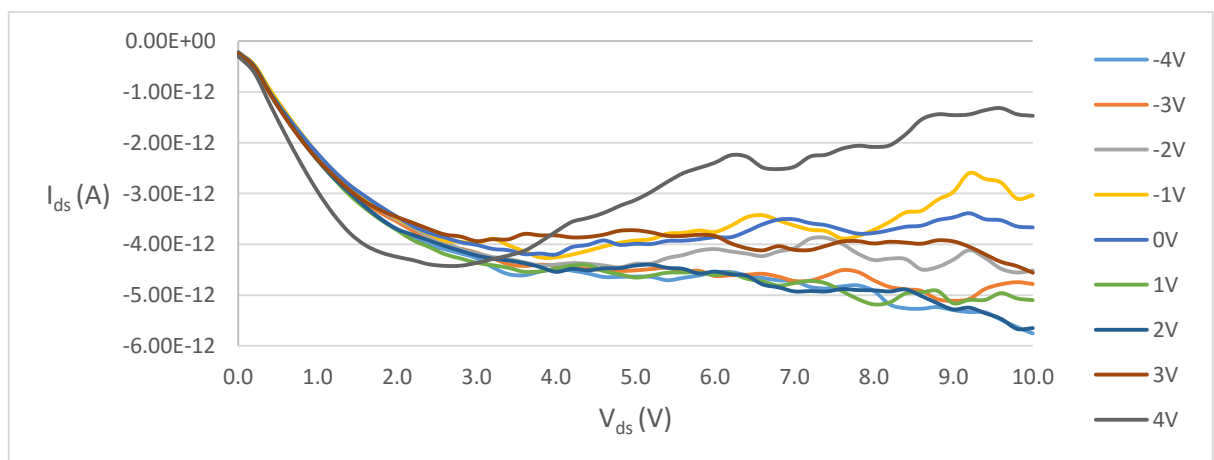


Figure 4-19 I-V characteristic of FET 1 for all measured gate voltages, after subtraction of the linear trend. The positive and negative data sets show self-consistency in the order of the I-V curves however the positive and negative sets are not consistent with each other.

In order to visualise the devices described above, the diamond chip was characterised using a field-emission scanning electron microscope. This device was able to resolve the change in contrast due to the difference in the conductivity of the oxygen- and hydrogen-terminated surfaces unlike the back-scattered SEM used previously. The three FET devices are seen clearly in Figure 4-20 in order, clockwise, from the top left. This is the first visual confirmation of the ability to write complex patterns into the surface termination of diamond using a pulsed UV laser.

Examining the width of the oxygen-terminated tracks in Figure 4-20 reveals the vertical and horizontal lines of FET 1 are approximately 80  $\mu\text{m}$  and 50  $\mu\text{m}$  wide respectively. This is wider than the focused beam width of the laser. This result suggests that either the laser was incorrectly focused or the pulsed UV beam induces oxidization over a larger area than the beam width, despite the etch depth profile coinciding with the square of the beam profile [3]. Due to the almost insignificant etch depth intended for these etches, it is not possible to compare the width of the induced oxygenation and the width of the actual etch.

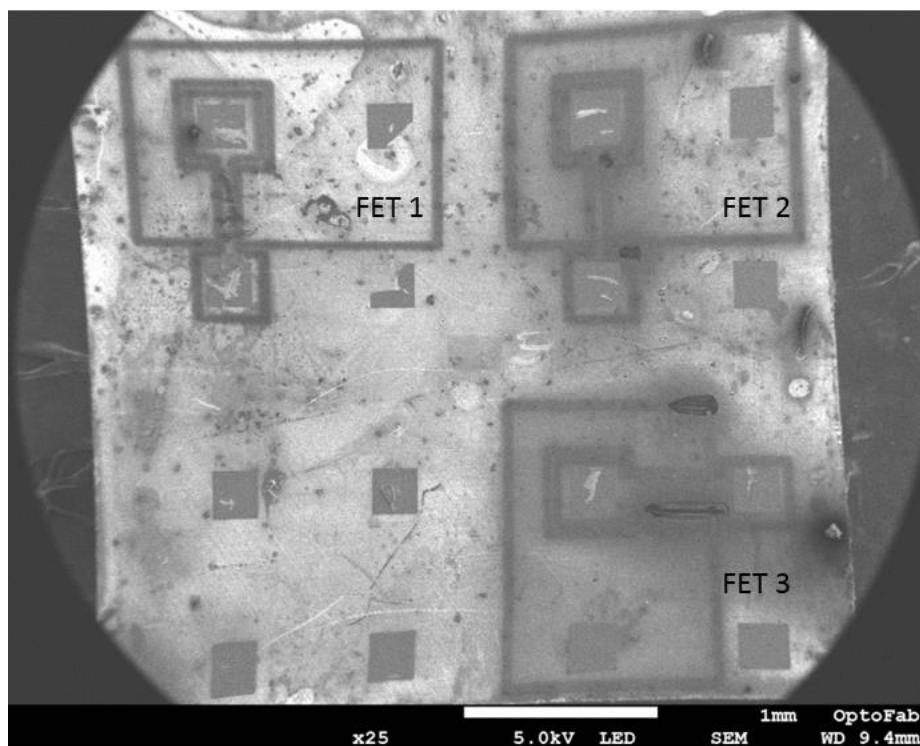


Figure 4-20 FESEM image of the FET diamond chip; FETS 1-3 clockwise from top left. Dark lines are attributed to induced oxygen-termination by pulsed UV laser etching. The slight distortion in the corners of the image are an artifact of the instrumentation.

By comparing the three devices it is clear that the contrast inside the gate is darker for FET 2 and FET 3 than for the FET 1, implying their gate regions are better isolated from the surrounding surface. This is verified by previous resistance measurements tabulated in Table 4-4. What is not clear however is: whether the scattered UV hypothesis can be confirmed from these images. Although there was notable difference in the resistance outside of FETs 1 and 2 compared to the open space with no device (or the location of FET 3 before it was written) there does not appear to be an appreciable difference in the contrast between those areas, excepting perhaps the area between FET 2 and FET 3. Furthermore, if significant UV scattering were present it should be noticeable just outside the etched regions though it is not obvious in Figure 4-20.



Several clear signs of ablation are present in FET 2 and 3. The significant ablation on FET 3 is visible with the unaided eye while conversely the small ablation craters in FET 2 were not immediately obvious and had not been visible under the optical microscope. These areas are seen clearly in Figure 4-21. It is apparent from these images the often fine line between surface modification and ablation of the surface. After each major component of the FET was drawn, the laser power was measured and corrected back to the desired 40 mW, if it had deviated. During etching of FET 3 the laser power rose to 80 mW by the end of one section of etching. It is unknown if a rise in the incident laser power caused the ablations seen in Figure 4-21. Other possible explanations may be: sub-surface defects in those areas lowering the ablation threshold, or dust or similar contaminants on the surface absorbing UV and triggering ablation of the diamond. In addition, Figure 4-21 further illustrates the vast differences in the removal rates between ablation and UV etching with the deep scoring of the ablation craters in stark contrast to the estimated mono-layer deep etching that is visible only due to the change in conduction it induces as a result of the modification of the surface-termination.

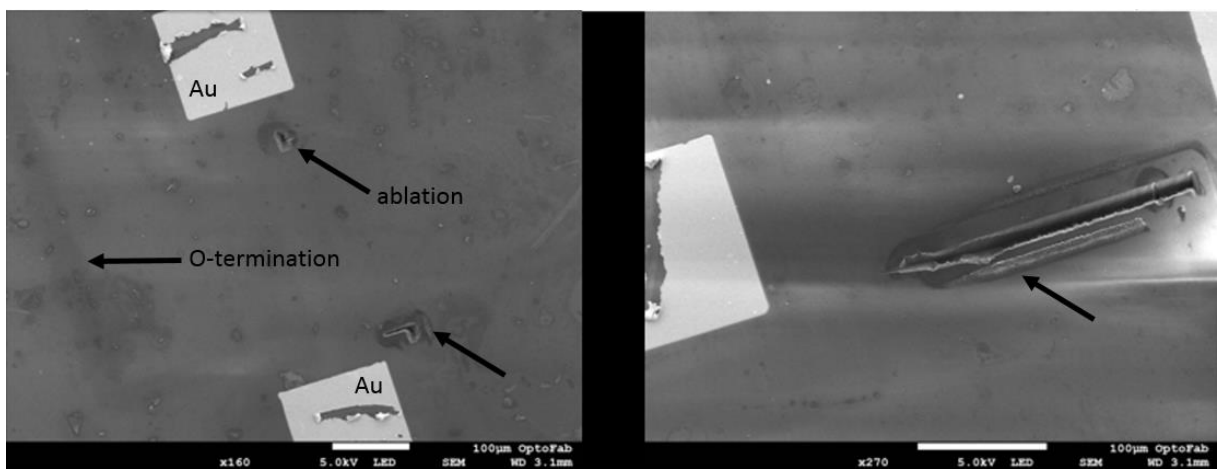


Figure 4-21 FESEM image of the FET diamond chip; ablation craters observed on FET 2 (left) and FET 3 (right). Also (barely) visible in the contrast are the oxygen tracks defining each device. Bright streaks across the images are attributed to surface charging by the electron beam.

## 5 Conclusions

Interest in diamond as a semiconductor material is driven by its high thermal conductivity, wide band gap and high breakdown electric field. These properties, together with a high carrier mobility, are expected to provide stand-out performance for diamond-based transistors in high-power and high-frequency operations. Exposure to hydrogen-plasma, either during- or post-growth, will impart a hydrogen-termination layer to the surface which will facilitate sub-surface p-type conductivity through an electron exchange between diamond and a thin water layer on the surface. Non-conducting regions or tracks are selectively defined by exposing the H-terminated surface to an oxygen-plasma as demonstrated by the myriad of devices found in the literature. In this report, non-conducting O-terminated tracks have been written onto an H-terminated diamond surface using a novel technique of 2-photon ultra-violet pulsed laser etching as first step towards a direct-write laser process for the fabrication of diamond semiconductor devices.

Previous investigations into the 2-photon UV etching phenomenon had been performed on oxygen-terminated diamond [3] and while it was known that the presence of oxygen was essential to the etching process [4] it was not known what effect an H-terminated surface would have on the etch rate; this project was the first step towards a systematic investigation of UV etching on an H-terminated surface. This is also the first demonstration of the ability to write complex patterns into the surface termination of diamond by way of pulsed UV laser techniques and demonstrates a versatile method for rapid-prototyping of functionalized diamond surface structures. It has been shown here that by etching (estimated) mono-layer deep tracks around Au contacts deposited on H-terminated diamond surfaces, thereby replacing H-termination with O-termination, that the conducting surface regions will be electrically isolated. An oxygen-terminated line, of similar dimensions to the beam width of the laser, between two conducting tracks has been shown to be sufficient to electrically isolate each track to greater than 200 GΩ. The minimum width of the O-terminated track is set by the laser beam width thereby raising the possibility of creating smaller structures with tighter constraints on the beam width using larger magnification lenses and diffraction-limited optics.

As well as demonstrating the ability to fully isolate conducting regions, the potential for reducing the conductivity by partially removing H-termination from an area has also been demonstrated for the first time. By reducing the exposure time, through increased speed of the beam across the surface, it is possible to modify the resistance between two points on the surface by many orders of magnitude. This is a very novel technique for controlling the surface doping compared with traditional chemical doping techniques.

Field-effect transistor (FET) structures were etched in the surface-termination of a hydrogen-terminated single-crystal diamond film, which were isolated to 200 GΩ. The FETs displayed significant resistance, were clearly sub-optimal devices and although full FET behaviour was not observed, the drain-source current  $I_{ds}$  was clearly influenced by the gate voltage  $V_{gs}$ . These results provide the basis towards a functioning p-type surface conduction diamond FET fabricated by a direct-write laser technique. Field-emission scanning electron microscopy has verified the creation of conducting tracks forming a simple flat field-effect transistor structure. This is the first visual confirmation of the ability to write complex patterns into the surface termination of diamond by way of pulsed UV laser techniques.

---

A method of reliable hydrogen-termination of diamond has been developed based on information in the literature although largely determined empirically. The procedure is able to reliably produce a low-resistance surface with minimal alterations to the surface roughness. Pairs of Au contacts deposited 0.24 mm apart on prepared H-terminated surfaces displayed an average resistance of 10 k $\Omega$  between them.

Future work will involve an attempt to understand the effect of humidity on the performance of diamond-based FETs or to avoid the problem entirely by coating the etched structure in MoO<sub>3</sub>, which has been shown to facilitate surface transfer doping and may provide a more stable adsorbate layer [35]. A greater understanding of the relationship between the removal of carbon atoms by 2-photon UV etching and oxidization of the surface is desirable as it may allow for finer control of the surface-termination modifications. This in turn would permit finer and more complex structures to be written in the surface-termination. Given the constant struggles with ablation of the diamond surface, a detailed study into the ablation threshold of hydrogen- versus oxygen-terminated diamond is warranted. Longer exposure times and/or higher incident power may also be explored as it would result in deeper etching and raise the possibility of creating three-dimensional devices rather than just changing the surface termination. The photo-conduction of the H-terminated surface is also of interest although it is likely a significant enough subject to warrant a separate program of study to the modification of surface-terminations. The demonstrated ability to control the surface-termination with a pulsed UV laser also opens up avenues for fundamental physics by defining and controlling the doping level of the hole sheet.

If diamond field-effect transistors can be reliably created using the techniques pioneered here, a further application would be to write multiple transistors in series on a single diamond chip all connected by p-type hydrogen-tracks e.g. a ring oscillator. A first step however would be to simply improve on the work already done, with the knowledge and understanding gained throughout the project. The refined hydrogenation method should result in smooth diamond surfaces, which will allow for better etch rate determinations and focussing of the beam on the surface for more precise etching. Better etch rate determination will also permit a robust calculation of the beam parameters required for mono-layer etching. Reverting to the 20x objective lens will reduce the spot size on the surface, potentially to a diffraction-limited spot, and allow for finer etch lines. More robust electrode contacts could also be formed by first depositing an oxide-forming metal, such as Al, on the surface for the Au contacts to adhere to.

Despite the challenges ahead, there is clear potential for the realisation of a commercial diamond semiconductor device based on UV patterning of surface-terminations as well as other possible interesting applications including quantum devices and biosubstrates; continued research into the physics underpinning the surface electronics and etching mechanism will grant new insights for those in the diamond surface physics and diamond opto-electronics fields.

---

## 6 References

- [1] F. C. Waldermann, P. Olivero, J. Nunn, K. Surmacz, Z. Y. Wang, D. Jaksch, R. A. Taylor, I. A. Walmsley, M. Draganski, P. Reichart, A. D. Greentree, D. N. Jamieson, and S. Prawer, "Creating diamond color centers for quantum optical applications," *Diamond & Related Materials*, vol. 16, pp. 1887–1895, 2007.
  - [2] C.-C. Fu, H.-Y. Lee, K. Chen, T.-S. Lim, H.-Y. Wu, P.-K. Lin, P.-K. Wei, P.-H. Tsao, H.-C. Chang, and W. Fann, "Characterization and application of single fluorescent nanodiamonds as cellular biomarkers," *The National Academy of Sciences of the USA*, vol. 104, no. 3, 2007.
  - [3] R. P. Mildren, J. E. Downes, J. D. Brown, B. F. Johnston, E. Granados, D. J. Spence, A. Lehmann, L. Weston, and A. Bramble, "Characteristics of 2-photon ultraviolet laser etching of diamond," *Optical Materials Express*, vol. 1, pp. 576–585, 2011.
  - [4] V.V. Kononenko, M.S. Komlenok, S.M. Pimenov, and V.I. Konov, "Photoinduced laser etching of a diamond surface," *Quantum Electronics*, vol. 37, no. 11, pp. 1043–1046, 2007.
  - [5] M. Kasu, K. Ueda, Y. Yamauchi, A. Tallaie, and T. Makimoto, "Diamond-based RF power transistors: Fundamentals and applications," *Diamond and Related Materials*, vol. 16, pp. 1010–1015, 2007.
  - [6] Kohn, E. and Ebert, W., "Electronic devices on CVD diamond," in *Low-Pressure Synthetic Diamond*, Dischler, B., Ed. Berlin: Springer, 1998, pp. 331–359.
  - [7] E. Johnson, "Physical limitations on frequency and power parameters of transistors," in *IRE International Convention Record*, 1965, vol. 13, pp. 27–34.
  - [8] R. W. Keyes, "Figure of merit for semiconductors for high-speed switches," *Proceedings of the IEEE*, vol. 60, no. 2, pp. 225–225, Feb. 1972.
  - [9] B. J. Baliga, "Semiconductors for high-voltage, vertical channel field-effect transistors," *Journal of Applied Physics*, vol. 53, no. 3, pp. 1759–1764, 1982.
  - [10] Ioffe Institute, "Physical properties of Silicon," *NSM Archive - Physical properties of semiconductors*. [Online]. Available: <http://www.ioffe.ru/SVA/NSM/Semicond/Si/index.html>. [Accessed: 10-Feb-2014].
  - [11] Ioffe Institute, "Physical properties of Gallium Arsenide," *NSM Archive - Physical properties of semiconductors*. [Online]. Available: <http://www.ioffe.ru/SVA/NSM/Semicond/GaAs/index.html>. [Accessed: 10-Feb-2014].
  - [12] G. Davies, *Properties and Growth of Diamond*. London: INSPEC, 1994.
  - [13] J. Isberg, J. Hammersberg, E. Johansson, T. Wikström, D. J. Twitchen, A. J. Whitehead, S. E. Coe, and G. A. Scarsbrook, "High Carrier Mobility in Single-Crystal Plasma-Deposited Diamond," *Science*, vol. 297, no. 5587, pp. 1670 – 1672, 2002.
  - [14] L. Reggiani, S. Bosi, C. Canali, F. Nava, and S. F. Kozlov, "Hole-drift velocity in natural diamond," *Phys. Rev. B*, vol. 23, no. 6, pp. 3050–3057, Mar. 1981.
  - [15] A. Aleksov, M. Kubovic, N. Kaeb, U. Spitzberg, A. Bergmaier, G. Dollinger, Th. Bauer, M. Schreck, B. Stritzker, and E. Kohn, "Diamond field effect transistors - concepts and challenges," *Diamond and Related Materials*, vol. 12, pp. 391–398, 2003.
  - [16] E. Kohn and A. Denisenko, "Concepts for diamond electronics," *Thin Solid Films*, vol. 515, no. 10, pp. 4333–4339, Mar. 2007.
  - [17] T. H. Borst and O. Weis, "Electrical characterization of homoepitaxial diamond films doped with B, P, Li and Na during crystal growth," *Diamond and Related Materials*, vol. 4, no. 7, pp. 948–953, May 1995.
  - [18] L. Ley, J. Ristein, F. Meier, M. Riedel, and P. Strobel, "Surface conductivity of the diamond: A novel transfer doping mechanism," *Physica B: Condensed Matter*, vol. 376–377, no. 0, pp. 262 – 267, 2006.
  - [19] S. Koizumi, M. Kamo, Y. Sato, H. Ozaki, and T. Inuzuka, "Growth and characterization of phosphorous doped 111 homoepitaxial diamond thin films," *Applied Physics Letters*, vol. 71, no. 8, pp. 1065–1067, 1997.
-

- [20] Kazushi Hayashi, Sadanori Yamanaka, Hideyo Okushi, and Koji Kajimura, "Study of the effect of hydrogen on transport properties in chemical vapor deposited diamond films by Hall measurements," *Applied Physics Letters*, vol. 68, p. 376, 1996.
- [21] P. Gluche, A. Aleksov, A. Vescan, W. Ebert, and E. Kohn, "Diamond Surface-Channel FET Structure with 200 V Breakdown Voltage," *IEEE Electron Device Letters*, vol. 18, no. 11, pp. 547–549, 1997.
- [22] C. E. Nebel, F. Ertl, C. Sauerer, M. Stutzmann, C. F. O. Graeff, P. Bergonzo, O. A. Williams, and R. B. Jackman, "Low temperature properties of the p-type surface conductivity of diamond," *Diamond and Related Materials*, vol. 11, no. 3–6, pp. 351–354, Mar. 2002.
- [23] Minoru Tachiki, Hokuto Seo, Tokishige Banno, Yu Sumikawwa, and Hitoshi Umezawa, "Fabrication of single-hole transistors on hydrogenated diamond surface using atomic force microscope," *Applied Physics Letters*, vol. 81, no. 15, pp. 2854–2856, 2002.
- [24] Morri, Y., Kwarada, M., and Hiraki, A., "Properties of metal/diamond interfaces and effects of oxygen absorbed onto diamond surfaces," *Applied Physics Letters*, vol. 58, pp. 940–941, 1991.
- [25] M. I. Landstrass and K. V. Ravi, "Resistivity of chemical vapor deposited diamond films," *Applied Physics Letters*, vol. 55, no. 10, pp. 975–977, 1989.
- [26] K. Hayashi, S. Yamanaka, H. Watanabe, T. Sekiguchi, H. Okushi, and K. Kajimura, "Investigation of the effect of hydrogen on electrical and optical properties in chemical vapor deposited on homoepitaxial diamond films," *Journal of Applied Physics*, vol. 81, no. 2, pp. 744–753, 1997.
- [27] F. Maier, M. Riedel, B. Mantel, J. Ristein, and L. Ley, "Origin of Surface Conductivity in Diamond," *Phys. Rev. Lett.*, vol. 85, no. 16, pp. 3472–3475, Oct. 2000.
- [28] J. S. Foord, C. H. Lau, M. Hiramatsu, R. B. Jackman, C. E. Nebel, and P. Bergonzo, "Influence of the environment on the surface conductivity of chemical vapor deposition diamond," *Diamond and Related Materials*, vol. 11, no. 3–6, pp. 856–860, Mar. 2002.
- [29] C. E. Nebel, B. Rezek, and A. Zrenner, "Electronic properties of the 2D-hole accumulation layer on hydrogen terminated diamond," *Diamond and Related Materials*, vol. 13, no. 11–12, pp. 2031 – 2036, 2004.
- [30] H. Kiyota, E. Matsushima, K. Sato, H. Okushi, T. Ando, M. Kamo, Y. Sato, and M. Iida, "Electrical properties of Schottky barrier formed on as-grown and oxidized surface of homoepitaxially grown diamond (001) film," *Applied Physics Letters*, vol. 67, no. 24, pp. 3596–3598, 1995.
- [31] S. Albin and L. Watkins, "Electrical properties of hydrogenated diamond," *Applied Physics Letters*, vol. 56, no. 15, pp. 1454–1456, 1990.
- [32] B. Rezek, C. Sauerer, C. E. Nebel, M. Stutzmann, J. Ristein, L. Ley, E. Snidero, and P. Bergonzo, "Fermi level on hydrogen terminated diamond surfaces," *Applied Physics Letters*, vol. 82, no. 14, pp. 2266–2268, 2003.
- [33] D. Petrini and K. Larsson, "Electron Transfer from a Diamond (100) Surface to an Atmospheric Water Adlayer: A Quantum Mechanical Study," *The Journal of Physical Chemistry C*, vol. 111, no. 37, pp. 13804–13812, 2007.
- [34] M. Kubovic, M. Kasu, H. Kageshima, and F. Maeda, "Electronic and surface properties of H-terminated diamond surface affected by NO<sub>2</sub> gas," *Diamond and Related Materials*, vol. 19, no. 7–9, pp. 889–893, Jul. 2010.
- [35] Stephen A.O. Russell, Liang Cao, Dongchen Qi, Alexandre Tallaire, Kevin G. Crawford, Andrew T.S. Wee, and David A.J. Moran, "Surface transfer doping of diamond by MoO<sub>3</sub>: A combined spectroscopic and Hall measurement study," *APPLIED PHYSICS LETTERS*, vol. 103, p. 202112, 2013.
- [36] Sima Dimitrijević, *Understanding Semiconductor Devices*. New York: Oxford University Press, 2000.
- [37] Hugh D. Young and Roger A. Freedman, *University Physics*, 11th ed. San Francisco: Pearson, 2004.
- [38] W. Storr, "MOSFET and Metal Oxide Semiconductor Tutorial," *Electronics Tutorials*, 16-May-2014. [Online]. Available: [http://www.electronics-tutorials.ws/transistor/tran\\_6.html](http://www.electronics-tutorials.ws/transistor/tran_6.html). [Accessed: 19-May-2014].
- [39] Stephen A.O. Russell, Salah Sharabi, Alex Tallaire, and David A.J. Moran, "Hydrogen-Terminated Diamond Field-Effect Transistors With Cutoff Frequency of 53 GHz," *IEEE Electron Device Letters*, vol. 33, no. 10, pp. 1471–1473, 2012.

- [40] K. Ueda, M. Kasu, Y. Yamauchi, T. Makimoto, M. Schwitters, D. J. Twitchen, G. A. Scarsbrook, and S. E. Coe, "Diamond FET using high-quality polycrystalline diamond with  $f_T$  of 45 GHz and  $f_{max}$  of 120 GHz," *Electron Device Letters, IEEE*, vol. 27, no. 7, pp. 570–572, Jul. 2006.
  - [41] P. Calvani, A. Corsaro, M. Girolami, F. Sinisi, D.M. Trucchi, M.C. Rossi, G. Conte, S. Carta, E. Giovine, S. Lavanga, E. Limiti, and V. Ralchenko, "DC and RF performance of surface channel MESFETs on H-terminated polycrystalline diamond," *Diamond and Related Materials*, vol. 18, pp. 786–788, 2009.
  - [42] Tokishige Banno, Minoru Tachiki, Hokuto Seo, Hitoshi Umezawa, and Hiroshi Kawarada, "Fabrication of diamond single-hole transistors using AFM anodization process," *Diamond and Related Materials*, vol. 11, pp. 387–392, 2002.
  - [43] R.E. Prange, *The Quantum Hall Effect*. Springer, 1987.
  - [44] V.I. Konov, T.V. Kononenko, and V.V. Kononenko, "Laser Micro- and Nanoprocessing of Diamond Materials," in *Optical Engineering of Diamond*, First Edition., Weinheim, Germany: Wiley-VCH Verlag GmbH & Co. KGaA, 2013, pp. 388–392.
  - [45] V. V. Kononenko, T. V. Kononenko, S. M. Pimenov, V. I. Konov, P. Fischer, V. Romano, H. P. Weber, A. V. Khomich, R. A. Khmel'nitskiy, and V. N. Strekalov, "Laser-induced structure transformations of diamonds," in *Proceedings of SPIE*, 2003, vol. 5121, pp. 259–270.
  - [46] E. Granados, D. J. Spence, and R. P. Mildren, "Deep ultraviolet diamond Raman laser," *Optics Express*, vol. 19, pp. 10857–10863, 2011.
  - [47] H. Kawarada, "Hydrogen-terminated diamond surfaces and interfaces," *Surface Science Reports*, vol. 26, no. 7, pp. 205–259, 1996.
  - [48] I. Friel, "Optical Quality Diamond Grown by Chemical Vapor Deposition," in *Optical Engineering of Diamond*, First Edition., Weinheim, Germany: Wiley-VCH Verlag GmbH & Co. KGaA, 2013, pp. 35–69.
  - [49] Y. L. Zhong and K. P. Loh, "The Chemistry of C-H Bond Activation on Diamond," *Chemistry – An Asian Journal*, vol. 5, no. 7, pp. 1532–1540, 2010.
  - [50] J. Ristein, W. Stein, and L. Ley, "Defect Spectroscopy and Determination of the Electron Diffusion Length in Single Crystal Diamond by Total Photoelectron Yield spectroscopy," *Phys. Rev. Lett.*, vol. 78, no. 9, pp. 1803–1806, Mar. 1997.
  - [51] B. D. Thoms, M. S. Owens, J. E. Butler, and C. Spiro, "Production and characterization of smooth, hydrogen-terminated diamond C(100)," *Applied Physics Letters*, vol. 65, no. 23, pp. 2957–2959, 1994.
  - [52] H. Sato and M. Kasu, "Electronic properties of H-terminated diamond during NO<sub>2</sub> and O<sub>3</sub> adsorption and desorption," *Diamond & Related Materials*, vol. 24, pp. 99–103, 2012.
  - [53] O. Auciello and A. V. Sumant, "Status review of the science and technology of ultrananocrystalline diamond (UNCD™) films and application to multifunctional devices," *Diamond and Related Materials*, vol. 19, no. 7–9, pp. 699 – 718, 2010.
  - [54] H. Ishizaka, H. Umezawa, H. Taniuchi, T. Arima, N. Fujihara, M. Tachiki, and H. Kawarada, "DC and RF characteristics of 0.7- $\mu$ m-gate-length diamond metal–insulator–semiconductor field effect transistor," *Diamond and Related Materials*, vol. 11, no. 3–6, pp. 378 – 381, 2002.
  - [55] S.P. Lansley, Hui Jin Looi, M.D. Whitfield, and R.B. Jackman, "An optically activated diamond field effect transistor," *Diamond and Related Materials*, vol. 8, pp. 946–951, 1999.
  - [56] Hitoshi Umezawa, Hirotada Taniuchi, Takuya Arima, Minoru Tachiki, and Hiroshi Kawarada, "Potential applications of surface channel diamond field-effect transistors," *Diamond and Related Materials*, vol. 10, pp. 1743–1748, 2001.
  - [57] Masataka Imura, Ryoma Hayakawa, Hirotaka Ohsato, Eiichiro Watanabe, Daiju Tsuya, Takahiro Nagata, Meiyong Liao, Yasuo Koide, Jun-ichi Yamamoto, Kazuhito Ban, Motoaki Iwaya, and Hiroshi Amano, "Development of AlN/diamond heterojunction field effect transistors," *Diamond and Related Materials*, vol. 24, pp. 206–209, 2012.
  - [58] M. Kasu, K. Ueda, H. Kageshima, and Y. Yamauchi, "Gate interfacial layer in hydrogen-terminated diamond field-effect transistors," *Diamond and Related Materials*, vol. 17, no. 4–5, pp. 741–744, Apr. 2008.
-

- [59] G. Conte, E. Giovine, M. Girolami, S. Salvatori, A. Bolshakov, V. Ralchenko, and V. Konov, "Polycrystalline diamond UV-triggered MESFET receivers," *Nanotechnology*, vol. 23, no. 7, p. 075202, 2012.
  - [60] S. P. Lansley, O. Gaudin, H. Ye, N. Rizvi, M. D. Whitfield, R. D. McKeag, and R. B. Jackman, "Imaging deep UV light with diamond-based systems," *Diamond and Related Materials*, vol. 11, no. 3–6, pp. 433–436, Mar. 2002.
  - [61] M. Geisler and T. Hugel, "Aging of Hydrogenated and Oxidized Diamond," *Advanced Materials*, vol. 22, no. 3, pp. 398–402, 2010.
  - [62] Fluke Corporation, "Fluke 45 Dual Display Multimeter," 2014. [Online]. Available: <http://www.fluke.com/fluke/m3en/digital-multimeters/Fluke-45.htm?PID=56082>. [Accessed: 15-Aug-2014].
  - [63] Ian M. Watt, *The principles and practice of electron microscopy*, Second edition. Cambridge: Cambridge University Press, 1997.
  - [64] Keithley Instrument Inc, "Model 617 Programmable Electrometer Quick Reference Guide Rev. A." [Online]. Available: <http://www.keithley.com/support/data?asset=1065>. [Accessed: 26-Aug-2014].
-

## 7 Appendix

### 7.1 Optical Interferometry

In order to determine the rate at which diamond is being etched under exposure to UV laser light, a method of investigating the surface morphology is required to determine the depth of the etch over the duration of the exposure. The technique used in this project was optical interferometry. A WYKO NT9800 from Veeco Instruments Inc. was used for all surface profiling. The following is adapted from the help files for the 'Vision 32' software package from Veeco Inc.

Two techniques were used phase-shifting interferometry (PSI) and vertical-scanning interferometry (VSI). The differences between PSI and VSI are summarised here and detailed below.

1. VSI requires unfiltered white light for measurements. PSI requires filtered light.
2. VSI vertically scans through a specified distance—the magnification objective actually moves through focus. PSI causes a phase-shift at a single focus point—the magnification objective does not move through focus.
3. VSI uses an algorithm that processes fringe modulation data from the intensity signal to calculate surface heights. PSI uses an algorithm that processes phase data from the intensity signal to calculate surface heights. Each algorithm has limits; each one is very reliable within its limitations.
4. VSI mode measures “rough” surfaces, while PSI measures “smooth” surfaces. These two modes allow you to measure a wide range of smooth and rough surfaces.

#### 7.1.1 Phase-shifting Interferometry (PSI)

For phase-shifting interferometry, a white-light beam is filtered and passed through an interferometer objective to the sample surface. The interferometer beam splitter reflects half of the incident beam to a reference surface within the interferometer. When the surface is in focus, the reflected beams from the sample surface and the reference surface form interference fringes. A piezoelectric transducer moves the reference surface linearly a small known amount to cause a phase shift between the objective and reference beams. The intensity of the resulting interference pattern is recorded at numerous relative phase shifts, and then converts the intensity to wavefront (phase) data by integrating the intensity data. The relative surface height of the sample surface can be calculated from the phase data as follows:

$$h(x, y) = \frac{\lambda}{4\pi} \phi(x, y)$$

Equation 7-1

where  $\lambda$  is the wavelength of the source beam, and  $\phi(x, y)$  is the phase data.

This technique is limited to fairly smooth, continuous surfaces; when the surface-height difference between adjacent measurement points is greater than  $\lambda / 4$  height errors in multiples of  $\lambda / 2$  may be introduced and the wavefront cannot be correctly reconstructed. PSI is reliable for smooth surfaces in which the height change between two adjacent points is not more than approximately 160 nm. For height changes greater than this, VSI must be used. PSI can accurately resolve smooth surfaces of less than 3 Å rms for a single measurement.



### 7.1.2 Vertical-scanning Interferometry (VSI)

To resolve rougher surfaces, vertical-scanning interferometry techniques are used. The basic interferometric principles are similar to phase-shifting interferometry: light reflected from a reference mirror combines with light reflected from a sample to produce interference fringes, where the best-contrast fringe occurs at best focus. However, in VSI mode, the white-light source is not filtered, and the system measures the degree of fringe modulation, or coherence, instead of the phase of the interference fringes.

The reference arm containing the interferometric objective moves vertically to scan the surface at varying heights during the measurement. Because white light has a short coherence length, interference fringes are present only over a very shallow depth for each focus position. Fringe contrast at a single sample point reaches a peak as the sample is translated through focus.

The system scans through the focus at evenly-spaced intervals as the camera captures frames of interference data. As the system scans downward, an interference signal for each point on the surface is recorded. The system uses a series of computer algorithms to demodulate the envelope of the fringe signal. Low-frequency components are first removed from the signal; the signal is rectified by square-law detection, then filtered; and finally, the peak of the low-pass filter output is located and the vertical position that corresponds to the peak is recorded. Finally the vertical position corresponding to the peak of the interference signal is extracted for each point on the surface.

To increase the resolution of the measurement beyond the sampling interval, a curve-fitting interpolation technique is employed by the software package. The surface height resolution is approximately 3 nm rms for a single measurement on a smooth, highly reflective sample. For resolving surfaces smoother than this, PSI must be used. The range of heights that VSI can profile is limited only by the range of the piezoelectric transducer to perform the translation through focus. For WYKO profilers, such as the NT9800, the range is up to 500 mm.

---

## 7.2 G-code scripts

The following is a representative example of the coding scripts developed throughout this project for the feed-back and control of the translation stage and shutter operation of the laser etching system. This particular script is responsible for writing the field-effect transistor devices in Chapter 4.5; an example of the output of this script is seen in Figure 4-14.

```

ENABLE X Y Z           ; enable translation stage axis movement
g91                    ; relative movement
g92                    ; set zero
v1 = 1.3                ; feed rate for etching
v2 = 20                 ; fast etch rate
v3 = 10                 ; alignment feed rate
g1 x-0.05 y0.05 fv3    ; after positioning on corner of Au
ou0,0                  ; open shutter
loop 4                  ; start source-drain channel isolation
g1 x0.36 fv1
g1 y-0.13               ; source-drain channel start side 1
g1 x0.525
g1 y0.13               ; source-drain channel end side 1
g1 x0.36
g1 y-0.36
g1 x-0.36
g1 y0.13               ; source-drain channel start side 2
g1 x-0.525
g1 y-0.13               ; source-drain channel end side 2
g1 x-0.36
g1 y0.36
next                   ; end source-drain channel isolation
ou0,1                  ; close shutter
g1 x0.41 y-0.13 fv3    ; move position for gate-drain isolation
ou0,0                  ; open shutter
loop 2                 ; start gate-drain isolation
g1 y0.43 fv1
g1 x1.095
g1 y-1.594
g1 x-1.095
g1 y1.064
g1 y-1.064             ; back
g1 x1.095
g1 y1.594
g1 x-1.095
g1 y-0.43
next                   ; end gate-drain isolation
ou0,1                  ; close shutter
g1 x0.425 fv3          ; move to position for extra gate-drain isolation
ou0,0                  ; open shutter
loop 2                 ; start extra gate-drain isolation
g1 y0.18 fv1
g1 x0.46
g1 y-0.46
g1 x-0.46
g1 y0.18

```

---

```
g1 y-0.18
g1 x0.46
g1 y0.46
g1 x-0.46
g1 y-0.18
next                                ; start extra gate-drain isolation
ou0,1                              ; close shutter
g1 y0.005 fv3                      ; move to position for source-drain channel raster
ou0,0                              ; open shutter
loop 21                            ; start source-drain channel raster
g1 y-0.08 fv2
g1 x-0.01
g1 y0.08
g1 x-0.01
next                                ; end source-drain channel raster
ou0,1                              ; close shutter
```

---